THE UNIVERSITY OF MICHIGAN
INDUSTRY PROGRAM OF THE COLLEGE OF ENGINEERING

THE EFFECT OF CHANGES IN CATALYST COMPOSITION ON THE HYDROGEN-DEUTERIUM EXCHANGE REACTION ON COBALT FERRITE

Robert G. Squires

A dissertation submitted in partial fulfillment
of the requirements for the degree of
Doctor of Philosophy in the
University of Michigan
Department of Chemical and Metallurgical Engineering
1962

October, 1962

IP-587

ACKNOWLEDGEMENTS

The author wishes to express his appreciation to the members of his committee for their guidance during the course of this work. Special thanks are due to Professor G. Parravano, who suggested the topic for this research and served as chairman, for his numerous helpful suggestions and criticisms. The author would also like to give special thanks to Professor J. J. Martin for his encouragement given throughout the author's studies, and to Professor D. R. Mason for arousing the author's interest in the application of semiconductor theory to catalysis.

The author is indebted to the Standard Oil Company of California and to the National Science Foundation for their financial aid through the award of fellowships for four years.

To the laboratory and shop personnel of the Department of Chemical and Metallurgical Engineering the author expresses his thanks. In particular, Mr. F. B. Drogosz deserves the author's thanks for his assistance in solving some of the analytical problems presented by this work.

Finally, the author would like to thank his wife for her constant encouragement and for the typing of both the rough and final drafts of this manuscript. The drafting of the figures by Mr. T. F. Beals and the printing of this manuscript by the Industry Program of the College of Engineering are also very much appreciated.

TABLE OF CONTENTS

TABLE OF CONTENTS CONT'D

LIST OF TABLES

LIST OF FIGURES

LIST OF FIGURES CONT'D

LIST OF FIGURES CONT'D

LIST OF APPENDICES

ABSTRACT

The catalytic activity of the hydrogen-deuterium exchange reaction on cobalt ferrite catalysts and the change in thermoelectric power of the ferrite during the adsorption of hydrogen and oxygen were investigated as functions of the catalyst composition. The relationships between the semiconducting and catalytic properties of cobalt ferrite were analyzed in the light of recent developments in the electron theory of catalysis.

The hydrogen-deuterium exchange reaction was investigated on ferrite catalysts, $Co_{3-x}Fe_xO_4$, with four different compositions: two n-type catalysts with $x > 2$, $Co_{0.93}Fe_{2.07}O_4$ and $Co_{0.98}Fe_{2.02}O_4$; and two p-type catalysts with $x < 2$, $Co_{1.03}Fe_{1.97}O_4$ and $Co_{1.07}Fe_{1.93}O_4$. The study was made using a flow reactor at approximately 75°C, 1 atmosphere pressure. Analyses of the gas samples were made by means of a mass spectrometer. The activation energy increased from 19 Kcal/mole to 24 Kcal/mole and the pre-exponential factor increased from 10^{30} to 10^{37} as the composition progressed from $x < 2.0$ to $x > 2.0$.

The change of thermoelectric power of compressed powder ferrite pellets during the adsorption of hydrogen and oxygen was investigated in the temperature range 88°-250°C on two samples of cobalt ferrite, one n-type ($Co_{0.96}Fe_{2.04}O_4$) and one p-type ($Co_{1.09}Fe_{1.91}O_4$). At temperatures above 120°C hydrogen was adsorbed on the cobalt ferrite as an electron donor, and oxygen was adsorbed

as an acceptor. No change in thermoelectric power was observed during the adsorption of hydrogen or oxygen in the lower temperature (88°C) runs, indicating that little electron transfer occurs between the adsorbed molecules and the catalyst surface in this temperature range.

It is concluded that the hydrogen-deuterium exchange reaction on cobalt ferrite occurs in two stages: (1) The first stage is an activation stage, in which the catalytic activity increases with time. This step might be associated with the reduction of oxygen on the surface of the ferrite, and the corresponding formation of OH and OD groups. (2) In the second stage the exchange reaction occurs with constant activity. In this step, it seems likely that exchange occurs between hydrogen and deuterium, and the OD and OH groups formed in stage (1).

This study has furnished data which indicates that the change in thermoelectric power of particulate systems due to gas chemisorption may be used to gain an insight into the electron exchange at the catalyst surface.

I. INTRODUCTION

A. Background and Scope of Research

The main objective of this research was to investigate and analyze in the light of recent developments in the electron theory of catalysis, the relationship between the semiconducting and catalytic properties of a semiconducting oxide catalyst. More specifically, the catalytic activity of a cobalt ferrite catalyst for the hydrogen-deuterium exchange reaction and the change in thermoelectric power of the ferrite during adsorption of hydrogen gas were investigated as a function of catalyst composition.

Cobalt ferrite, $Co_{3-x}Fe_xO_4$, was chosen for the following reasons:

1) In the composition range $1.9 < x < 2.1$, single phase spinels are formed with a metal to oxygen ratio of 3:4. The concentration of lattice vacancies is small enough to be neglected in the theoretical considerations.

2) Numerous previous workers in the literature have investigated oxide catalysts which are single carrier semiconductors. The catalyst, in these cases, was always p-type or n-type and only the carrier concentrations could be changed by doping with small concentrations of foreign elements. When Fe is added to $CoFe_2O_4$, it enters the crystal structure as Fe^{II}, which acts as an electron donor and causes the ferrite to become an n-type semiconductor. When Co is added to $CoFe_2O_4$, it enters the crystal structure as Co^{III}, which acts as an acceptor, causing the ferrite to become a

p-type semiconductor. The opportunity is therefore afforded to study a reaction on an oxide catalyst having a single chemical substrate with either electrons (n-type catalyst) or holes (p-type catalyst) in excess. Furthermore, no foreign impurities need be added to the ferrite.

3) The bulk thermoelectric properties of polycrystaline sintered cobalt ferrite have been reported by Jonker[45]. As the catalyst composition increases from 1.9 to 2.1 Jonker observed a resistivity change from 10^7 to 10^2 ohm-cm and a thermoelectric power change from +800 to -600 μv/°C. If a relationship does exist between the electrical properties and the catalytic properties of the ferrite, one might expect a corresponding change in catalytic activity in this composition range.

The hydrogen deuterium exchange reaction was chosen since it was relatively simple and preliminary studies indicated that it proceeded at a conveniently low temperature. Due to the experimental difficulties involved in obtaining meaningful conductivity data in high impedance particulate systems, the thermoelectric power was chosen as the semiconducting property to be measured so that an insight could be gained into the nature of the electron transfer process taking place between the adsorbed gas molecules and the catalyst surface. Since the cobalt ferrite is a narrow band, or localized level semiconductor, no appreciable Hall effect, photoconductivity, or carrier injection effect would be expected. These effects, which are often used in studying the

electrical properties of semiconducting materials, were, therefore, not investigated.

The simultaneous measurement of thermoelectric power and catalytic activity was originally proposed. Experimental difficulties soon demonstrated that this approach was impractical. Therefore, the kinetic and thermoelectric properties of cobalt ferrite were investigated independently.

Some effort was devoted to considering possible reaction mechanisms. A possible reaction mechanism is proposed which is consistent with the data in this study and with other work in the literature.

Several runs were also made on mechanically mixed n- and p-type catalysts and on sintered n- and p-type catalysts to qualitatively determine if the formation of p-n junctions would affect the catalytic activity of the ferrite.

B. Literature Survey

The pertinent literature can be divided into two main sections, the first of which is concerned with the theoretical development and experimental verification of the role which electron transfer takes in adsorption and in heterogeneous catalysis. The investigations of the hydrogen-deuterium exchange reaction on various catalysts and of kinetic studies using ferrite catalysts for various reactions pertain more directly to this thesis and are therefore reviewed in more detail in separate sections. Although much work has also been done on metals, this survey will emphasize

the adsorption and heterogeneous catalysis on oxide semiconductors. The second category includes the methods of preparation, phase behavior, and semiconducting properties of cobalt ferrite. These sections of the literature are reviewed below and those articles which pertain directly to this work are discussed in more detail in other chapters of this thesis.

1. The Electron Theory of Catalysis

a. Development of Theory

A theoretical approach to surface catalysis was considered in 1916 by Langmiur[60] who suggested that chemical forces hold adsorbed particles to the surface. Roginskii and Schultz[80], in 1928 emphasized the electronic considerations and Rideal and Wansbrough-Jones[76] proposed a relationship between the work function of metals and the speed of catalytic reaction. De Boer[16] studied the relationship between the work function and the ionization potential of the adsorbed gas during ionic adsorption. Brewer[13], 1928, Schmidt[83], 1933, and Nyrop[71], 1935, suggested that during some catalytic reactions the adsorbed species must be present on the surface in an ionized form. Lennard-Jones[62], in his electron theory of chemisorption on metal surfaces, formulated the problem of the electron transfer process in chemisorption.

With the development of quantum mechanical treatments of solids and the application of Fermi-Dirac statistics to electrons, detailed studies of the electronic factor in catalysis on metals

and semiconductors became possible. Reviews of the theoretical and experimental development of the electron transfer process in metals have been given by Garner[30] and Culver and Tompkins[15].

The electron theory of catalysis relating chemisorption, catalytic activity and semiconducting properties for semiconducting oxides cannot yet be regarded as complete. At least three approaches to the problem have been proposed. The boundary-layer theory, independently developed by Aigrain and Dugas[1], Hauffe and Engell[38] and Weisz[105] emphasizes the electron transfer between the semiconductor and the chemisorbed layer. The density and energy level of the surface electrons are changed by the space charge which builds up in the boundary layer between the interior of the semiconductors and the adsorbed species on the surface; this change in surface electron charge density causes corresponding changes in the heat of adsorption and the reactivity of the chemisorbed gas. Wolkenstein[109], [110], [111], in another approach, emphasizes the covalent and ionic bond formation between adsorbate and semiconductor using conduction electrons or electron holes of the semiconductor. Wolkenstein[109], [110], [111] differentiates between "weak" and "strong" chemisorption. Dowden, Mackenzie, and Trapnell [19] emphasize covalent bonding by means of atomic orbitals or electrons of the metal ions of the oxide.

Recent articles by Wolkenstein [112], [113], indicate his views on the present state of the electron theory of catalysts. Roginskii [79] has attempted to formulate rules for the selection

of catalysts based on the electron theory of catalysis. An attempt has been made by Garrett[32] to indicate how the electron theory may be applied in a quantitative manner. Garrett's paper follows the approach of Krusemeyer and Thomas[56] to the adsorption and charge transfer on semiconducting surfaces.

b. Chemisorption Studies

The electron theory of chemisorption predicts a variation in the semiconducting properties of the solid surface, such as the electrical conductivity, Hall effect, and thermoelectric power, with gas adsorption. Experimental verifications of this effect have been given, for example, for the adsorption of various gases on ZnO[5, 14, 24, 28, 40, 47, 54, 58, 69, 91, 101, 103], NiO[7, 8, 24, 48, 101], and Cu_2O[31, 34, 47, 74].

Other examples may be found in review articles by Wolkenstein[112], Parravano and Boudart[73], Winter[100], Hauffe[37], and Morrison[68].

c. Reaction Studies

Many experimental studies have been reported which attempt to relate the catalytic activity to the semiconducting properties of the catalyst surface. The decomposition of nitrous oxide, oxidation of carbon monoxide, and hydrogen-deuterium exchange, in particular, have been frequently used to study this effect. These investigations fall into two categories. The first group of experiments measured changes in reaction rate or activation energy as a function of the hole and electron concentration of the catalyst, which

may be controlled by bulk doping. Wagner[102], first used this technique in trying (unsuccessfully) to improve the rate of the nitrous oxide decomposition on ZnO by doping the latter with Ga_2O_3. Later experiments, however, were successful. For example, Schwab and Block[86] have investigated the carbon monoxide oxidation on Li- and Cr-doped NiO and Ga- and Li-doped ZnO. In both cases a change in activation energy with doping was observed. Similar correlations between catalytic activity and doping have been reported by Schwab et al.[87] for the carbon monoxide oxidation on various mixed oxides; Molinari and Parravano[66] for the hydrogen-deuterium exchange on ZnO; Hauffe et al.[39] for the nitrous oxide decomposition on NiO; Block and Chon[10] for the carbon monoxide oxidation on CoO; Keier et al.[49] for the carbon monoxide oxidation on NiO; Otwinowska et al.[72] for the dehydration of isopropanol on ZnO; and Dogramadzi and Matic[18] for the hydrogen-deuterium exchange on ZnO and NiO.

All of the experiments mentioned above were made on single carrier oxide semiconductors. A few experiments have been conducted on two carrier semiconductors in which not only the carrier concentration but also the type of carrier may be changed by doping. Watson[104], for instance, has investigated the catalytic activity of the Friedel-Crafts reaction on p- and n-type germanium. Penzkofer[75] reported that the activation energy for the dehydrogenation of formic acid on germanium was less for p-type (32 Kcal/mole) than for n-type (40 Kcal/mole). The hydrogenation

of ethylene on p- and n-type germanium and silicon has been reported by Krawczynski[54]. The activation energy was found to be 22 Kcal/mole for n-type and 3 to 6 Kcal/mole for p-type germanium. The similar study on silicon gave activation energies of 11 Kcal/mole and 5 Kcal/mole, respectively. Kuchaev and Boreskov[59] reported that, at 150°C, intrinsic germanium was an order of magnitude more active for the hydrogen-deuterium exchange than were either n-type or p-type germanium.

The second category of experiments measures both the electrical conductivity and catalytic activity during the course of a reaction. This type of investigation has been made by Matveev and Boreskov[65] for the dissociation of methyl alcohol on ZnO; by Bielanski et al.[6] for the dehydration of ethyl alcohol on various oxides; Weller and Voltz[106] for the hydrogen-deuterium exchange on Cr_2O_3; Otwinowska[72] et al. for the dehydration of isoproponal on ZnO. Schwab[85] reported a variation of electrical conductivity with catalytic activity for various mixed catalysts. A similar investigation was also made by Alkhazov and Bielanski[2] on $Fe_2O_3Al_2O_3$. Further discussion may be found in review articles by Wolkenstein[112], Law[61], Parravano and Boudart[73], Winter[108], Hauffe[37] and Morrison[68].

d. Hydrogen-Deuterium Exchange Studies

Hydrogen-deuterium exchange and reversible chemisorption have been observed for ZnO in the temperature range -190° to 200°C by Taylor et al.[93][94] and Harrison and McDowell[36]. Heckelsberg et al.[41] measured the simultaneous variation of con-

ductivity and catalytic activity of the hydrogen-deuterium exchange on Li-, Al-, and Cr-doped ZnO. Molinari and Parravano[66] measured the catalytic activity of the hydrogen-deuterium exchange on ZnO as a function of Li-, Al-, and Ga-doping. The catalytic activity of chromic oxide for hydrogen-deuterium exchange after pretreatment in either hydrogen or oxygen was measured by Weller and Voltz[106]. Dowden et al.[19] measured the rate of hydrogen-deuterium exchange on the oxides of most of the transition metals. Dogramadzi and Matic[18] studied the effect of Li- and Ga-doping of ZnO and NiO on the catalytic activity of the hydrogen-deuterium exchange. The hydrogen-deuterium exchange on p-type, n-type and intrinsic germanium was studied by Kuchaev and Boreskov[59]. Other investigations using the hydrogen-deuterium exchange on oxides are discussed in review articles by Parravano and Boudart[73] and Halpern[35].

e. Reactions on Ferrite Catalysts

Schwab et al.[87] reported that the carbon monoxide oxidation proceeds faster and with lower activation energy on zinc ferrite than on magnesium ferrite. Svaalenak and Scott[92] investigated the ortho-para hydrogen conversion on iron-zinc oxide catalysts as a function of increasing ferrite content. In his review on the properties of oxide catalysts based on semiconducting properties, Solymosi[90] included a detailed discussion of the relationship between the catalytic properties of oxide mixtures and spinels and their electrical properties. Linde et al.[63] studied the catalytic

activity of Co-Mn spinels for the oxidation of propane. The catalytic activity for the conversion of water gas on ferrites of NiO, ZnO, CoO, MnO, and MgO was studied by Fukutome and Kusano[29]. Most exhibited weak activity. $NiO-Fe_2O_3$ and $CoO-Fe_2O_3$, however, were found to be very active after a short initiation period in which the ferrite is reduced by the water gas.

2. Cobalt Ferrite

a. Preparation

The general methods of ferrite preparation have been outlined by Economos[20]. Economos[21] also compared these different methods, giving the percent conversion to ferrite as a function of firing time and temperature for Ni ferrite. The effect of iron oxide particle size on Ni ferrite formation was reported by Economos and Clevenger[22]. Methods of preparation of cobalt ferrite are outlined by Robin and Benard[78], Smiltens[89] and Jonker[45].

b. Phase Behavior

Robin and Benard[78] constructed a phase diagram for the Fe-Co-O systems based on x-ray diffraction data of a series of mixed iron and cobalt samples heated at temperatures up to 1000°C. Smiltens[89] studied the 1200°C, 1400°C and 1626°C isotherms of the Fe-Co-O systems. Smiltens[89] used the triangular diagram method, based on chemical analysis of the quenched samples and x-ray diffraction data. The data of Smiltens[89] was substantiated by Jonker[45] at a temperature of 1350°C. Both Smiltens[89] and

Jonker reported that in the vicinity of $CoFe_2O_4$ the ferrite has a spinel structure with a ratio of metal to oxygen ions of 3:4.

c. Semiconducting Properties

The semiconducting properties of transition metal oxides, including cobalt ferrite, were reported by Jonker and Van Houten[46]. A detailed analysis of the semiconducting properties of cobalt ferrite was made by Jonker[45]. From measurements of resistivity, activation energy and Seebeck effect, Jonker[45] derived an energy level scheme by which the semiconducting properties of $CoFe_2O_4$ can be described.

II. THEORY

A. Semiconducting Properties of Cobalt Ferrite

Cobalt ferrite belongs to the group of transition metal oxides whose semiconducting properties depend on a partially filled 3d band. The importance of understanding the fundamental properties of the transition metal oxides has been emphasized in recent years, due to their increased use in heterogeneous catalysis[23], electric[4] and magnetic[33] circuits, and corrosion applications[25]. A review of the properties of oxides of the 3d transition metals has been given by Morin[67].

In the case of a relatively simple oxide such as zinc oxide, the energy bands may arise from the filled 2p levels of the $O^{=}$ and the empty 4s levels of the Zn^{++} which are broadened when the ions form the solid. The energy gap, or forbidden region, which determines the semiconducting properties of the oxides is the energy separation of the 2p and 4s bands. However, the existance of a partially filled 3d band in the transition metal oxides makes possible other energy levels in the 3d band. The semiconducting properties of 3d oxides will be controlled by the relative energy of the 3d and 2p levels of the anions and the 4s levels of the cation. Morin[67] points out that calculations of the energy levels of the 3d metals[88] indicate that the 4s band is at least 10 ev wide and overlaps the 3d band which, in Ni, for example, is approximately 2.8 ev wide. Since the 3d band can hold 10 electrons as

compared to two electrons for the 4s band, the 3d band in Ni, per electron, is only 1/15 as wide as the 4s band. Morin[67] postulates that the overlap of the 3d wave function in the already narrow 3d band present in the metals is reduced further due to the increased distance between the ions in the oxide. When the 3d band becomes extremely narrow, it can no longer be considered a continuous band, and the 3d charge carrier can be treated as occupying energy levels localized on the cations.

The conduction in such a narrow band or "localized level" semiconductor is due to the lattice vibrations which cause the electron wave functions on adjacent cations to overlap with a higher degree of probability. Transport of this type, resulting in an extremely low mobility (10^{-4} to 10^{-8} $cm^2/v.-sec.$ for $CoFe_2O_4$) which increases exponentially with temperature, is given by

$$\mu = \frac{d^2 e \nu \, e^{-q/kT}}{kT} \qquad (1)$$

where μ = mobility

d = jump length

ν = lattice frequency

q = activation energy for lattice deformation

Due to the very low mobility, no Hall effect, photoconductivity, or carrier injection would be expected in a localized level semiconductor.

For conduction to take place in the 3d levels, there must be present in pure $CoFe_2O_4$, some Co^{III} and Fe^{II}(hole electron pair)

which can exchange electrons with Co^{II} and Fe^{III}. These states, however, can exist only at high temperature. However, the room temperature semiconducting properties of $CoFe_2O_4$ can be varied by introducing excess Co^{III} (holes) or Fe^{II} (electrons) into the lattice. Cobalt ferrite has an inverse spinel structure, with the cobalt ions and half of the iron ions on the octahedral sites, and the remaining iron on the tetrahedral sites. Since excess Fe^{II} and Co^{III} also occupy octahedral sites, cobalt ferrite, $Co_{3-x}Fe_xO_4$, may be considered as the following series of mixed crystals. For $x > 2$ the mixed crystal consists of 3-x molecules of $Fe^{II}(Co^{II}Fe^{III})O_4$ and x-2 molecules of $Fe^{III}(Fe^{II}Fe^{III})O_4$; thus x-2 represents the Fe^{II} or electron content per molecule of the n-type ferrite. For the p-type ferrite ($x < 2$) the crystal can be considered x-1 molecules of $Fe^{III}(Co^{II}Fe^{III})O_4$ and 2-x molecules of $Fe^{III}(Co^{II}Co^{III})$; thus 2-x represents the Co^{III} or hole concentration of the ferrite. Since the n- and p-type conductivities of cobalt ferrite can be related to the concentration of excess Fe^{II} and Co^{III} in the lattice, cobalt ferrite may be classified as a controlled-valency semiconductor [Verwey et al. (99)(100)]. Note, however, that no foreign doping elements need be added to the lattice.

Jonker(45) proposed the following localized band model to describe the semiconducting properties of cobalt ferrite (Figure 1). The following discussion (through equation 18) outlines Jonker's(45)(46) treatment of the semiconducting properties of cobalt ferrite.

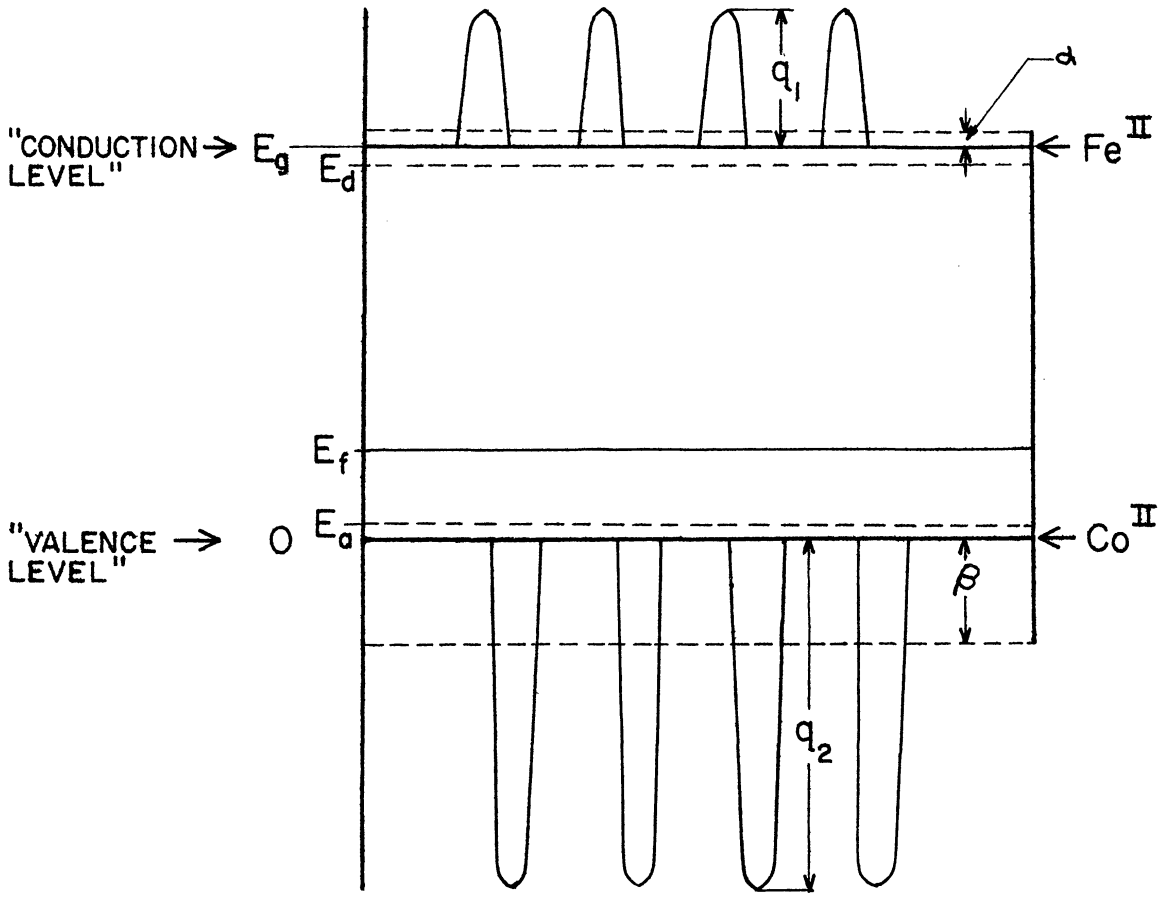

Figure 1. Energy Level Scheme for Cobalt Ferrite. E_f is the Fermi level (for a p-type ferrite in this case). q_1 and q_2 are activation energies for jumps of electrons and holes. α and β are the contribution to transport levels of electrons and holes. Energy of Co^{II} is taken as zero. E_g is energy of Fe^{II} level. Ea and Ed are the energies of acceptor and donor levels.

Since the distribution of charge carriers over the different energy levels affects both the conductivity and Seebeck effect, a brief description follows concerning the application of Fermi statistics for interpreting the measurements. The method of calculation is analogous to that for the energy band

scheme in normal semiconductors [i.e. Kittel[51], Mason[64]] with the bands replaced by localized energy levels.

For the case of p-type ferrites, with excess Co, the application of Fermi statistics gives

$$\frac{N_V}{1 + \exp\left(E_f/kT\right)} = \frac{N_A}{1 + \exp\left[(E_a - E_f)/kT\right]} + \frac{N_C}{1 + \exp\left[(E_g - E_f)/kT\right]} \qquad (2)$$

(holes in valence level) = (electrons in acceptor level) + (electrons in conduction level)

Since the Co^{III} concentration is small in the series of mixed crystals in this study, the number of available valence levels and conduction levels, designated by N_V and N_C, will be approximately equal to the number of cobalt or iron ions, respectively, which occupy octahedral sites. Since there are eight Co ions and eight Fe ions occupying octahedral sites in the cobalt ferrite unit cell, and since the cell constant is 8.39Å, it follows that $N_V = N_C = 1.35 \times 10^{22} cm^{-3}$. Since $N_V = N_C$, in the following discussion the subscript will be dropped (i.e., $N_V = N_C = N$).

Equation (2), relating the hole concentration, the Fermi level, temperature and acceptor level concentration, can be simplified by making various assumptions which are valid over limited temperature ranges. At low temperatures the last term of Equation (2) may be neglected, and the resulting equation which is quadratic in the

factor, $\exp(-E_f/kt)$, and may be solved for E_f. When $kT \ll Ea$, the resulting equation simplifies to

$$E_f = kT \ln \frac{N}{N_A} \tag{3}$$

In this temperature region where the donor levels are completely ionized, but the intrinsic conduction is still negligible, the concentration of holes in the valence level, n_2, will equal the concentration of acceptor levels, N_a. Therefore, Equation (3) may be written

$$E_f = kT \ln \frac{N}{n_2} \tag{4}$$

or

$$n_2 = N \exp\left(- E_f/kT\right) \tag{5}$$

For an n-type material, with excess Fe^{II}, an analogous development gives

$$E_g - E_f = kT \ln \frac{N}{n_1} \tag{6}$$

or

$$n_1 = N \exp\left[-(E_g - E_f)/kT\right] \tag{7}$$

The difference between n_1 and n_2, fixed by the chemical composition of the ferrite, is independent of temperature. The equilibrium between holes and electrons is given by the law of mass action:

$$n_1 n_2 = N^2 \exp(-E_g/kT) \tag{8}$$

Therefore, a cobalt ferrite with a majority carrier concentration appreciably greater than $\sqrt{n_1 n_2}$ will have a negligible concentration of minority carriers and the majority carrier concentration will be practically independent of temperature.

The general expression for the electrical conductivity, σ , for a two carrier semiconductor is

$$\sigma = n_1 e \mu_1 + n_2 e \mu_2 \tag{9}$$

The variation of σ with temperature for $n_1 >> \sqrt{n_1 n_2}$ and $n_2 >> \sqrt{n_1 n_2}$ may therefore be attributed to the variation of μ_1 and μ_2 with temperature.

Insight into the energy level scheme of cobalt ferrite may also be gained by measurement of the Seebeck effect, or thermoelectric power. A temperature difference ΔT between the ends of the sample causes an emf of $\Theta \Delta T$ microvolts, where Θ, the thermoelectric power, is given in microvolts/degree.

The significance of the Seebeck effect is often explained in terms of its inverse, the Peltier effect, which is a measure of the heat absorbed at one semiconductor-metal junction, and liberated at the other, when current is passed through the semiconductor. The Peltier coefficient is expressed in units of joules/coulomb, or volts.

The thermoelectric power and Pelti coefficient, II, are related by the Kelvin relationship

$$\Theta T = \Pi \tag{10}$$

These effects arise from the fact that the energy level of the current carrying electron in the semiconductor differs from that of the metal. In normal band type semiconductors an additional term must be added to account for the transfer of kinetic energy of the carriers in moving from a hot to a cold region. In a localized level semiconductor, Jonker[45] indicates that a similar additional term must be added to account for the transport of the energy in excess of that indicated by the electron levels. He further points out that not only is it difficult to predict the magnitude of the contribution of the activation energy, q, to the transport energy, but even the sign of the contribution may be in doubt, since the activation energy may be associated with either the emitting or receiving ion. If the energies, α and β, are associated with

the transport of electrons and holes respectively, Jonker[45] points out that the Peltier effect for cobalt ferrite is given by

$$\Pi = \frac{-n_1\mu_1(E_g - E_f + \alpha) + n_2\mu_2(E_f + \beta)}{n_1\mu_1 e + n_2\mu_2 e} \tag{11}$$

In the concentration ranges where one type of carrier predominates Equation (11) reduces to

$$e\Pi = e\Theta T = -(E_g - E_f + \alpha) \qquad n_1 >> n_2 \tag{12}$$

or

$$e\Pi = e\Theta T = (E_f + \beta) \qquad n_2 >> n_1 \tag{13}$$

Combining Equations (5), (13) and (7), (12) gives

$$e\Theta T = -\alpha - kT \ln \frac{N}{n_1} \qquad n_1 >> n_2 \tag{14}$$

for an n-type ferrite, and

$$e\Theta T = +\beta + kT \ln \frac{N}{n_2} \qquad n_2 >> n_1 \tag{15}$$

for a p-type ferrite.

Jonker[45] reports that both α and β are linear functions of temperature. Therefore, Equations (14) and (15) can be solved for Θ to give

$$\Theta = \frac{k}{e}\left[\ln \frac{N}{n_1} + \alpha'\right] \qquad n_1 >> n_2 \qquad (16)$$

or

$$\Theta = \frac{k}{e}\left[\ln \frac{N}{n_2} + \beta'\right] \qquad n_2 >> n_1 \qquad (17)$$

In the temperature range for which Equations (5) and (7) apply, Equations (16) and (17) predict that Θ will be independent of temperature. Jonker[45] found the Seebeck effect for cobalt ferrite to be temperature independent between room temperature and 160°C.

The difference between the band type and localized level type semiconductors is emphasized by a plotting Θ vs n, for various materials (Figure 2, from Jonker[46]). The theoretical slope, of 198 μv/°C. per decade of concentration, is observed for all cases. At the intersection of the extrapolated lines with the abscissa, as can be seen from Equations (16) and (17), n is approximately equal to N, the number of sites available for electrons or holes. Band theory predicts a value for N given by

$$N = 2\left[\frac{2\pi m^* kT}{h^2}\right]^{3/2} \qquad (18)$$

If m* = 1, at room temperature, N = 2.5 x 10^{19} cm^{-3}. The CdS(Kroger et al.(55)), PbS(Bloem(11)) and CdTc(de Nobel(17)) curves, Group I in Figure 2 , intersect the abscissa at approximately this value.

The localized level semiconductor, Group II in Figure 2, including data on NiO(van Houten(97)), $COFe_2O_4$(Jonker(45)), $Fe_2O_3TiO_2$ and $LaFeO_3$(Jonker(44)), intersect the abscissa at extrapolated values of N = 10^{22} which is approximately equal to the number of metal ions/cc. present in the oxide. This emphasizes the different character of the two groups of semiconductors.

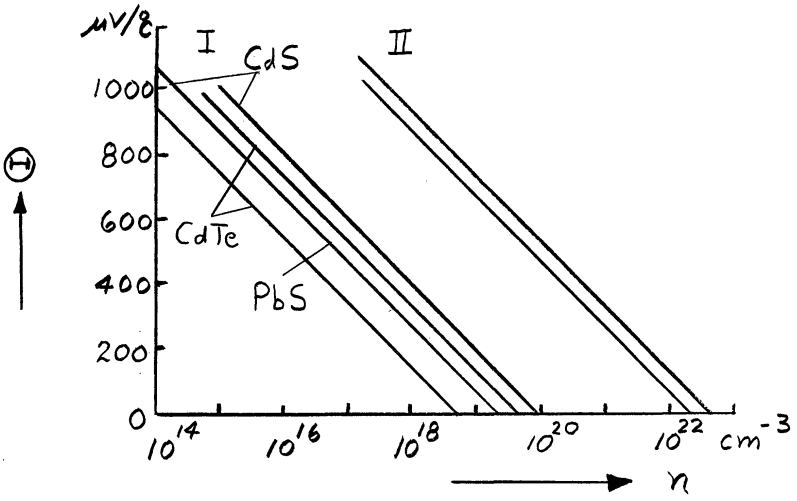

Figure 2 . Schematic Survey of the Seebeck Effect of a Number of Compounds as a Function of Hole Concentration, n, Extrapolated to the Intersection Points With the Abscissa.

From measurements of both electrical conductivity and thermoelectric power, Jonker[45] calculated a set of values of the pertinent parameters which characterize the room temperature semiconducting properties of $Co_{3-x}Fe_xO_4$. (See Table I).

TABLE I.

Constants Needed to Describe the Semiconducting Properties of $Co_{3-x}Fe_xO_4$.

E_g = 0.55 ev

α = 0.025 ev = 1 kT

β = 0.15 ev = 6 kT

q_1 = 0.205 - 0.175 ev

q_2 = 0.51 - 0.475 ev

μ_1 = 0.7 - 1.3 x 10^{-4} $cm^2/v.sec.$

μ_2 = 0.6 - 2.1 x 10^{-8} $cm^2/v.sec.$

ν_1 = 6.5 x 10^{12} $sec.^{-1}$

ν_2 = 1.0 x 10^{14} $sec.^{-1}$

μ_1/μ_2 = 10^4

The energy gap, E_g, of cobalt ferrite may be estimated by calculating the energy change in the valency reaction

$$Co^{II} + Fe^{III} \longrightarrow Co^{III} + Fe^{II}.$$

$$E_g = I_3(Co) - I_3(Fe) + \Sigma \text{ c.f.} \qquad (19)$$

where I_3 refers to the third ionization potential and $\sum$ c.f refers to the crystal field stabilization energies. If I_3 values from Finkelnburg and Humback[27] and $\sum$ c.f from Jonker and von Houten[46] are used, the calculations give E_g = 33.49 - 30.64 - 1.5 = 1.35 ev.

This value compares reasonably well with Jonker's experimental value of E_g = .55 ev, since elastic energy contributions have been neglected. Jonker and von Houten[46] also point out that, since the acceptor levels are completely ionized at room temperature in samples with an excess carrier concentration as high as 10%, E_a and E_d must be smaller than 0.06 ev.

B. The Effect of Chemisorption on Thermoelectric Properties

The preceeding development assumes that only one type of donor or acceptor level exists. However, the electron transfer associated with the adsorption of either donor or acceptor atoms would introduce other levels on the surface of the ferrite. These surface states, due to the nature of the bond formed between the adsorbed ions and the surface (which might be characterized by the degree of electron sharing, or degree of covalent bonding), might be at energy levels which are different from the donor and acceptor levels formed in the semiconductor due to additions of excess Fe^{II} or Co^{III} to the crystal structure. Assuming that these surface acceptor states, N_B, are all at the energy level, E_b, the application of Fermi statistics in the surface region gives

holes in valence = electrons in acceptor level A + electrons in acceptor level B + electrons in conductor band

$$\frac{N}{1+\exp\left[\frac{E_f}{kT}\right]} = \frac{N_A}{1+\exp\left[\frac{E_a-E_f}{kT}\right]} + \frac{N_B}{1+\exp\left[\frac{E_b-E_f}{kT}\right]} + \frac{N}{1+\exp\left[\frac{E_g-E_f}{kT}\right]} \qquad (20)$$

At low temperatures, the last term may be neglected and the resulting equation is cubic in $\exp(-E_f/kT)$. For the temperature range in which $E_a \ll kT$, $E_b \ll kT$, this cubic equation can be solved for E_f to give

$$E_f = kT \ln \frac{N}{N_A+N_B} \qquad (21)$$

Equation (21) is analogous to the previous case, but the denominator now contains the total number of acceptor states, due to excess Co^{III} and due to adsorption. A similar solution may be derived for the n-type material. Therefore, in the temperature range where both E_a and E_b are much smaller than kT, an increase in the number of acceptor atoms adsorbed on the surface is analogous to an increase in the number of holes (Co^{III}), and an increase in the donor atoms on the surface corresponds to an increase in the number of electrons (Fe^{II}). Thus the Fermi level at the surface is related to both the stoichiometry and the degree of adsorption.

Huston[43] points out that, although the thermoelectric power is sometimes thought of as characteristic of the bulk material, in the case of a compressed powder or sintered sample a large fraction

of the total temperature drop through the sample would probably be localized at the sintered "necks" or regions of particle to particle contact. Consider, for example, a compressed powder, such as illustrated in Figure 3 . The space charge layer, formed as a result of the electron transfer between the adsorbed gas and the surface, is indicated by the shaded borders of the particles. One would not expect the temperature gradient within such a compressed powder to be uniform. If an idealized spherical particle is considered, Parravano and Domenicali[74] point out that the temperature distribution in a collinear row of particles will resemble the distribution given in Figure 4 . The solid lines inside the spheres (Figure 4a) represent isothermal surfaces, and the dashed curves represent lines of heat flow. Figure 4b shows qualitatively the temperature variation along a line connecting the centers of a collinear row of particles. This model illustrates that the temperature gradient in the region of particle to particle contact may differ appreciably from the gradient farther inside the particle, causing the measured thermoelectric power to be "weighed" heavily in favor of the contact region. If this were the case, this surface layer contribution to the thermoelectric power would be large. Parravano and Domenicali[74] measured the thermoelectric power of powdered NiO under different gas atmospheres and presented a theoretical analysis showing how the ratio between the thickness of the space charge layer at the semiconductor surface and the "thickness" of the thermal gradient affects the change in

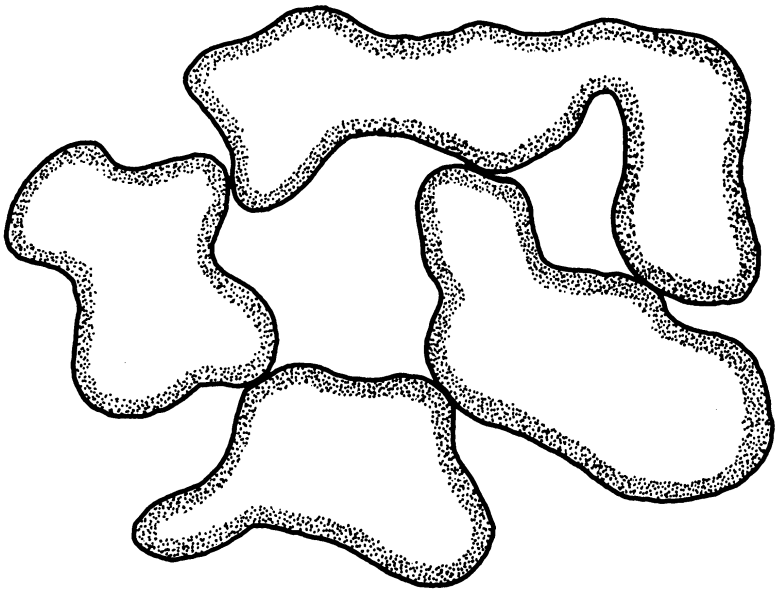

Figure 3. Cross Section of Compressed Powder Sample. (Shading Indicates Space Charge Region)

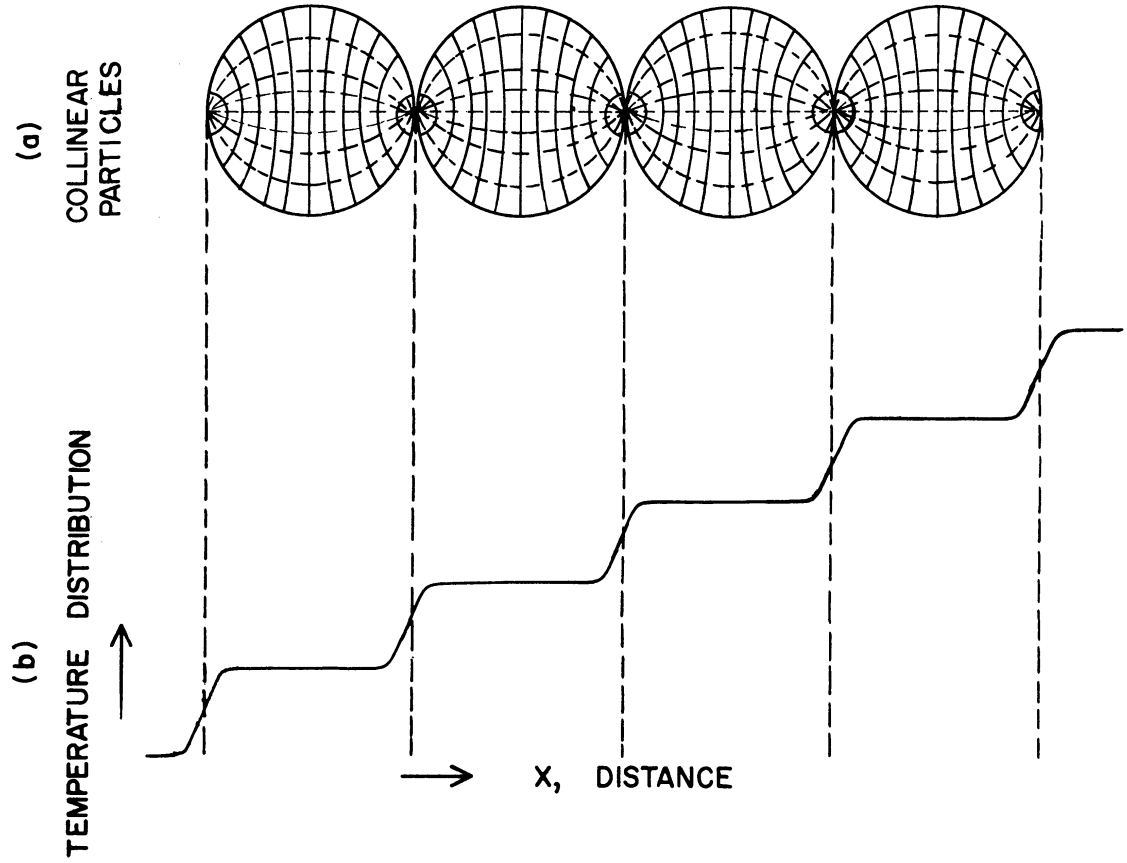

Figure 4. Temperature Distribution in Idealized Spherical Particles(74).

thermoelectric power resulting from chemisorption. A similar study on the thermoelectric behavior of pellitized 60 x 10^4 Å germanium particles exposed to oxygen and water vapor has been made by Kmetko[52]. Thus, at the surface of the cobalt ferrite the distance between the conduction band (or valence band) and the Fermi level, indicated by measurements of the thermoelectric power of a compressed, powdered sample, is related not only to the composition (Fe/Co ratio) of the ferrite but also to the amount and type (donor or acceptor) of ions adsorbed on the surface.

C. The Effect of Changes in Fermi Level on Adsorption and Catalytic Activity

Boreskov[12] presented the following derivation of the relationship between the Fermi level and the rate of adsorption and desorption. Consider the adsorption of an atom, A, such as hydrogen, on the surface of an oxide catalyst. The heat to adsorption, Q, is $Q = (\phi - I_a + w)$, where ϕ is the electron work function, I_a is the ionization energy, and w is a term referring to the interaction of the adsorbed atom with the surface. Let us consider the effect on chemisorption of a small change in ϕ associated with a change in the Fe/Co ratio of our ferrite catalyst. We will neglect any change in w and will, at present, not consider any changes of ϕ with surface coverage. The simple band picture of the p-type material is shown in Figure 5.

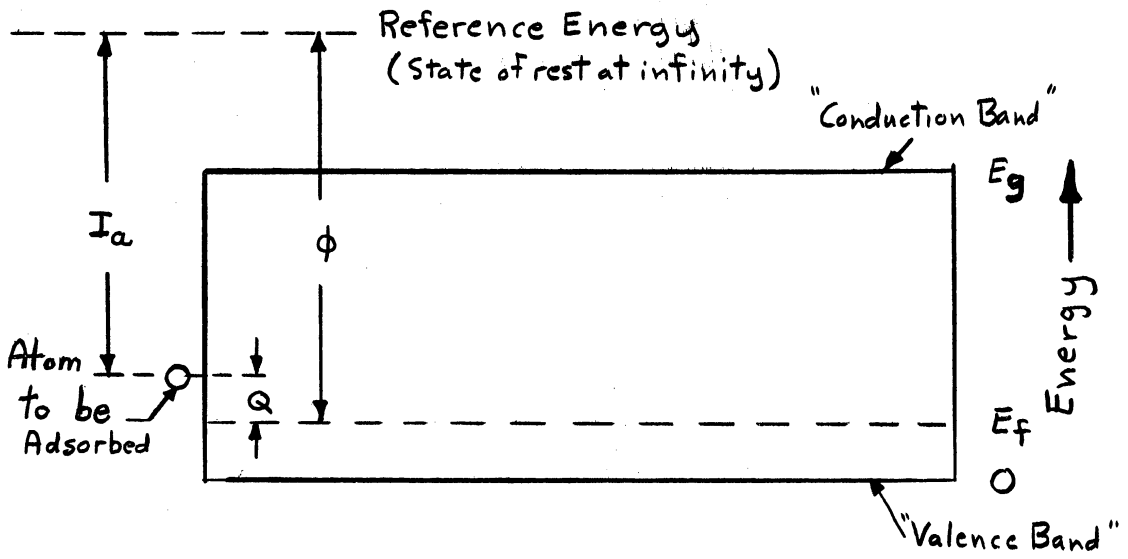

Figure 5. Energy Picture For Adsorption

The change in heat of adsorption will then be equal to the change in Fermi level, E_f, caused by the new Fe/Co ratio.

$$Q = Q_o + \Delta\phi = Q_o - \Delta E_f \tag{22}$$

The degree of surface coverage, assuming Langmuir adsorption, is

$$\theta = \frac{b P_A}{1 + b P_A} \tag{23}$$

where

$$b = b_o e^{(Q_o/kT)} e^{(\Delta\phi/kT)} \tag{24}$$

is the adsorption coefficient and P_A is the pressure of gas A.

The rates of adsorption and desorption are determined by the activation energy of the absorbed complex. This energy also depends on the level of chemical potential of the electrons.

Temkin[95] has shown that a change in activation energy of adsorption forms some part of the change in heat of adsorption.

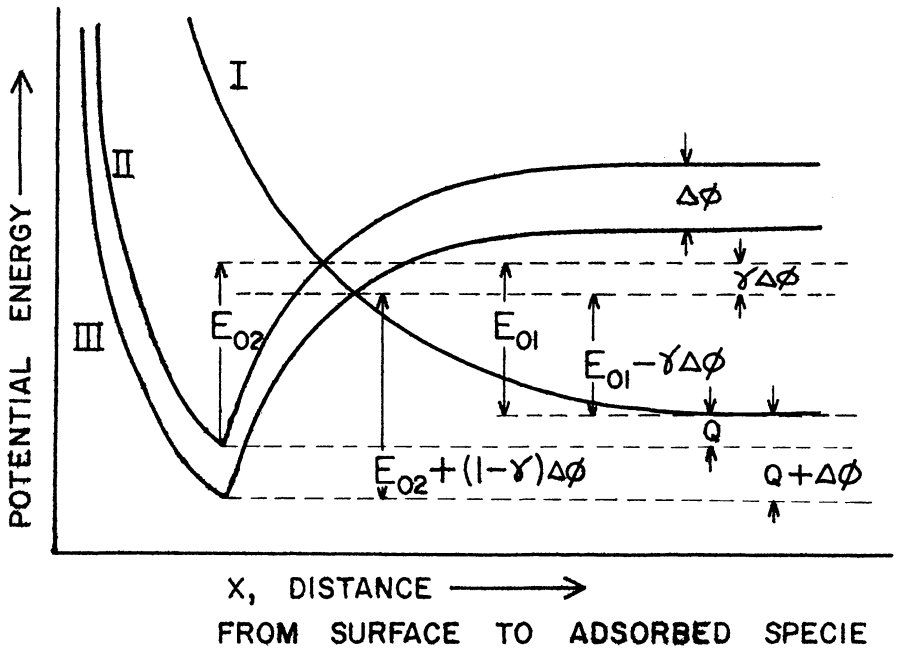

Figure 6. Change in Activation Energy of Adsorption With Changes in Chemical Potential of the Electrons[12].

In Figure 6, curve I represents the Van der Waals interaction energy of the molecule A. As a molecule of A approaches the surface it is acted upon by a repulsive force and thereby increases in potential energy. Curves II and III represent potential energy of the chemically absorbed specie as a function of the distance from the

surface of catalysts with different compositions, i.e., different Fe/Co ratios, in the case of cobalt ferrite. At the intersection of curves I and II (or I and III) the particle will follow the chemically absorbed curve (II or III) if x decreases, and will follow the Van der Waals curve as x increases. This intersection, then, represents the activated complex. The activation energy of adsorption is

$$E_1 = E_{01} - \gamma \Delta \phi \tag{25}$$

and the activation energy for desorption is

$$E_2 = E_{02} + (1-\gamma) \Delta \phi \tag{26}$$

where γ is between 0 and 1.

The rate of adsorption is

$$\omega_1 = k_1 P_A (1-\theta) = k_{01} e^{\gamma \Delta \phi / kT} P_A (1-\theta) \tag{27}$$

The rate of desorption is

$$\omega_2 = k_2 \theta = k_{02} e^{-(1-\gamma) \Delta \phi / kT} \tag{28}$$

At equilibrium

$$\omega_1 = \omega_2 = k_{02} \frac{P_A b_0 e^{Q_0/kT} e^{\gamma \Delta\phi/kT}}{1 + P_A b_0 e^{Q_0/kT} e^{\Delta\phi/kT}} \tag{29}$$

Equation (29) indicates, that at equilibrium, as the work function increases, the rates of adsorption and desorption increase for low degrees of surface coverage, pass through a maximum at $\Theta = \gamma$, and decrease at high degrees of surface coverage.

Boreskov[12] applies these results to clarify the effects of displacement of the Fermi level of oxide catalyst on the activity with respect to the hydrogen-deuterium exchange reaction. If the hydrogen-deuterium exchange can be represented by

$$S(H) + \tfrac{1}{2} D_2 \rightarrow S + HD \tag{30}$$

$$S + \tfrac{1}{2} H_2 \rightarrow S(H) \tag{31}$$

and if Equation (30) is rate controlling, the rate will be given by

$$r = k P_{H_2}^{1/2} \Theta \tag{32}$$

where Θ is the fraction of the surface covered with hydrogen. Since Equation (30) is the rate controlling step, Θ will be given by the equilibrium adsorption isotherm corresponding to Equation (31):

$$\theta = \frac{\sqrt{b P_{H_2}}}{1+\sqrt{b P_{H_2}}} \tag{33}$$

Therefore,

$$r = k P_{H_2}^{1/2}\theta = \frac{k_o P_{H_2}^{1/2}\sqrt{b_o e^{Q/kT} e^{\gamma\Delta\phi/kT}}}{\left[1+\sqrt{b_o e^{Q/kT} e^{\Delta\phi/kT} P_{H_2}}\right]} \tag{34}$$

Analogous equations may be written if the role of H_2 and D_2 in Equations (30) and (31) are interchanged.

If the hydrogen-deuterium exchange is represented by the reactions

$$S(H) + S(D) \rightarrow 2S + HD \tag{35}$$

$$S + \tfrac{1}{2} H_2 \rightarrow S(H) \tag{36}$$

$$S + \tfrac{1}{2} D_2 \rightarrow S(D) \tag{37}$$

when reaction (35) is rate controlling, the rate will be given by

$$r = k\theta^2 \tag{38}$$

where θ is the fraction of the surface covered. In this case,

Boreskov[12] points out that

$$\theta = \frac{\sqrt{b P_{H_2}}}{1 + \sqrt{b P_{H_2}}} \tag{39}$$

and

$$r = k\theta^2 = k_o \frac{b_o e^{Q/kT} e^{\gamma \Delta\phi/kT} P_{H_2}}{\left[1 + \sqrt{b_o e^{Q/kT} e^{\Delta\phi/kT} P_{H_2}}\right]^2} \tag{40}$$

In either case, lowering the Fermi level, which is equivalent to increasing the work function, decreases the activation energy of adsorption and increases the activation of desorption, see Equations (25) and (26). Therefore, in regions of low surface coverage, ($\theta < \gamma$) lowering the Fermi level should increase the catalytic activity (see Equations (34) and (40).

D. Determination of Activation Energy and Pre-exponential Factor

The kinetic data for the reaction $H_2 + D_2 \rightarrow 2HD$ were computed from the percentage conversion p, defined as

$$p = \frac{\left(\frac{[HD]}{[H_2]}\right)_t}{\left(\frac{[HD]}{[H_2]}\right)_t + 2\left(\frac{[D_2]}{[H_2]}\right)_t} \times 100 = \frac{[HD]_t}{[HD]_t + 2[D_2]_t} \times 100 \tag{41}$$

Values of p were determined at three flow rates as a function of temperature. Figure 7 shows a typical data plot. The method of calculating the activation energy and pre-exponential factor is outlined below.

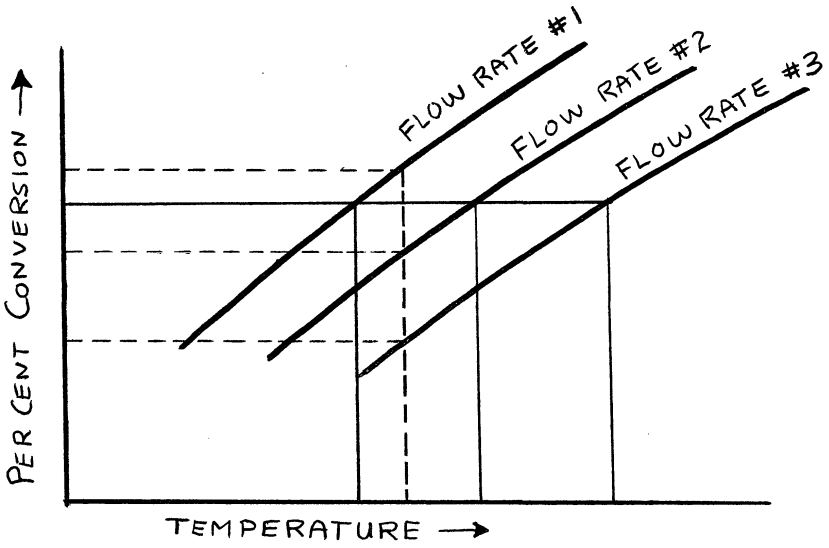

Figure 7. Typical Data Plot.

1. Activation Energy

Values of the activation energy were calculated from flow rates and corresponding temperatures at constant conversion. (See solid lines in Figure 7). If the rate of change in deuterium concentration is assumed to be equal to the first power of the deuterium concentration

$$-\frac{d[D_2]}{dt} = k[D_2] \qquad (42)$$

Therefore

$$-\int_{[D_2]_o}^{[D_2]_t} \frac{d[D_2]}{[D_2]} = kt \qquad (43)$$

At constant conversion the integral on the left side of Equation (43) is a constant, A. Writing k in the Arrhenius form, $k = k_o e^{-E/kT}$ and substituting $\frac{V}{v}$ for t, gives

$$kt = A = \frac{V}{v} k_o e^{-E/kT} \qquad (44)$$

where

V = void volume of reactor in cc.

v = flow rate through reactor, cc./min.

The flow rate v_a, measured at ambient temperature and pressure is related to v by:

$$v = \frac{v_a T P_a}{T_a P} \qquad (45)$$

Therefore

$$A = \frac{k_o V T_a P}{v_a T P_a} e^{-E/kT} \qquad (46)$$

or

$$\ln [v_a T] = -E/kT + \ln \left[\frac{V T_a P k_o}{A P_a}\right] \qquad (47)$$

Since the quantity, $\left[\frac{V T_a P k_o}{A P_a}\right]$ is constant during the run, the activation energy, E, may be determined from the slope, -E/k, of a plot of $\ln[r_a T]$ vs $\frac{1}{T}$. The procedure was repeated for three values of conversion. Note that this method of determining the activation energy is independent of the kinetic order of the reaction (i.e., the assumption of first order kinetics is unnecessary).

2. Preexponential Factor

The preexponential factor was calculated from value of the flow rate and corresponding percent conversion at constant temperature (see dotted lines, Figure 7).

If the reaction is first order,

$$-\frac{d[D_2]}{dt} = k[D_2] \tag{48}$$

or

$$\ln \frac{[D_2]_o}{[D_2]_t} = kt \tag{49}$$

However, since the HD concentration at time = 0 is negligible,

$$\frac{[D_2]_o}{[D_2]_t} = \frac{2[D_2]_t + [HD]_t}{2[D_2]_t} = \frac{1}{1-p} \tag{50}$$

Equation (49) then becomes

$$\ln\left[\frac{1}{1-P}\right] = kt \tag{51}$$

Combining Equations (44), (45) and (51) gives

$$\ln\left[\frac{1}{1-P}\right] = \frac{k_o V T_a P}{v_a T P_a} e^{-E/kT} \tag{52}$$

Since the temperature is a constant, a plot of $\ln\left[\frac{1}{1-P}\right]$ vs. $\frac{1}{v_a}$ results in a straight line of slope m, where

$$m = \frac{k_o V T_a P}{T P_a} e^{-E/kT} \tag{53}$$

The pre-exponential factor, k_o, can then be calculated, since

$$\ln k_o = E/kT + \ln\left[\frac{m T P_a}{V T_a P}\right] \tag{54}$$

This procedure was repeated for three values of temperature.

E. Isotopic Analysis By the Mass Spectrometer

The analysis of hydrogen isotopes on the mass spectrometer was developed by Bleakney[9]. Since this technique is frequently used in tracer studies, it has been developed to a high accuracy, and, in some laboratories, is a routine method. A detailed descrip-

tion of isotopic analysis by a mass spectrometer has been given by Kirshenbaum[50]. A brief outline of the factors which are involved is presented below.

When the mixture of H_2, HD and D_2 enters the mass spectrometer, monotomic, diatomic, and triatomic hydrogen ions are produced (see Table II).

TABLE II. Ions From a Mixture of the Hydrogens in Which H is More Abundant Than D[50].

Ion	Mass	Intensity	Dependence of Peak Height on Pressure
H	1	weak	a_1P+, b_1P^2
H_2	2	very strong	a_2P
D	2	very weak	$a_3P+b_3P^2$
H_3	3	weak	b_4P^2
HD	3	weak	a_5P
D_2	4	very very weak	a_6P
H_2D	4	very very weak	b_5P^2
HD_2	5	very very weak	b_6P^2
D_3	6	very very weak	b_7P^2

The height of the peak at a particular mass number is proportional to both the number of molecules having that mass and the ionization efficiencies of the molecules. In the case of the hydrogen isotopes, the peak height is a function only of the number of molecules, since the ionization efficiencies of hydrogen and deuterium do not

measurably differ[50], (77), (96).

The H_2, HD, D_2 mixture used in this study was approximately 98% H_2. Table II shows concentration of the various ions present in the mass spectrometer as a function of pressure. The peak height I, for masses 2, 3, and 4, are, therefore given by

$$I_2 = a_2 P \tag{55}$$

$$I_3 = a_5 P + b_4 P^2 \tag{56}$$

$$I_4 = a_6 P \tag{57}$$

Since the gas is 98% H_2, $P \cong I_2/a$ or

$$I_3 = \left[\frac{a_5}{a_2}\right] I_2 + \left[\frac{b_4}{(a_2)^2}\right] I_2^2 \tag{58}$$

or

$$\frac{I_3}{I_2} = \left[\frac{a_5}{a_2}\right] + \left[\frac{b_4}{(a_2)^2}\right] I_2 \tag{59}$$

Therefore

$$\frac{I_3}{I_2} = \frac{[HD]}{[H_2]} + \frac{[H_3]}{[H_2]^2} I_2 \tag{60}$$

If the results of analyses made at different pressures are plotted, the intercept of an $\frac{I_3}{I_2}$ vs. I_2 graph will equal $\frac{[HD]}{[H_2]}$

For a 1-2% D_2 mixture, $\left[H_2D^+\right] \ll \left[D_2\right]$ and may be neglected.

Therefore

$$\frac{I_4}{I_2} = \frac{a_6}{a_2} = \frac{[D_2]}{[H_2]} \tag{61}$$

Nier, Stevens, and Rustad[70] indicate that it is desirable to operate the mass spectrometer at sufficient high pressures to minimize dilution or memory effects, which become pronounced at low pressures.

III. EXPERIMENTAL APPARATUS AND TECHNIQUES

A. Kinetic Experiments

1. Catalyst Preparation and Analysis

Reagent grade cobalt carbonate (J. T. Baker Co.) and iron oxide (General Chemical Division, Allied Chemical and Dye Corporation) were weighed out, mixed, and wet ball milled in acetone (in a Szegvari Attritor, Type SV, Size 01, Union Process Company) for four hours. An analysis of the cobalt carbonate and iron oxide is given in Table XVI, Appendix V. The sample was then dried overnight. The resulting cake was crushed into a powder, loaded in platinum boats, and fired at 1050°C. for four hours in air in a Harper Model HL 7618 furnace (Harper Electric Furnace Corporation) controlled by a Brown Electronik Controlled (Minneapolis Honeywell Model 152C15PS-226-91Q2). The material was crushed with a motar and pestle and put through a No. 40 mesh screen.

The resulting powder was poured into a 3/8" diameter die, and compressed at a pressure of 20,000 psi (Buehler Ltd., Type 1315AB Hydralic Specimen Mount Press) to form pellets, 3/8" diameter, and approximately 1/2" high. These pellets were then placed on top of a layer of the No. 40 mesh powder in platinum boats and fired at 1350°C. for ten hours in air in a Burrell high temperature furnace Type B-7 (Burrell Technical Supply Co.). The samples were then quenched in air. The resulting sintered pellets were crushed and screened, and

the fractions that would pass a No. 40 mesh screen but would not pass a No. 100 mesh screen were used as the catalyst in the hydrogen-deuterium exchange studies.

The surface area of the catalyst powder was measured using nitrogen adsorption at liquid nitrogen temperatures. The results were plotted according to B. E. T. theory. The density of the catalyst was measured in a 10 cc. picnometer.

Catalyst samples were made having four different Fe/Co ratios. The Fe/Co ratios were determined by comparing the catalyst pellets to three pellets with known Fe/Co ratios by means of a Norelco X-ray Flourescent Spectrometer (Phillips Electronics, Inc. Type 42202). The three pellets with known Fe/Co ratios were made from the same starting materials as the catalysts. However, they were wet ball milled in acetone for ten hours, and then pressed at 4,000 psi into 1" pellets. The catalyst pellets were mounted in bakelite and polished with a fine diamond polishing wheel. The samples were then analyzed twelve times on each side. In order to check the homogeniety of the pellets, two samples were rough surface ground (600 A paper) and then polished with the fine diamond wheel, exposing a new layer of material, between each analysis.

X-ray diffraction patterns were taken to determine the crystal structure of the powder samples and microscopic examination of the polished surfaces of the pellets were made.

2. Apparatus

A diagram of the kinetic study apparatus is shown in Figure 8. The cylinder of prepurified hydrogen (Matheson Company,

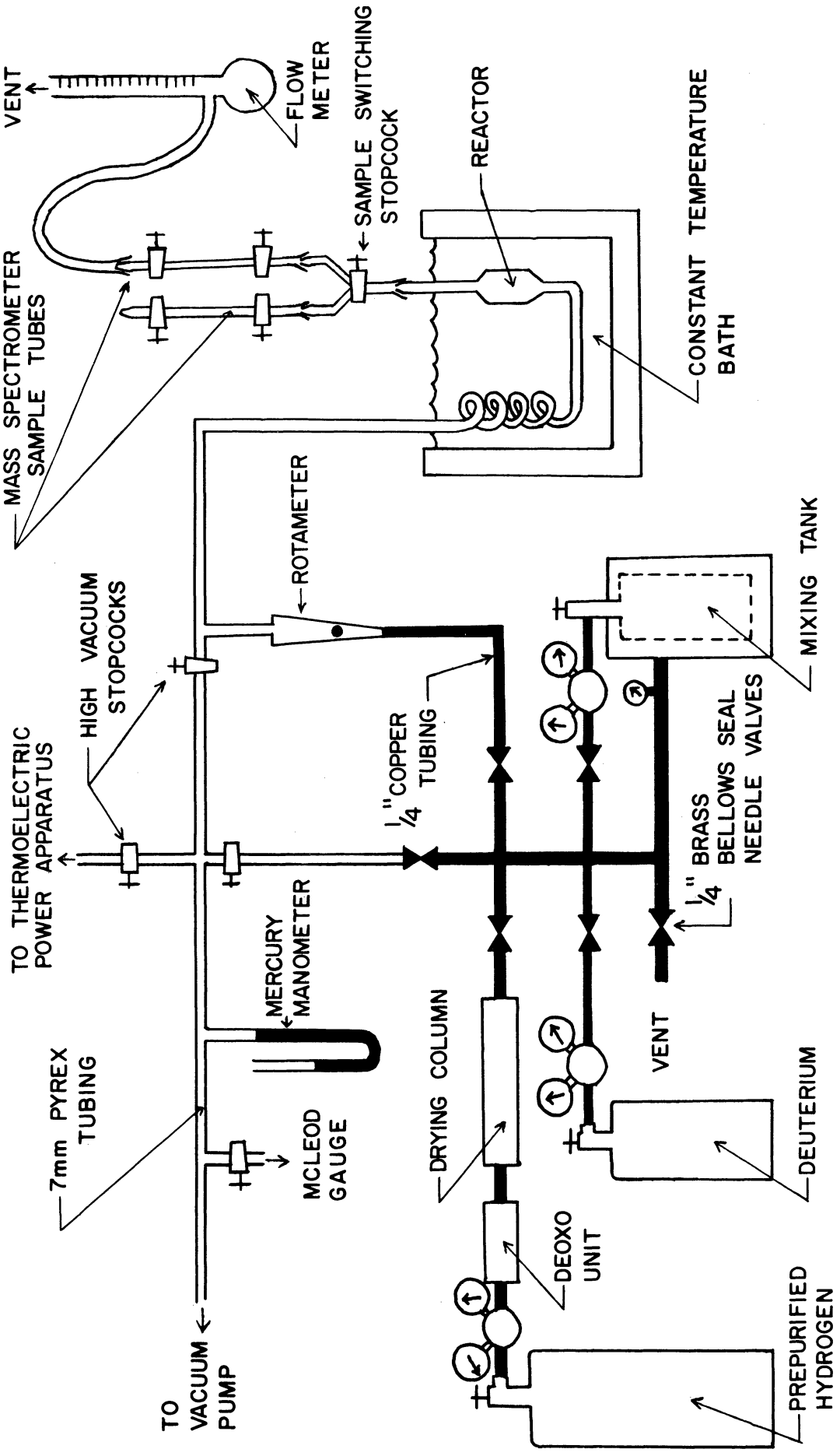

Figure 8. Kinetic Study Apparatus.

Inc.) was specified by the Matheson Company to be 99.9% pure and to contain less than 20 ppm oxygen. The purity of deuterium (General Dynamics Corporation) was specified by General Dynamics Corporation to be 99.5%. The pressure of the gases leaving these cylinders was controlled by Matheson No. 1 single stage pressure regulators. The hydrogen then passed through a Deoxo Type 5-50 catalytic hydrogen purifier (Baker and Company, Inc.) which was designed to reduce the oxygen content of the hydrogen stream to less than one ppm. The oxygen content of the hydrogen at this point was below the level which could be detected on the mass spectrometer, 10 ppm. The water formed in the Deoxo unit was removed from the hydrogen stream in a phosphorus pentoxide drying column. The gas flowed through 1/4" copper tubing with brass compression fittings and 1/4" helium leak tested brass bellows seal needle valves (Hoke, Type A433) into a glass lined mixing tank. The pressures of hydrogen and deuterium were regulated so that a 2% deuterium 98% hydrogen mixture was formed in the mixing tank at a total pressure of 60 psi. Flow of the hydrogen-deuterium mixture from the mixing tank was manually regulated by a Matheson No. 1 pressure regulator and 1/4" needle valve and was measured by a rotameter (Fischer and Porter, Precision Bore Flowrator).

In the low pressure side of the flow system, downstream from the rotameter, the gas flowed through 7 or 8 mm Pyrex tubing fitted with high vacuum oblique bore stopcocks (Pyrex brand No. 7544). The gases then passed into the preheating coil and

reactor, which were contained in a constant temperature bath. A sample of the gas stream was taken as it left the reactor. The gas then passed through a soap bubble flowmeter in which the volumetric flow rate was measured, and was then vented. A vacuum pump (Cenco Hyvac-7) was connected to the system to facilitate removing air from the lines and sample tube before each run.

The copper high pressure side of the system, including the mixing tank, was statically pressure tested at 80 psi and the entire system was tested with a vacuum of 10^{-4} mm Hg., measured by a McLeod fitting type vacuum gage (Scientific Glass Apparatus Company, Inc.). The system was also checked with a helium leak detector (Consolidated Electrodynamics Corporation Type 24-210).

Details of the mixing tank are shown in Figure 9. A Pyrex glass mixing vessel was chosen since the hydrogen-deuterium exchange reaction is not appreciably catalyzed by Pyrex glass at room temperature. A double walled vessel, able to withstand a pressure as high as 80 psi, was designed. The pressure in the annulus between the glass inner vessel and the steel outer shell was manually controlled so that the pressure differential across the glass did not exceed 5 psi. The outer shell was fabricated from 5" O. D. heavy wall steel pipe. A 1/2" thick steel bottom plate was welded to the pipe. The 1/2" thick top plate was attached with eight 1 1/2" 8-32 steel bolts. The rubber gasket between the top plate and the steel shell was coated with SEAL-ALL (Allen Products Corporation) to prevent leakage. The glass inner

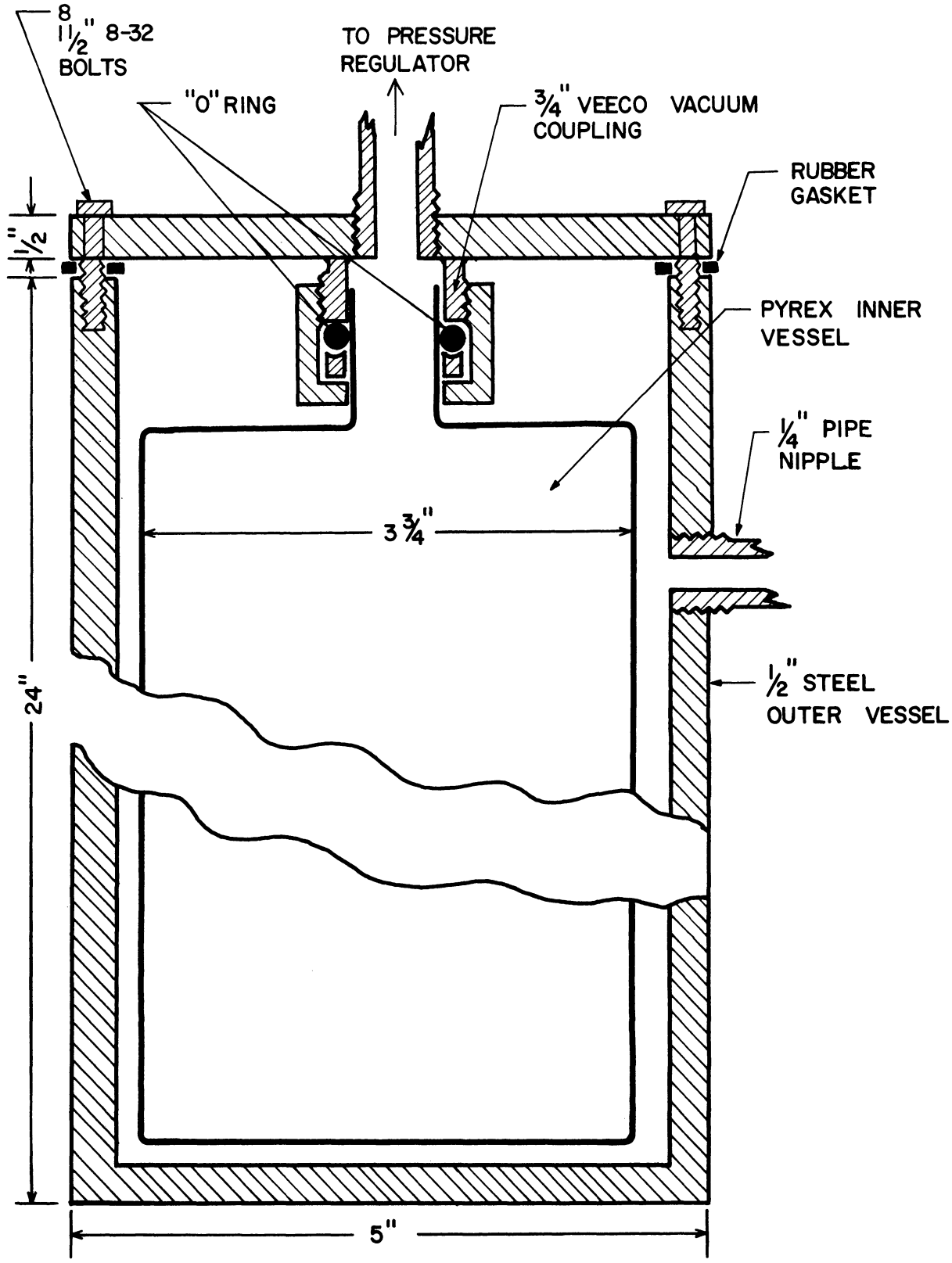

Figure 9. Mixing Tank Details.

vessel was held in place by means of a 3/4" Veeco vacuum coupling (Vacuum Electronics Corporation) which was silver soldered to the top plate. Gas entered the annulus through a standard 1/4" pipe fitting. The annulus gas pressure was measured by a 0-100 psi pressure gauge (U. S. Gauge Co.). The pressure of the hydrogen-deuterium gas mixture in the inner glass vessel was measured by the pressure gauge in the Matheson No. 1 pressure regulator which was attached to the top plate by means of steel pipe fittings.

Details of the constant temperature bath and reactor vessel are shown in Figure 10. A 2000 ml. stainless steel beaker was clamped to an aluminum support rod. An asbestos shell, with walls 1 1/2" thick, was fabricated to fit snuggly around the stainless steel beaker. This insulating shell, attached to the aluminum support rod with an adjustable slide, could be removed to facilitate rapid cooling of the bath. A 1 1/2" thick asbestos lid was constructed. The stainless steel beaker was filled to approximately 1" of the top with Dow Corning 550 heat stable silicon fluid. The current input to the 250 watt knife type immersion heater (Cenco Cat. No. 16551) was regulated by a gas thermometer type thermoregulator and relay (Supersensitive Relay No. 4-5400, American Inst. Company, Inc.). Agitation was provided by a variable speed stirrer (Eastern Industried Inc. Model 3). The bath temperature was measured with a Chromel P-Alumel couple in conjunction with a Leeds and Northrop type 8662 portable potentiometer. The hydrogen-deuterium gas mixture was preheated to the

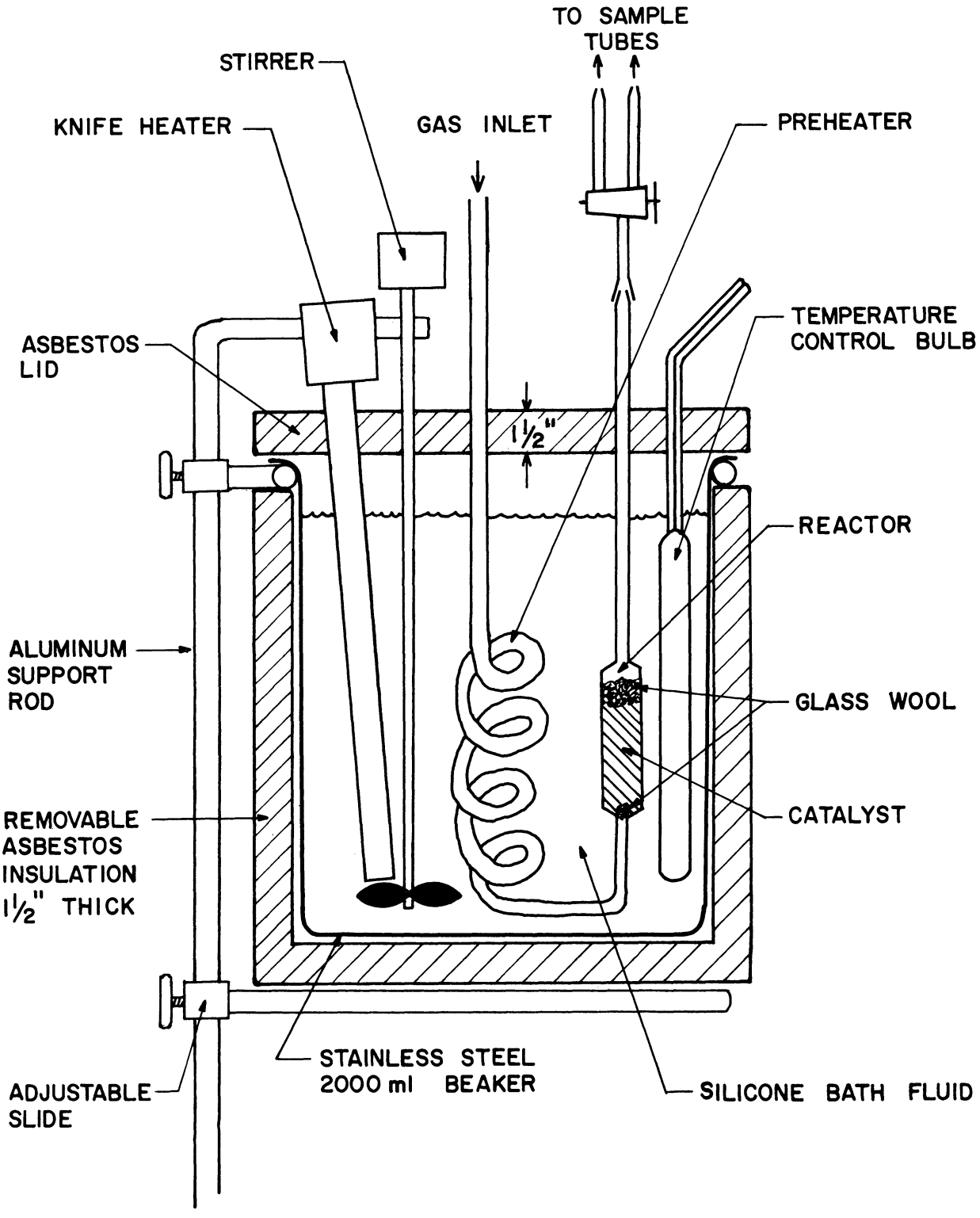

Figure 10. Reaction Vessel Details.

bath temperature in a coil of 7 mm Pyrex tubing and then passed through the reactor. The reactor was a section of Pyrex tubing, 25 mm long, with the diameter enlarged to 10 mm. A slight constriction in the line below the reactor supported a small wad of glass wool which, in turn, supported the catalyst. A small wad of glass wool was also inserted on top of the catalyst to prevent the gas from blowing the catalyst out of the reactor.

The temperature controller was essentially a gas thermometer with two electrical contacts in the mercury column, which activated a supersensitive relay, regulating the current to the bath heater. The temperature setting could be controlled by varying the height of mercury in the pressure leg. In order to avoid oxidation of the mercury at the upper electrode, hydrogen was used to fill the bulb.

3. Experimental Procedures

Hydrogen and deuterium were introduced into the mixing tank. The pressures were regulated manually during the filling operation in order to achieve a final pressure of 60 psi, with 2% deuterium, 98% hydrogen in the gas mixture. A weighed amount of catalyst was placed in the reactor and a gas mixture flow of 30 cc/min. was started through the reactor. After flowing at this rate for 1/2 hour to flush air out of the system, the flow was reduced to 10 cc/min. and the reactor temperature was raised to 200°C. The catalyst was activated for twelve hours at 200°C. The

bath temperature was then lowered to 70-75°C. and held at this temperature for at least four hours.

The catalyst had now been activated and the run was started. The gas flow rate was measured on the soap bubble flowmeter, and the reactor temperature was noted. The stopcocks on the mass spectrometer sample tube were closed, and the sample switching stopcock was turned, diverting the gas flow through the second sample tube. The gas sample was removed and an empty sample tube was put in its place for the next measurement. The experimental conditions (temperature and/or flow rate) were then changed to the next set of desired values. While the system was coming to a new steady state (15-20 minutes), the gas sample was analyzed on the mass spectrometer.

As the run progressed and the pressure in the mixing tank dropped, gas was periodically bled from the annulus so that the pressure differential across the glass inner vessel would not exceed 5 psi. In order to avoid air contamination of the premixed gases, the pressure in the mixing tank was not allowed to fall below 15 psig.

4. Analytical Methods

The analysis of the gas samples were made on the mass spectrometer (Consolidated Engineering Corporation Type 21-013B, Modified to Type 21-103C specifications). A quantitative analysis of a gas mixture is, in general, obtained by comparing the sample cracking pattern against standard samples of the pure components.

However, since the sensitivity of the mass spectrometer for hydrogen and deuterium are approximately equal (13.6 div/μ for hydrogen, 13.5 div/μ for deuterium)[3] in this special case the ratio of peak heights will equal the ratio of partial pressures. If the sensitivity of the spectrometer for hydrogen deuteride is assumed to be also 13.5 div/μ, then the ratio of the peak heights for all three gases in the mixture will equal the ratios of their partial pressures and no standard samples need be run. The validity of this assumption was verified by comparing the mass balances of samples taken before and after reaction.

More specifically, the %D in the unreacted $H_2 + D_2$ mixture was calculated from the mass spectrometer analysis. The sample was then passed over the catalyst and the resulting $H_2 + HD + D_2$ mixture was analyzed on the mass spectrometer. The calculated %D, based on an HD sensitivity of 13.5 div/μ, was then compared to the %D calculated for the unreacted gas.

The most accurate method for determining the composition of $H_2 + HD + D_2$ mixtures, described in the theory chapter, requires that each sample be analyzed four or five times, at different pressures. Since, in following the course of the exchange reaction, a new sample was taken each 15-20 minutes, it was impossible to make multiple analyses of each sample. Instead, all of the samples of any one run were analyzed only once, and each analysis was made using the same gas pressure in the mass spectrometer. This technique would introduce a consistent error (approximately +3%) in the HD

and D_2 analyses which could be eliminated during the calculation of the activation energy and pre-exponential factor, since these calculations involved only differences in percent conversions. (See sample calculations, Appendix II).

B. Thermoelectric Power Studies

1. Catalyst Preparation and Analysis

In order to produce a high surface area ferrite powder for the thermoelectric power studies the following preparation procedure was used. The reagent grade iron oxide and cobalt carbonate were weighed, mixed and then wet ball milled in acetone for four hours. The sample was dried overnight at 120°C. and fired for four hours at 1035°C. in a Harper Model HL7618 furnace. The material was crushed with a mortar and pestle and put through a No. 40 mesh screen. It was then mixed on a rolling mill for seventeen hours. The powder was placed in mullite combustion boats, McDaniel, high temperature mullite, fired in air for eight hours at 1100°C. (Harper Type HL7618 furnace), air quenched, crushed in a mortar and pestle and passed through a No. 40 mesh screen. The powder was then poured into a 3/8" diameter die and compressed at 2,000 psig, into pellets 3/8" in diameter and approximately 1/2" long which were used in the thermoelectric power studies.

The Fe/Co ratio of the powder was determined by chemical analysis. The ferric ion was precipitated from 10% H_2SO_4 solution by cupferron, the ammonium salt of nitrosophenylhydroxyamine, separating the iron from the cobalt. The iron was

then reduced with stannous chloride and titrated with standard potassium dichromate. The cobalt was weighed as cobalt sulfate, obtained by evaporating the oxide with H_2SO_4 and igniting at 550°C.

X-ray diffraction patterns were taken in order to determine the crystal structure of the material.

The surface area of the powder was measured using nitrogen adsorption at liquid nitrogen temperatures. The results were plotted according to B. E. T. theory.

The partial size distribution of the ferrite powder was determined from electron photomicrographs (RCA EML Electron Microscope) at 1100X magnification.

The density of the powder was measured by means of a 10 cc. picnometer.

2. Apparatus

A diagram of the thermoelectric power apparatus is given in Figure 11. The gas inlet manifold was constructed with 7 mm Pyrex tubing, and high vacuum oblique bore Pyrex stopcocks (Pyrex Cat. No. 7544). The prepurified hydrogen used in the hydrogen-deuterium exchange study was also used in this work. The helium (General Dynamics Corporation, 99.5% pure) pressure was regulated by a Matheson No. 1 single stage regulator. The helium was purified by passing it through hot copper oxide 350°C. and activated charcoal cold trap, cooled with dry ice in isopropanol. Pressure measurements were made with a McLeod tilting type vacuum gauge (Scientific Glass Apparatus Company, Inc.) and a

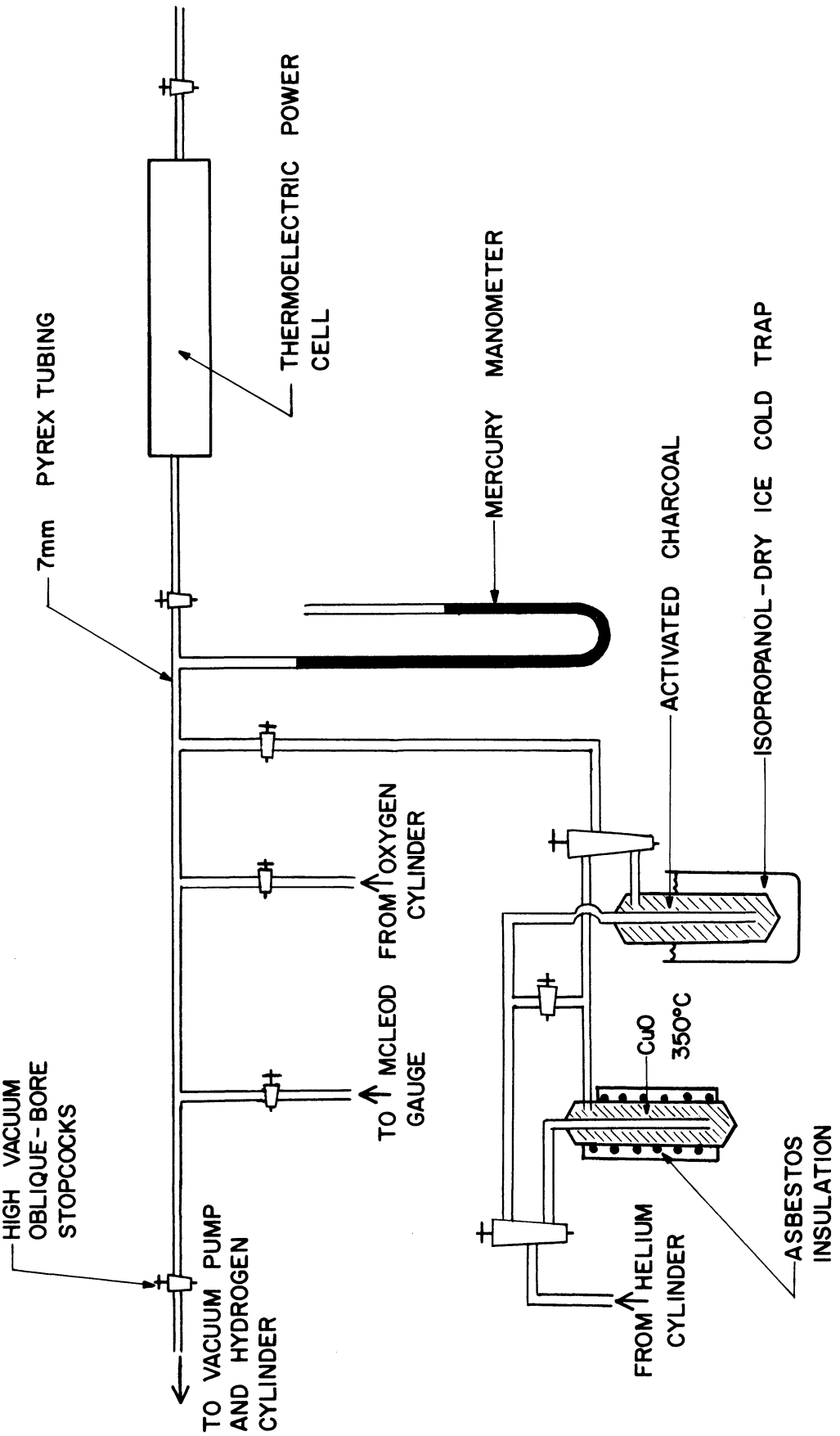

Figure 11. Thermoelectric Power Apparatus.

mercury manometer.

The details of the thermoelectric power cell are shown in Figures 12 and 13. A modified Dresser coupling (Dresser Industries, Inc., Style 65) was used to support the sample holder and Pyrex cover. Tightening the ends of the Dresser coupling forced a copper sleeve to expand the "O" ring, forming a vacuum tight seal between the coupling and the sample holder and Pyrex cover.

The vacuum system and purification train were attached to the cell by an "O" ring seal in a 5/16" Veeco vacuum coupling which was silver soldered over a 5/16" hole drilled in the coupling.

The electrical leads passed through Kovar tubes. The primary coil, made from No. 26 gauge Chromel A heating wire, was wound on the Pyrex envelope and covered by approximately 1/2" of asbestos insulation. The current to this coil was controlled by a variable transformer (Variac Type 200-CM).

Details of the sample holder and electrical wiring are shown in Figure 13. The sample holder was mounted on a stainless steel support which was bolted to the brass sample holder mount. The sample was mounted between two 20 mil. platinum discs (Baker Platinum Division of Englehard Industries), supported by 2 mm. bore capillary Pyrex tubing. These capillary tubes were mounted inside hollow stainless steel cylinders which were welded to the sample holder support. When the sample had been placed between the discs, a stainless steel knob, threaded into the outer cylinder,

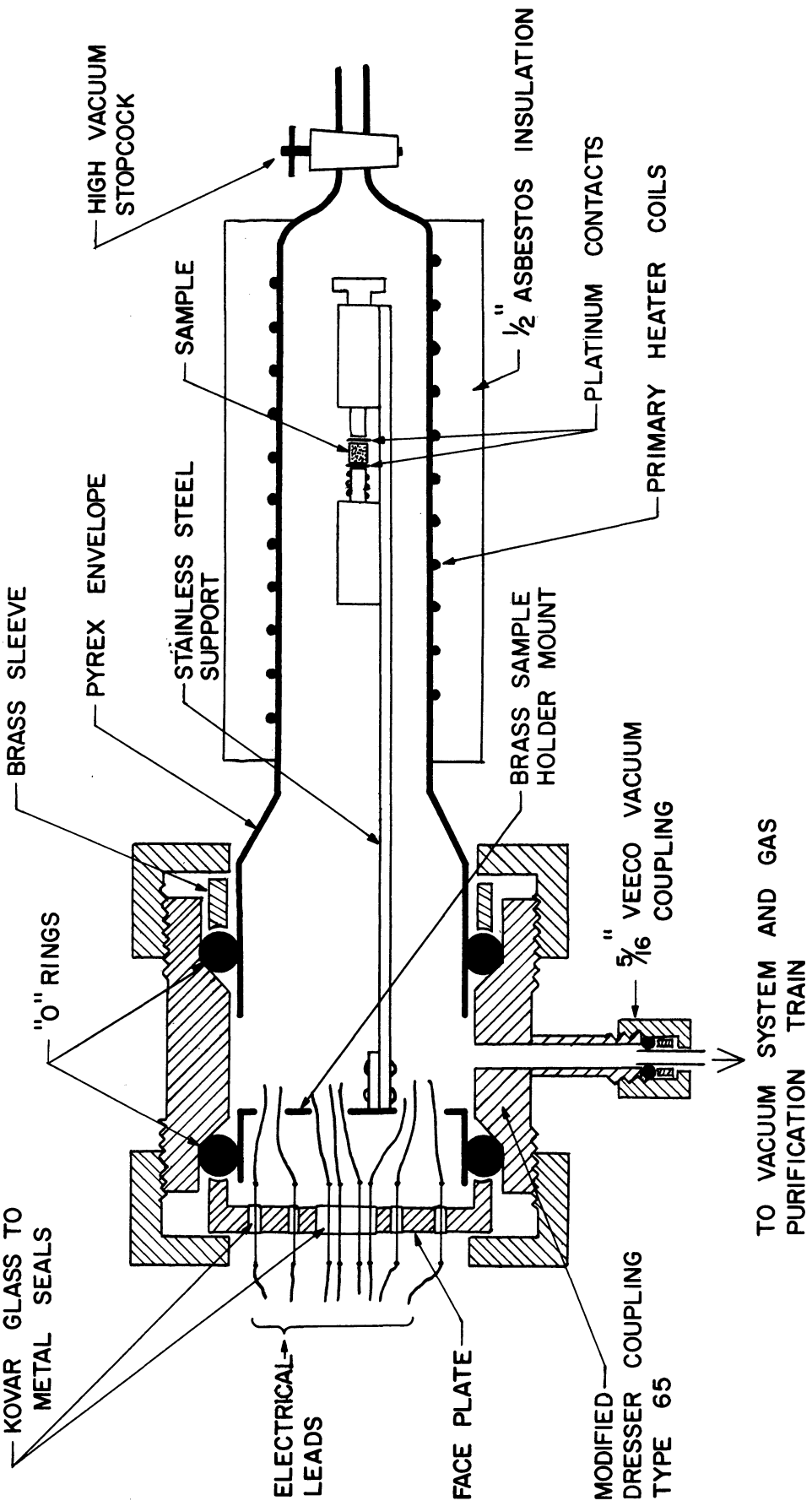

Figure 12. Thermoelectric Power Cell Details.

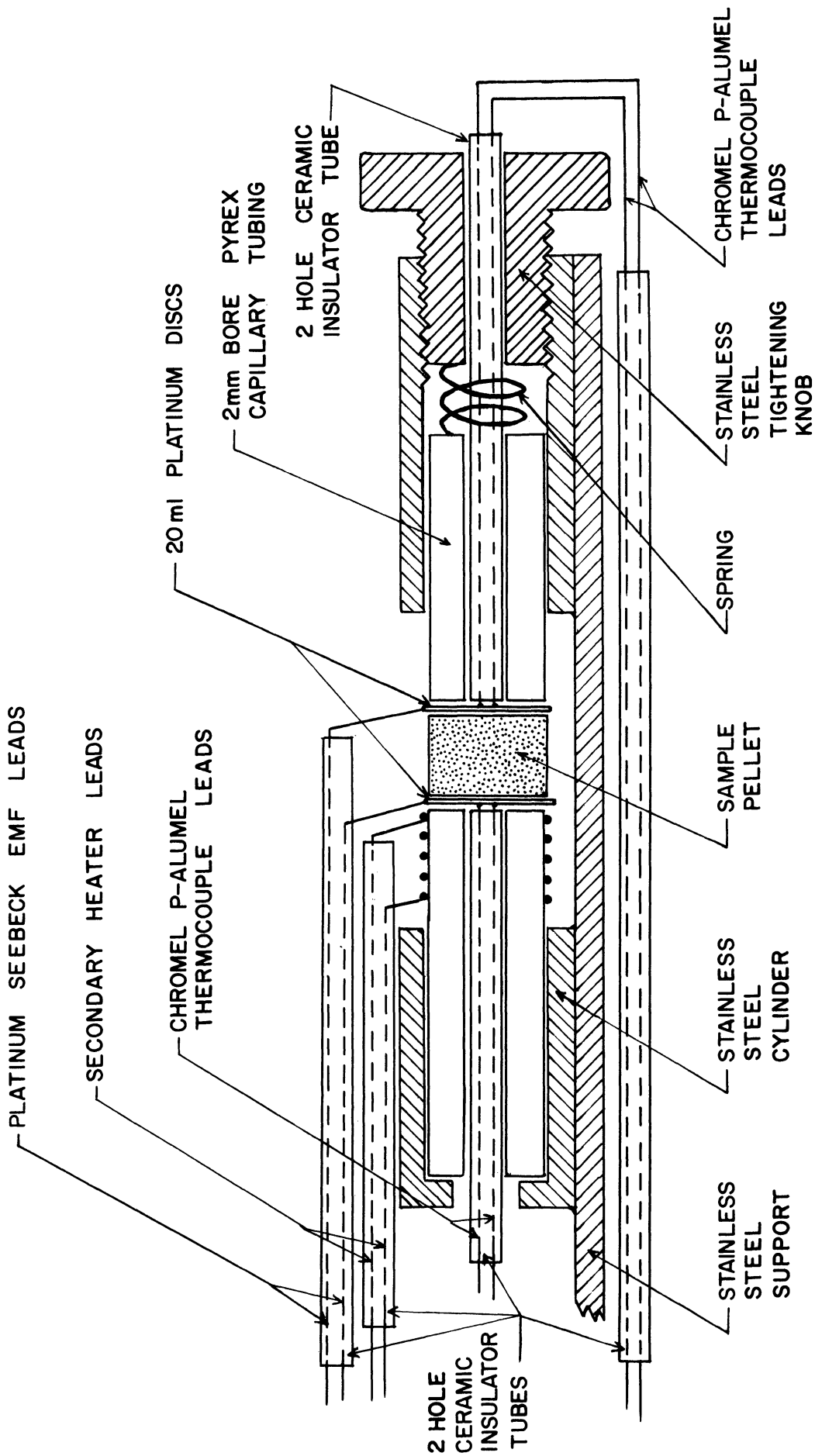

Figure 13. Thermoelectric Power Apparatus; Sample Holder and Internal Wiring Details.

was tightened, firmly clamping the pellet in place. The secondary Chromel A heating coil, controlled by a variable transformer (Variac, Type 200-CM), was wound on the inner glass capillary tube. A No. 40 Chromel-P-Alumel thermocouple (Hoskins Manufacturing Co.) and a No. 30 gauge platinum lead (for EMF measurement) were spot welded on each platinum electrode on the side opposite the sample. The Chromel-P and Alumel leads passed through a 2-holed ceramic insulating tube mounted in the bore of the capillary tubing. The platinum leads were threaded through a similar ceramic insulator which was mounted outside of the stainless steel cylinders. The eight leads (4 thermocouple wires, 2 platinum EMF wires, and 2 secondary heater wires) passed through the brass sample holder mount and through the Kovar glass seals in the face plate.

Details of the external electrical wiring are shown in Figure 12. The Chromel-P-Alumel thermocouple wires lead to the 0°C. cold junction. Copper wires then connected the thermocouple wires to a thermocouple switch (Leeds and Northrup Ten Point rotary switch Cat. No. 8240). The output terminals of this switch were connected to the "B" contacts of a double pole, double throw thermal free switch (Leeds and Northrup Cat. No. 3294). The inner contacts of the DPDT switch were connected to a potentiometer (Leeds and Northrup Type K-3) and electronic DC null detector (Leeds and Northrup Cat. No. 3834).

The platinum EMF wire lead to the inner terminals of a similar double pole, double throw switch. The "A" terminals of

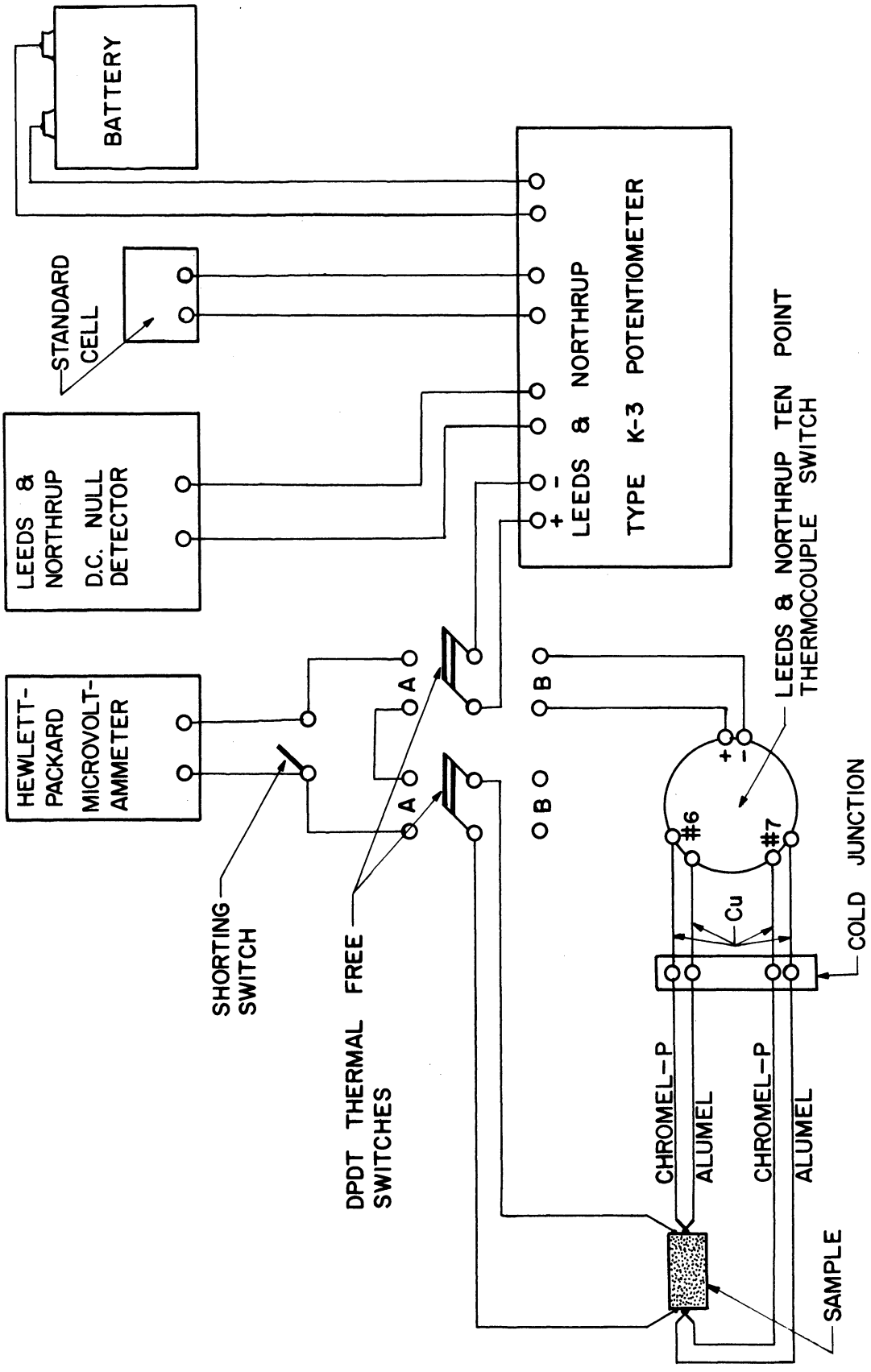

Figure 14. Thermoelectric Power Apparatus, Wiring Diagram.

the two switches were then connected through a DC micro volt-ammeter (Hewlett Packard Model 425A). A switch was provided to short out the micro volt-ammeter for zeroing purposes.

As Figure 14 indicates, when both double pole, double throw switches were connected to terminals "A", and the null detector was switched off, the EMF between platinum discs was measured through the platinum leads by means of the micro volt-ammeter, (used as a null instrument) in conjunction with the K-3 potentiometer. When both double pole, double throw switches were connected to terminals "B", the temperatures on the platinum discs were measured through the Chromel-P-Alumel couples and thermocouple switch, by means of the DC null detector and K-3 potentiometer.

3. Experimental Procedures

To minimize the electrical contact resistance, the ends of the ferrite pellet were first coated with graphite by rubbing with a pencil. This technique was used by Jonker[45]. Van Uitert[98] reported that indium-mercury and graphite form good electrical contacts on ferrite.

The ferrite pellet was clamped between the platinum discs and the Pyrex envelope put in place. The Dresser fitting was then tightened so that the "O" ring made a vacuum tight seal on the Pyrex envelope. The cell was evacuated to 10^{-4} mm Hg. It was then filled with purified helium and evacuated to 10^{-1} mm Hg. This cycle was repeated five times in order to flush any residual air

from the cell. The cell was then filled with helium and the primary heater coil voltage was set at the desired value. The secondary heater voltage was adjusted to impose a temperature difference of 1-3°C. across the pellet. The EMFs were then measured with a Leeds and Northrup Type K-3 potentiometer, coupled with the DC electronic null detector (Leeds and Northrup Cat. No. 3834) for temperature measurements (Chromel-P-Alumel couples), and coupled with the Hewlett Packard Model 425A micro volt-ammeter (used as a high impedence null detector) for the thermoelectric EMF measurement (platinum-ferrite couples). The resistance of the sample and platinum leads was measured with an ohm meter (Triplett, Model 630.

The helium pressure was then reduced to 30 cm. Hg. and 2-6 cm. of hydrogen gas (or oxygen) was introduced. The pressure was increased to 76 cm. H. with prepurified helium. The temperatures, thermal EMF and resistance were recorded as function of time. The measurements were continued until steady state was reached.

The cell was then evacuated (10^{-4} cm), flushed five times with helium, and a helium-oxygen (or hydrogen) mixture was introduced and similar measurements were taken.

Catalyst composition, gas composition and temperature were the independent variables of this study.

C. Experimental Program

The hydrogen-deuterium exchange reaction was initially studied in the 110-130°C. temperature range, using an eight hour

activation time at 200°C. Four different catalyst compositions were used, two p-type and two n-type. Per cent conversion data were taken as a function of temperature at two different flow rates. The activity of the catalyst did not remain constant when data for a third flow rate was taken.

In order to avoid this effect, all subsequent exchange data were taken in the 55-75°C. temperature range, using a twelve hour activation period at 200°C. Using this technique, reproducible kinetics data were taken, as function of temperature, using four catalyst compositions (two p-type, two n-type), three flow rates (10, 15, 20) cc/min.

The thermoelectric power studies, investigating the direction of the change in Seebeck coefficient during gas (hydrogen and oxygen) adsorption, were made in order to gain some insight into the electron transfer process during adsorption. These studies were made as a function of temperature and gas composition, using two catalyst compositions, one n-type and one p-type.

Four hydrogen-deuterium exchange runs were also made on a series of mixed, sintered, p- and n-type ferrite catalysts, to see what effect the formation of p-n junctions in the catalyst would have on the kinetics of the reaction.

IV. EXPERIMENTAL RESULTS

A. Hydrogen-Deuterium Exchange Studies

1. Ferrite Catalyst Characterization

Cobalt ferrite catalyst samples, $Co_{3-x}Fe_xO_4$, having four different compositions were prepared in pellet form, two with $x > 2.0$ and two with $x < 2.0$. The Fe/Co ratios of these samples were determined by comparing the catalyst pellets to samples with known Fe/Co ratios by means of an x-ray flourescent spectrometer. Tables XIV and XV, Appendix IV, shows the Fe/Co ratios and standard deviations which resulted from the twenty-four measurements made on each known sample and each catalyst pellet. Figure 15 is the catalyst composition calibration curve determined by the three samples with known Fe/Co ratios of 0.9/2.1, 1.0/2.0, and 1.1/1.9. The resulting catalyst compositions, $Co_{1.07}Fe_{1.93}O_4$, $Co_{1.03}Fe_{1.97}O_4$, $Co_{0.98}Fe_{2.02}O_4$, and $Co_{0.93}Fe_{2.07}O_4$, are also indicated on Figure 15.

In order to check on the homogeniety of the catalyst pellets, catalyst sample $Co_{0.98}Fe_{2.02}O_4$, was surface ground between each of the twenty-four x-ray analyses in order to expose a new layer of material to the spectrometer. As Table III indicates, no significant difference was observed in the standard deviation of this sample as compared to the standard deviation of the three other catalyst samples, in which the twenty-four measurements were repeated on the same surface.

The thermoelectric power and resistivity of the four catalyst pellet samples were measured. In Figures 16 and 17 the results of these measurements are compared to similar data reported by Jonker[45].

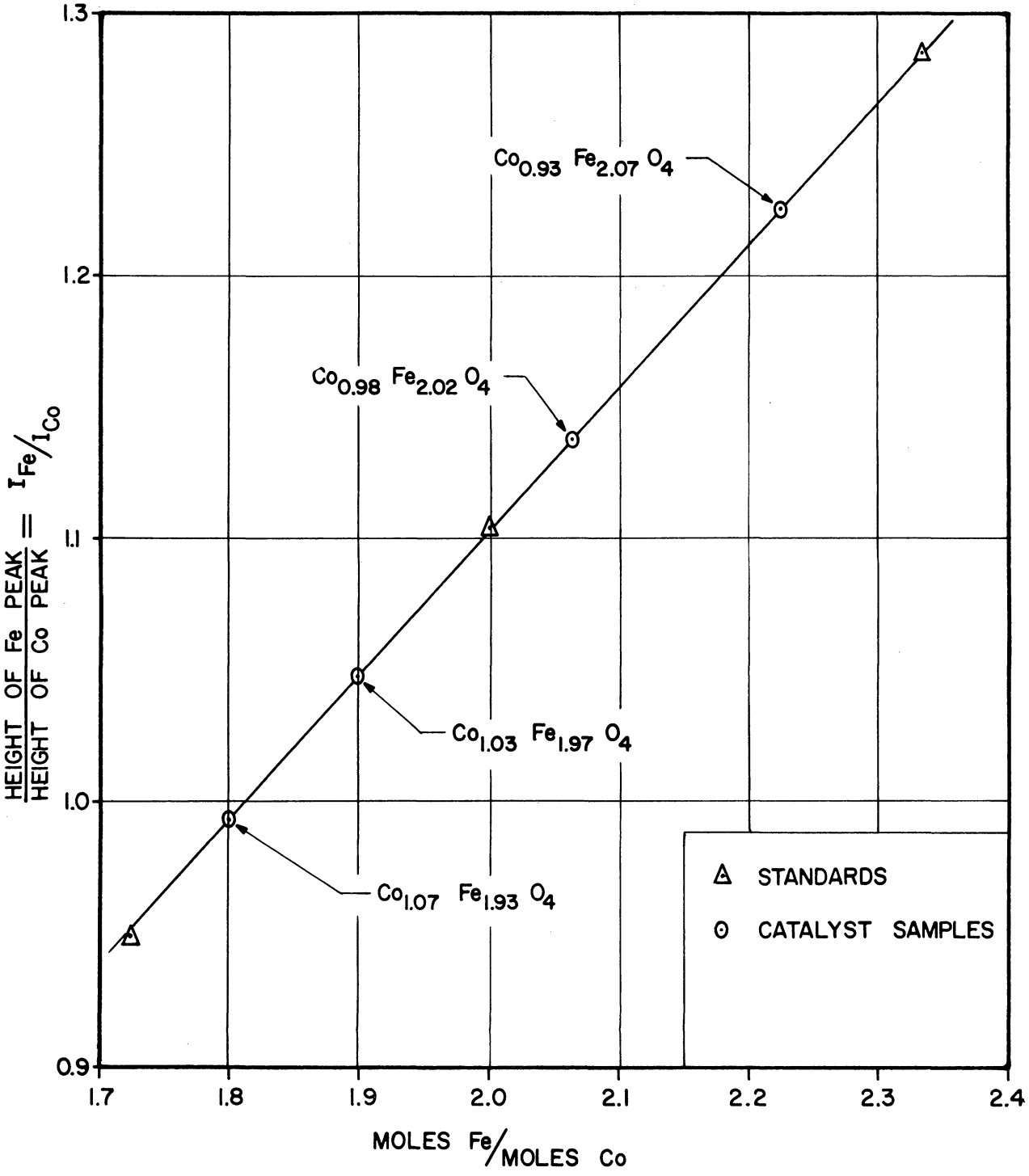

Figure 15. Catalyst Composition Calibration Curve for X-Ray Flourescent Spectrometer Data.

Note that in both Jonker's data and the data of this study an extreme change occurs in both the electrical resistivity and thermoelectric power as the catalyst composition passes through $x = 2.0$. For $x < 2.0$ a high resistivity, p-type ferrite resulted, while for $x > 2.0$ a lower resistivity, n-type ferrite was observed. No variation in thermoelectric power or resistivity during the adsorption of hydrogen or oxygen was observed for these pelletized, sintered samples after 48 hours at 250°C.

TABLE III. Comparison of Standard Deviations of X-Ray Analyses of the Four Catalyst Samples

Catalyst Sample	Side	Peak Height Ratio Fe/Co	Standard Deviation
$Co_{1.07}Fe_{1.93}O_4$	1	1.001	0.0128
	2	0.986	0.0118
$Co_{1.02}Fe_{1.98}O_4$	1	1.053	0.0114
	2	1.043	0.0022
$Co_{0.93}Fe_{2.02}O_4$*	1	1.137	0.0128*
	2	1.140	0.0141*
$Co_{0.93}Fe_{2.07}O_4$	1	1.232	0.0139
	2	1.222	0.0125

*Surface ground between measurements

A microscopic examination of the polished surfaces of the catalyst pellets, and x-ray diffraction patterns of the samples of

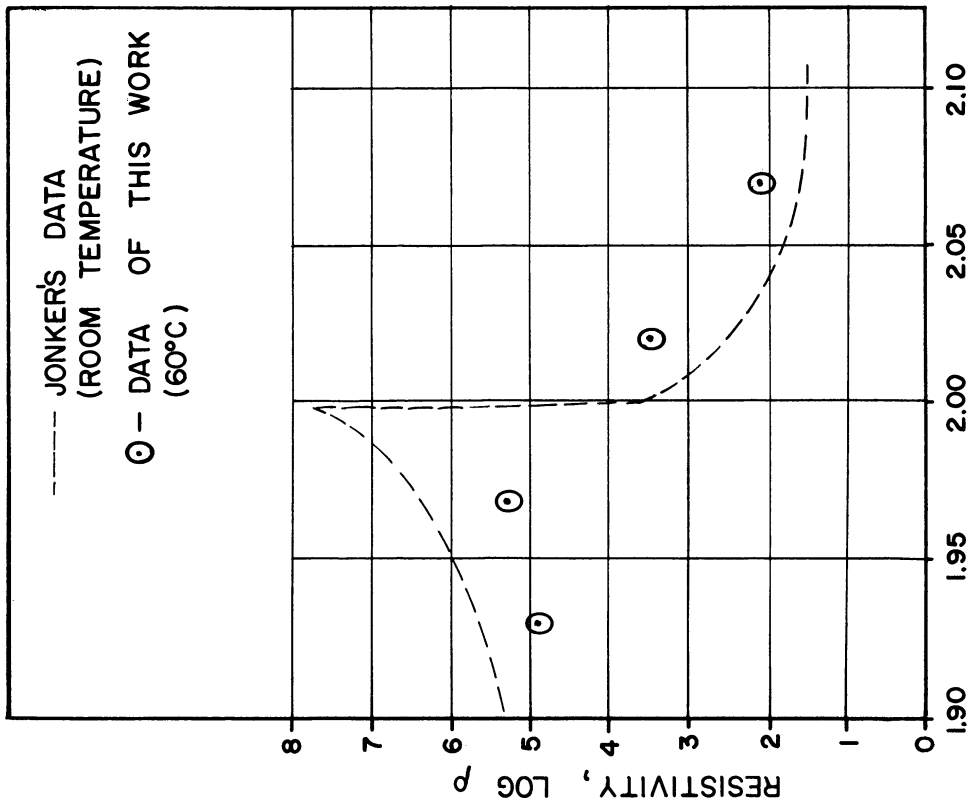

Figure 17. Resistivity of Cobalt Ferrite as a Function of Composition.

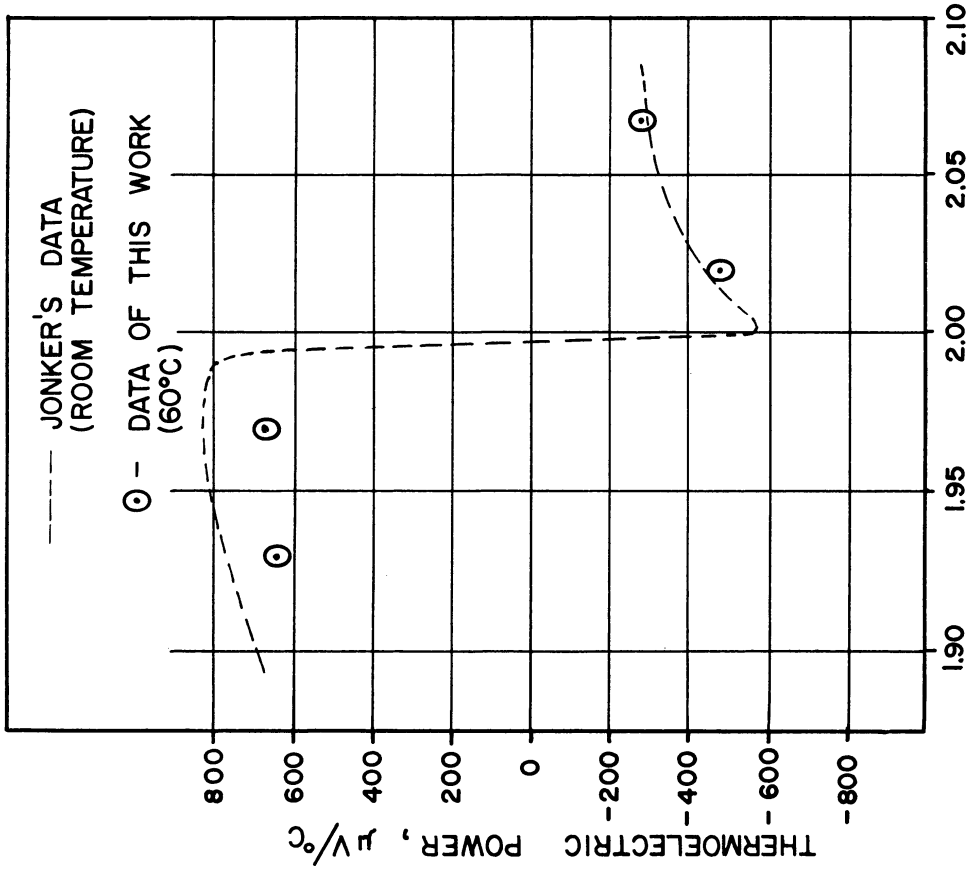

Figure 16. Thermoelectric Power of Cobalt Ferrite as a Function of Composition.

crushed pellets indicated that single phase spinel compounds were formed for all four compositions. These results are in good agreement with reports of the phase behavior of cobalt ferrite by Jonker[45], Smiltens[89], Robin and Benard[78], and Roiter and Paladino[81]. A typical x-ray diffraction pattern is given in Figure 35a, Appendix III. All of the lines, except two, in the x-ray diffraction pattern shown in Figure 35a may be attributed to the diffraction of Co radiation on a spinel structure. The two extra lines are caused by iron contamination in the cobalt target in the x-ray diffraction tube. This error may be checked by applying a correction factor equal to the ratio of the wavelengths of the iron and cobalt radiation. (See footnote, Table XIII, Appendix III.) Sample calculations of "d" values for the x-ray diffraction pattern are given in Table III, Appendix XIII.

The catalyst pellets were crushed and screened. The fraction which would pass through a No. 40 mesh Tyler screen but would not pass through a No. 100 mesh Tyler screen was used as the catalyst for the hydrogen-deuterium exchange studies.

The surface area of this crushed powder, measured in a B. E. T. apparatus, was found to be 0.08 m^2/gm. No variation in surface area, within the experimental accuracy of the B. E. T. measurements, was observed between the different catalyst samples.

Figure 18 is a typical photomicrograph of the crushed catalyst particles. As would be expected due to the screening procedure employed, the particle sizes lie in the range 0.15 to 0.5 mm.

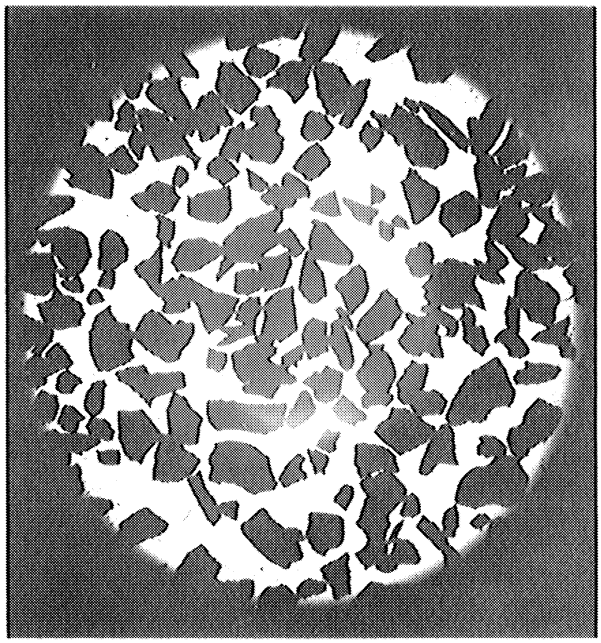

Figure 18. Photomicrograph (11.5x) of the Crushed Pellet Catalyst Particles

The density of the ferrite catalyst, measured in a 10 cc. picnometer, was 5.2 gm/cc.

2. Exchange Runs

Preliminary runs indicated that for given flow rate and temperature, the per cent conversion would remain constant as a function of time (the constant flow was continued for as long as four hours), after the catalyst was activated for 12 hours at 200°C

in a hydrogen atmosphere. It was further found that activated samples would be rapidly deactivated if exposed to air or oxygen.

Preliminary runs were also made to test the variation in per cent conversion with flow rate and temperature. Run 72, shown in Figure 19 , illustrates that consistent values of the per cent conversion were observed as the flow rate was alternated from 20 cc./min. to 37 cc./min. at a constant temperature of 126°C. In Figure 20 , Run 74 indicates that at a constant flow rate (20 cc./min.) the per cent conversion observed at decreasing temperatures was the same as that observed when the temperature was increasing.

A plot of the data from a typical hydrogen-deuterium exchange experiment is shown in Figure 21 . A summary of the activation energies and pre-exponential factors for the hydrogen-deuterium exchange experiments are given in Table IV. The experimental data used in calculating Table IV is given in Tables X and XI , Appendix IA .

In Figures 22 and 23 the activation energy and pre-exponential factor, respectively, are plotted as a function of the $Co_{3-x}Fe_xO_4$ composition variable, x. The activation energy increases 4 to 5 Kcal/mole and the pre-exponential factor increases 6 to 7 orders of magnitude as the composition progresses from $x < 2.0$ to $x > 2.0$. This compensation effect is emphasized in Figure 24 , which is a plot of activation energy vs. $\ln(ko)$.

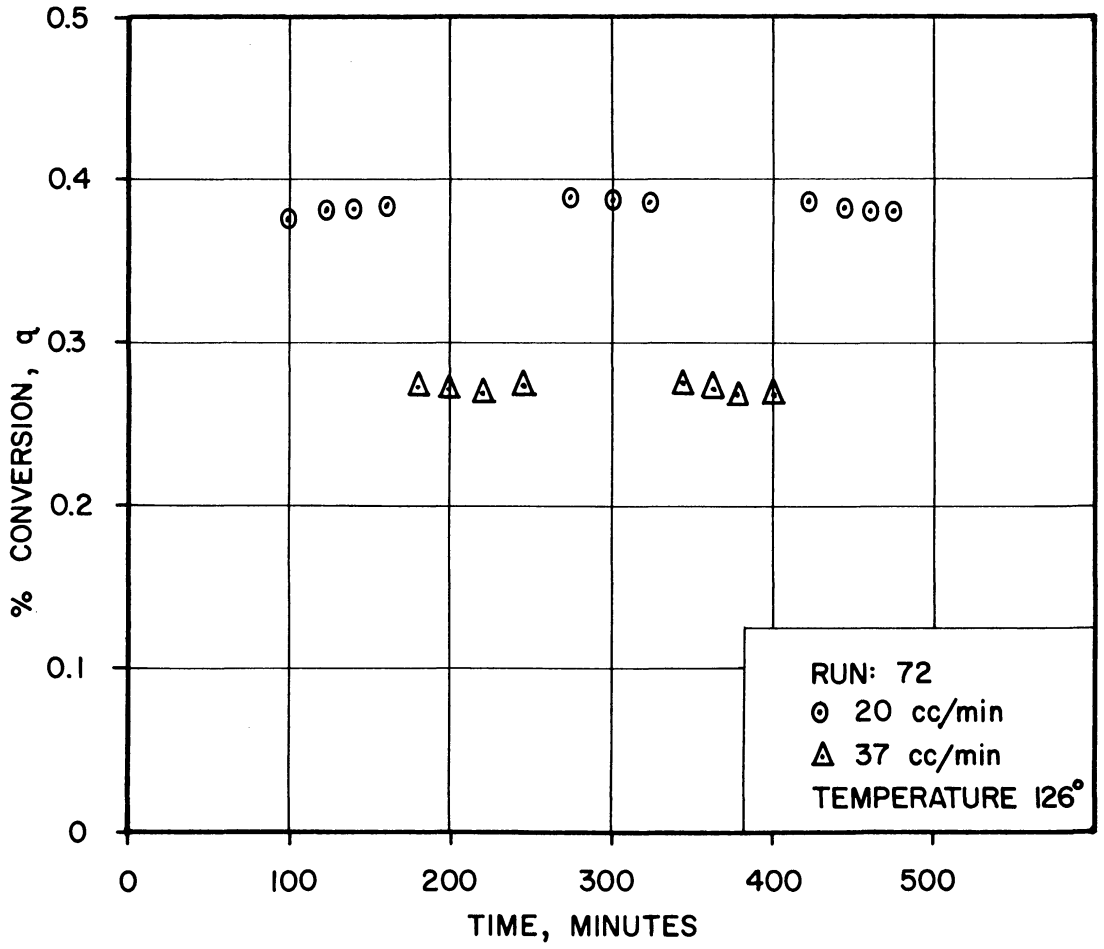

Figure 19. The Effect of Changes in Flow Rate on Percent Conversion at Constant Temperature.

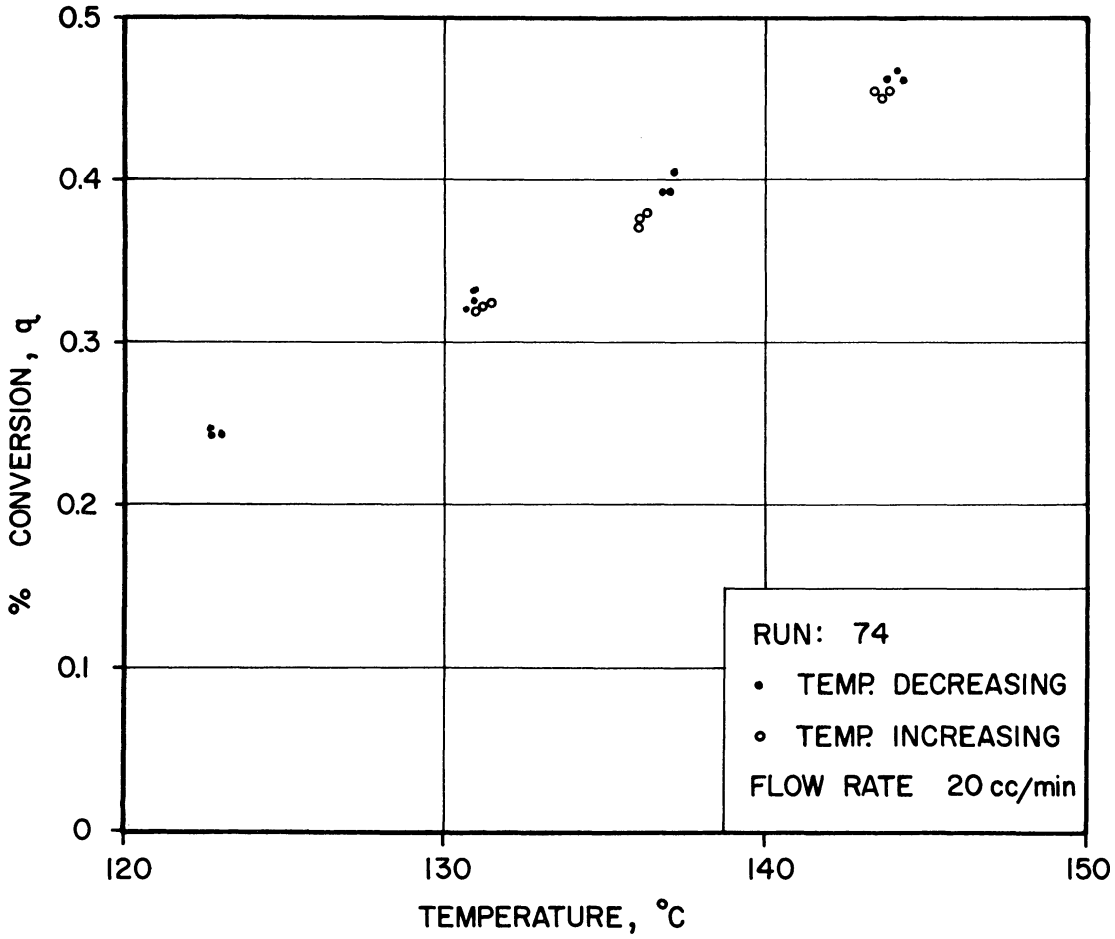

Figure 20. Percent Conversion as a Function of Temperature at Constant Flow Rate.

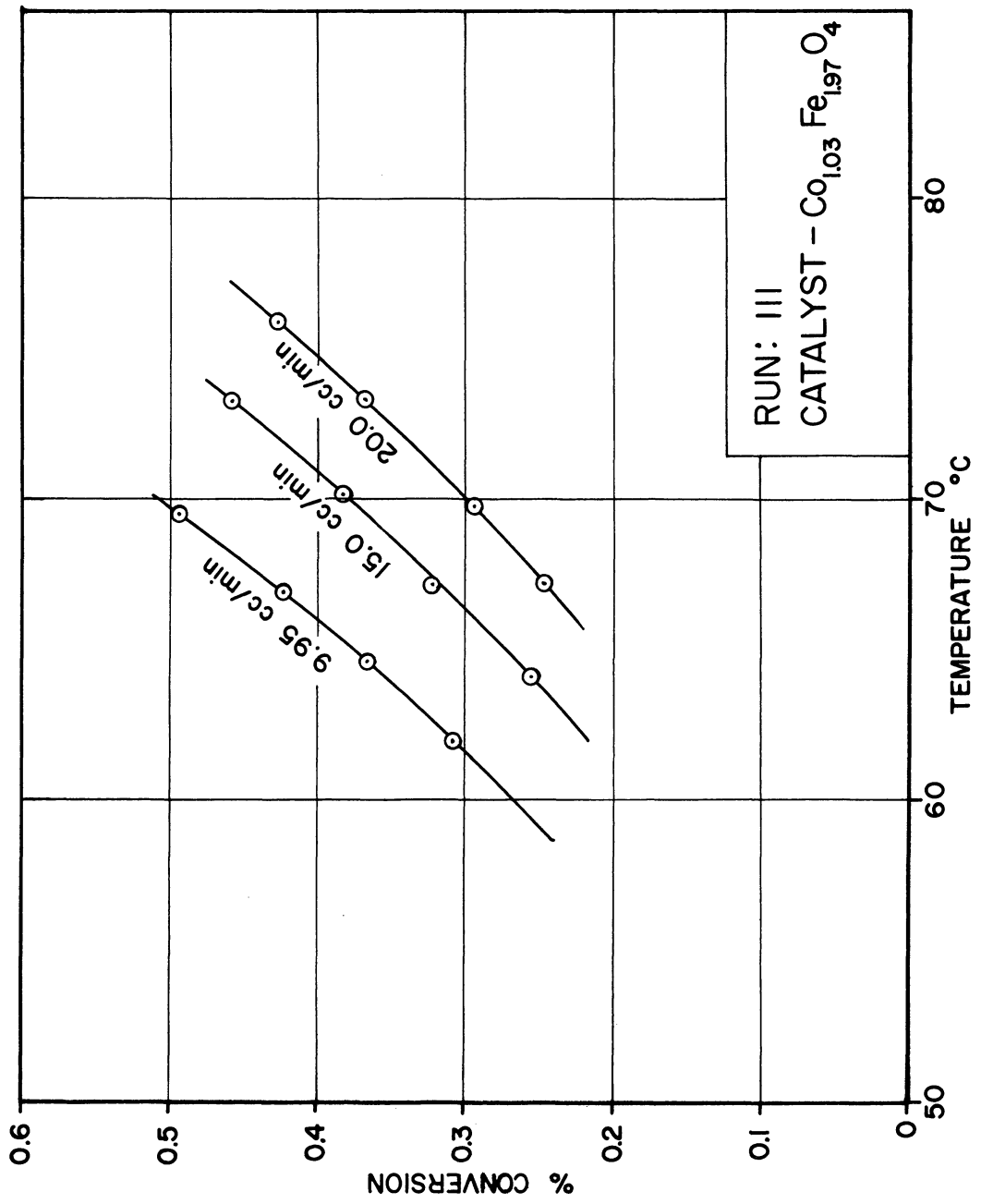

Figure 21. A Typical Hydrogen-Deuterium Exchange Run.

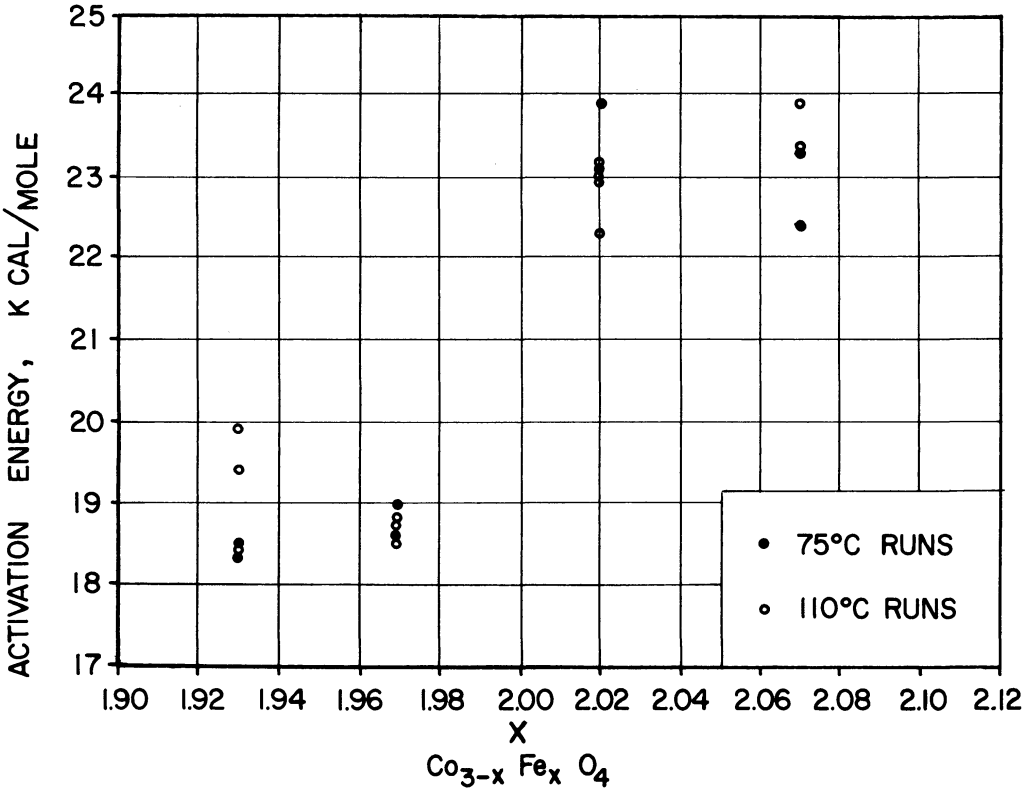

Figure 22. Activation Energy as a Function of Catalyst Composition.

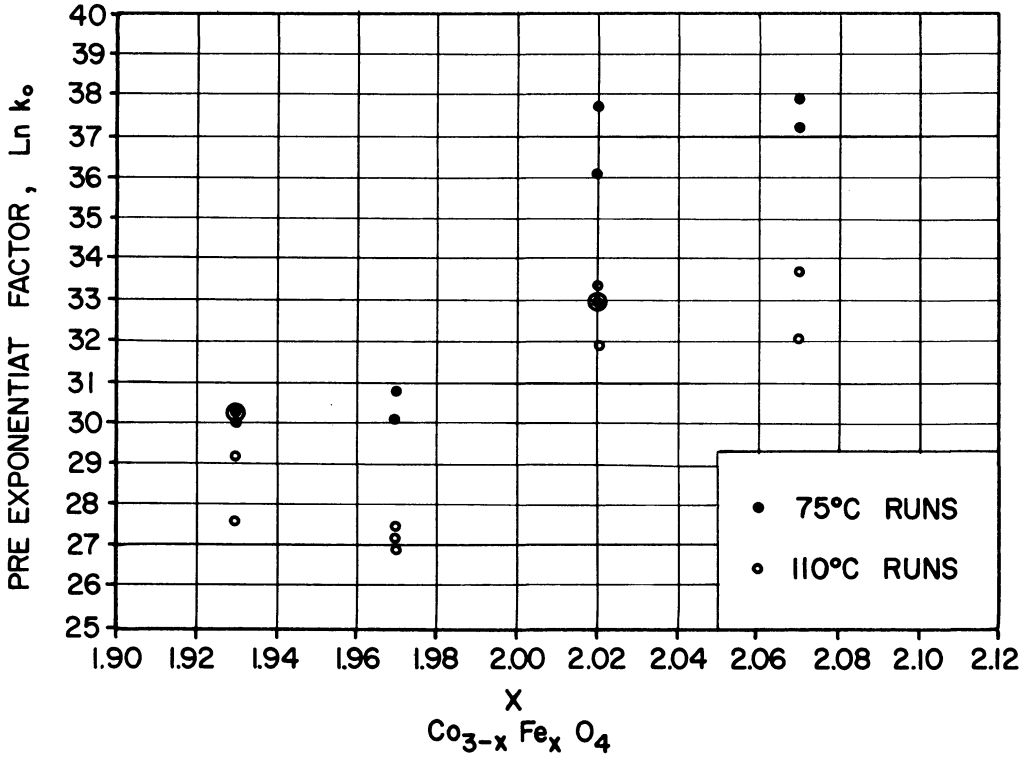

Figure 23. Pre-Exponential Factor as a Function of Catalyst Composition.

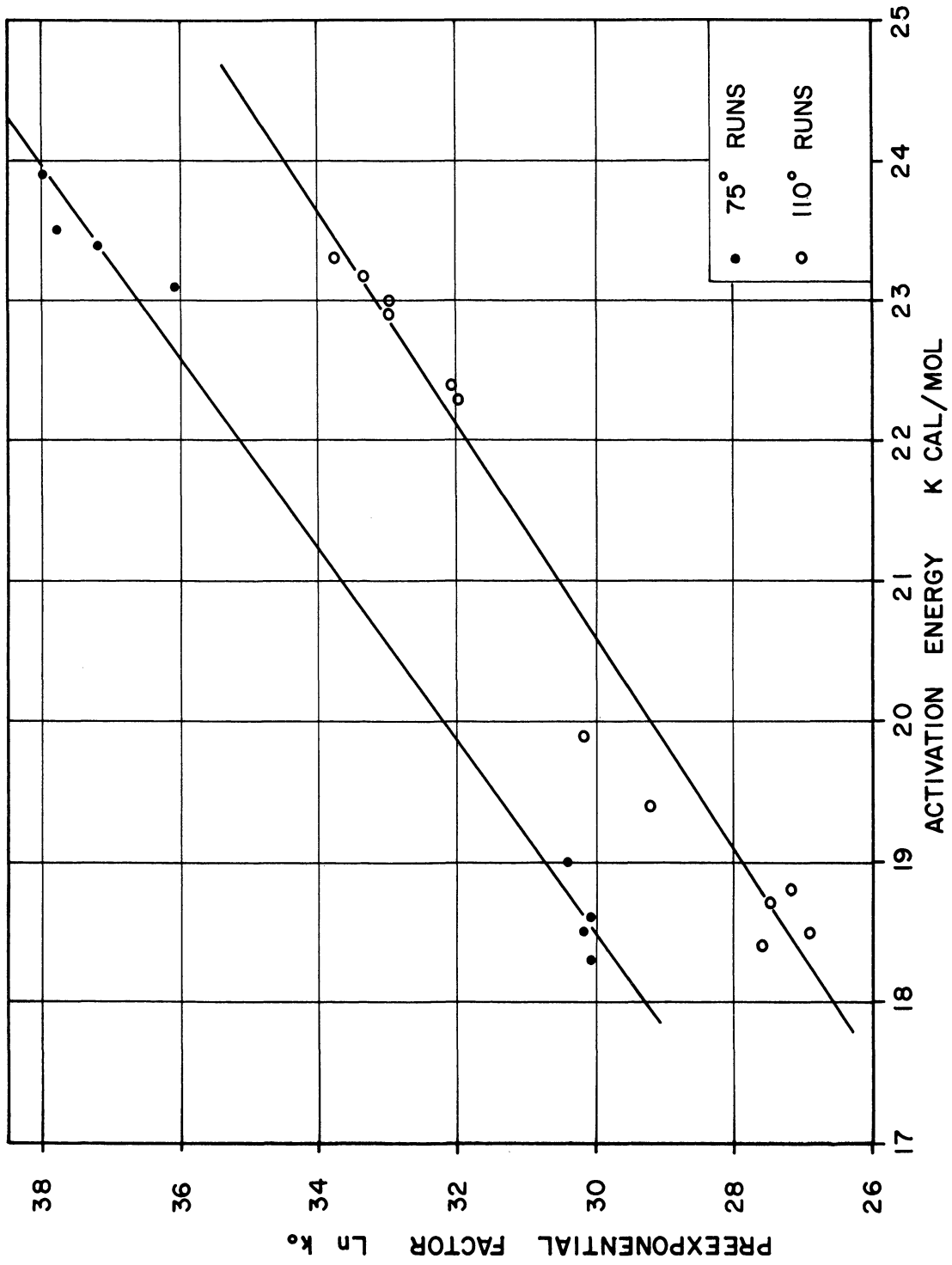

Figure 24. Compensation Effect Between Activation Energy, E, and Preexponential Factor, Ln k_o .

TABLE IV. Summary of Activation Energy and Pre-exponential Factors for Hydrogen-Deuterium Exchange Experiments

		110°C Runs			75°C Runs		
Sample	Type	Run No.	Act. Energy Kcal/mole	Pre-exp. Factor $\ln(k_o)$	Run No.	Act. Energy Kcal/mole	Pre-exp. Factor $\ln(k_o)$
$Co_{1.07}Fe_{1.93}O_4$	p	76	19.4	29.2	108	18.3	30.1
		77	19.9	30.2	110	18.5	30.2
		78	18.4	27.6			
$Co_{1.03}Fe_{1.97}O_4$	p	80	18.7	27.5	111	19.0	30.8
		81	18.5	26.9	112	18.6	30.1
		82	18.8	27.2			
$Co_{0.98}Fe_{2.02}O_4$	n	83	23.2	33.4	120	23.9	37.8
		84	23.0	33.0	121	23.1	36.1
		85	22.9	33.0			
		86	22.3	32.0			
$Co_{0.93}Fe_{2.07}O_4$	n	89	23.3	33.8	123	23.4	37.3

The results of four runs made on mixed, sintered, p- and n-type catalysts are given in Table V. The activation energies and pre-exponential factors calculated for these runs, which were made to see what effect the formation of p-n junctions in the catalyst might have on the exchange kinetics, do not differ appreciably from the results for the unmixed catalyst listed in Table IV.

TABLE V . Activation Energies and Pre-exponential Factors for Runs Using Mixed Sintered Catalysts

Sample	Sintering Time (hr)	Run No.	Act. Energy Kcal/mole	Pre-exp. Factor $\ln(k_o)$
50% $Co_{1.07}Fe_{1.93}O_4$	0	125	20.7	33.5
50% $Co_{0.93}Fe_{2.07}O_4$	1 hour 850°C	126	21.6	34.4
	1 hour 990°C	127	21.1	34.2
	1 hour 1120°C	128	22.1	34.3

B. The Effect of Chemisorption on Thermoelectric Power

1. Cobalt Ferrite Characterization

Cobalt ferrite powder having two different compositions, one with $x < 2.0$ and one with $x > 2.0$, were prepared. The compositions of these samples, determined by means of wet chemical analysis, were $Co_{1.09}Fe_{1.91}O_4$ and $Co_{0.96}Fe_{2.04}O_4$.

X-ray diffraction patterns of the samples indicated that a single phase spinel compound was formed in each case. A typical x-ray diffraction pattern is presented in Figure 35B , Appendix III. All lines in Figure 35B are characteristic of the spinel structure except for the two extra lines caused by the iron contamination in the cobalt target of the x-ray tube (see footnote, Table XIII , Appendix III).

The surface area of the ferrite powder was measured by B. E. T. techniques. Figure 25 shows the surface area of the ferrite powder as a function of the firing time.

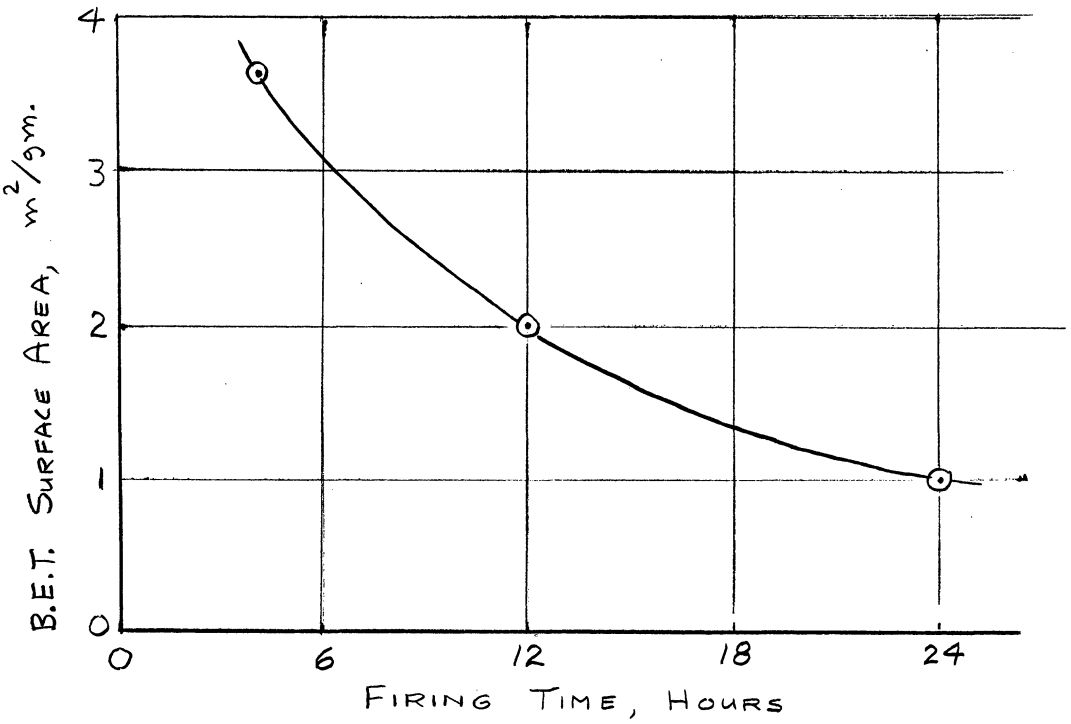

Figure 25. Surface Area of Ferrite Powder as a Function of Firing Time (1035°C for 4 hours followed by 1100°C for 20 hours)

The samples used in the chemisorption studies were fired for four hours at 1035°C followed by eight hours at 1100°C, which corresponds to a surface area of $2m^2/gm$.

Figure 26 is a photomicrograph of the resulting sintered agglomerates of small particles. These agglomerates were separated by means of a mortar and pestle in accordance with the techniques outlined by Schuster and Fullam[84]. Figures 27 and 28 are electron micrographs of the resulting separated particles. From eight

electron micrographs at 11000x magnification, including the micrograph in Figure 27 , the particle size distribution of the ferrite was obtained. This particle size distribution results in a normal distribution when plotted on a logarithmic scale (see Figure 29) but gives a skewed curve when plotted on a linear scale. This "skewed" distribution, found in previous work[74][26], is probably due to sintering of the ferrite powder.

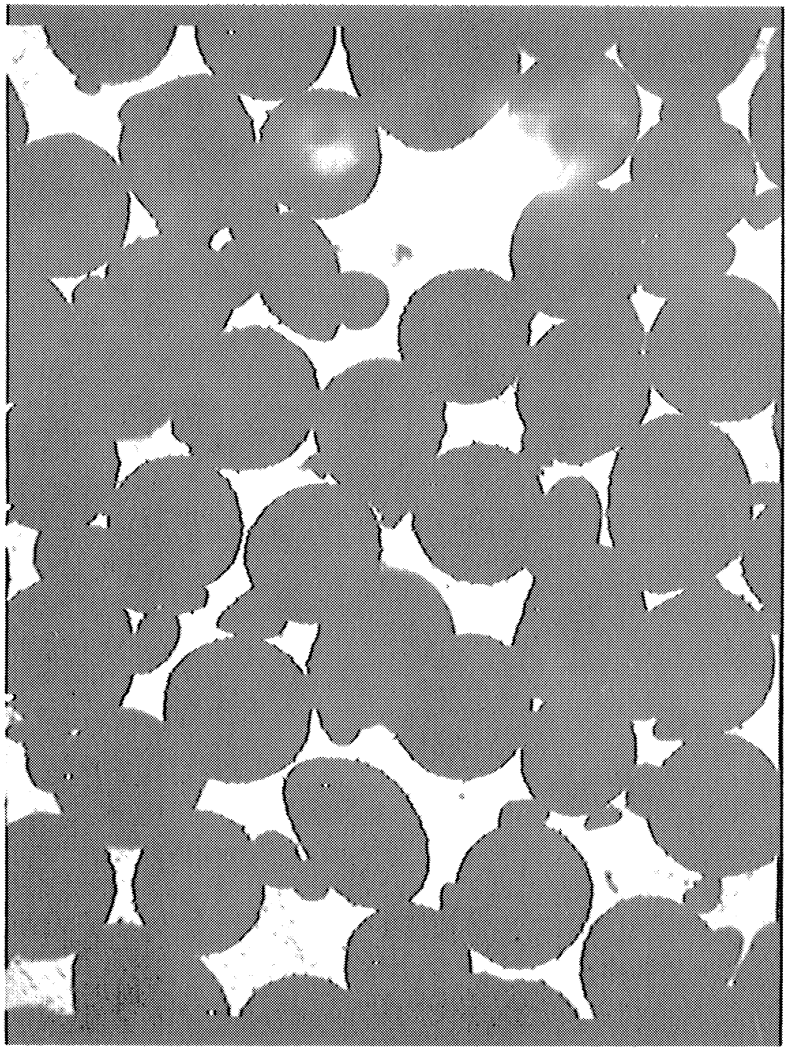

Figure 26. Photomicrograph (60x) of Sintered Ferrite Powder Agglomerates

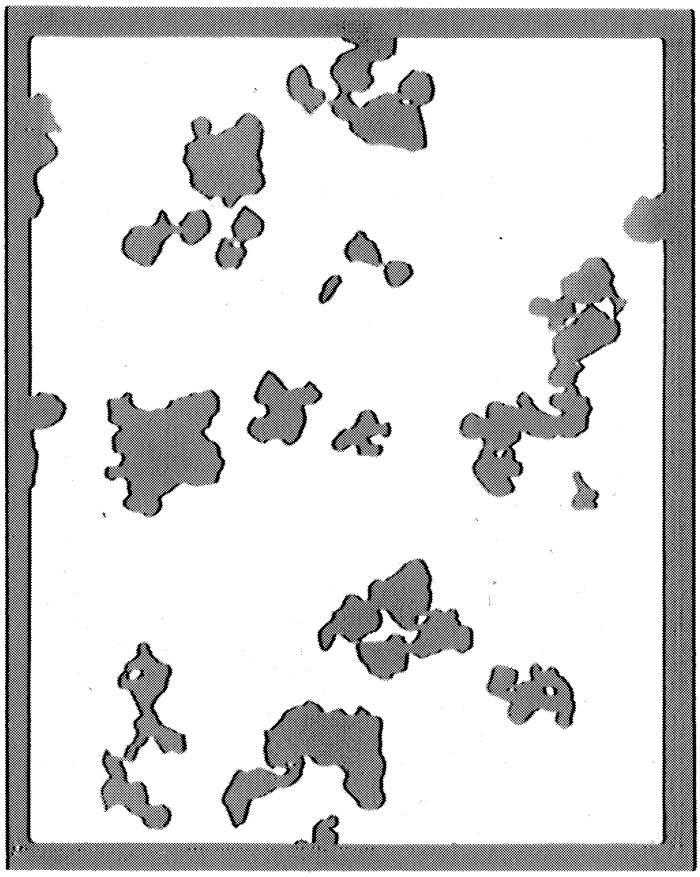

Figure 27. Electron Photomicrograph (11000x) of Separated Particles

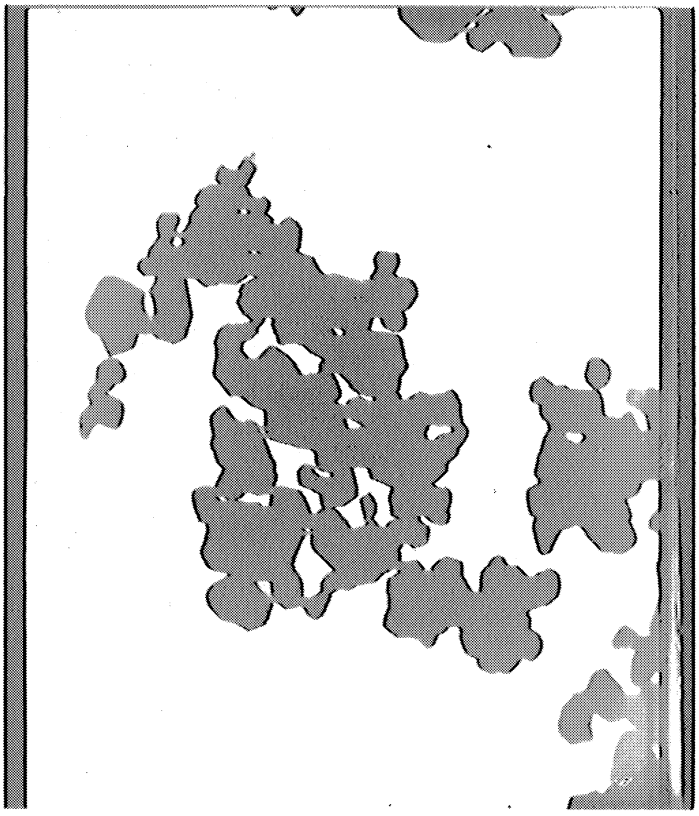

Figure 28. Electron Photomicrograph (16000x) of Separated Ferrite Particles

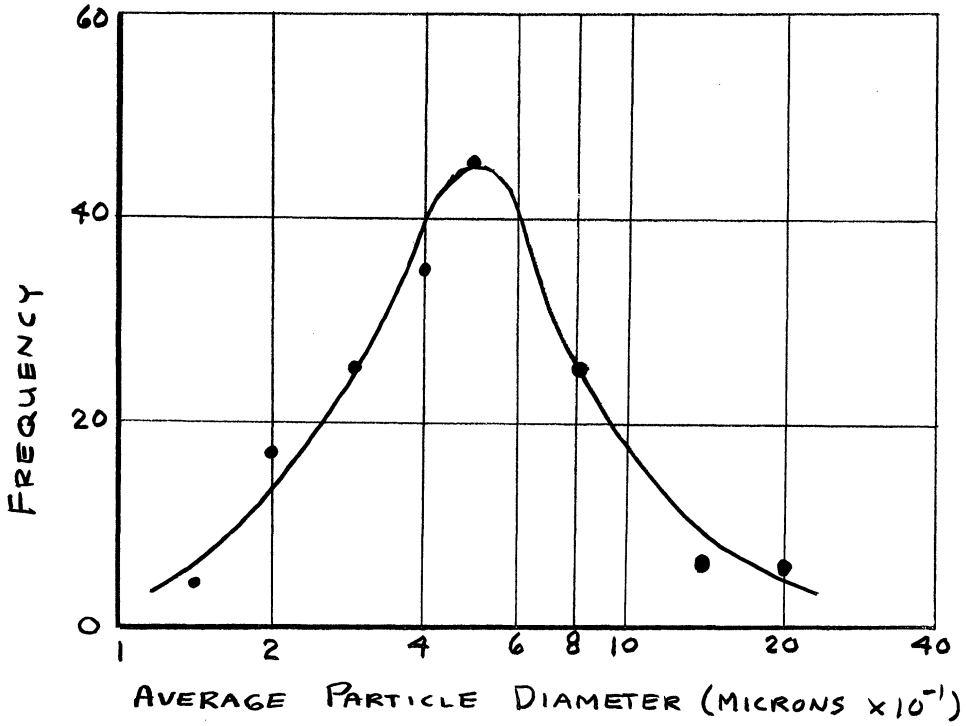

Figure 29. Particle Size Distribution For Separated Ferrite Particles

The density of the ferrite powder, measured by means of a 10 cc. picnometer, was 5.3 gm/cc. If a spherical particle shape is assumed, the average particle size can be estimated by

$$d = \frac{6}{A\rho} = 0.56 \text{ microns}$$

where A is the surface area and ρ the solid density. This value agrees quite well with the value determined electronmicroscopically.

2. Thermoelectric Power Measurements During Chemisorption of Hydrogen and Oxygen Gases

Preliminary runs were made to test the variation of emf with ΔT and the emf at zero ΔT under varying gas atmospheres.

Figure 30 , in which the emf is plotted for $Co_{0.93}Fe_{2.07}O_4$ for eight different ΔT's, illustrates that no variation in thermoelectric power was observed for different ΔT values. Table VI illustrates that the emf's produced by temperature differences near $\Delta T \approx 0$ is constantly small in helium, hydrogen, and oxygen atmospheres. The ΔT values in this table, given in millivolts (Chromel-Alumel couples) are all less than 0.02°C (i.e., .01°C = .0004 millivolts). This table indicates that the intercept of the emf vs. ΔT curve, the slope of which determines the thermoelectric power, does not appreciably vary in helium, hydrogen, or oxygen atmospheres.

TABLE VI. Variation of EMF at $\Delta T \cong 0$ for Different Gas Atmospheres

Sample	Helium Atmos. ΔT	Helium Atmos. emf	Hydrogen Atmos. ΔT	Hydrogen Atmos. emf	Oxygen Atmos. ΔT	Oxygen Atmos. emf
$Co_{1.09}Fe_{1.91}O_4$	0.0003	0.0021	0.0000	0.0310	0.0007	0.0112
$Co_{0.96}Fe_{2.04}O_4$	0.0001	0.0302	0.0005	0.0092	0.0003	0.0412

Typical plots showing the change in thermoelectric power during gas adsorption are given in Figure 30 (high temperature = 250°C), Figure 32 (intermediate temperature = 150°C), and Figure 33 (low temperature = 88°C). A summary of the results of all of the thermoelectric power runs is given in Table VII . Raw data for these runs are presented in Tables XII, Appendix IB.

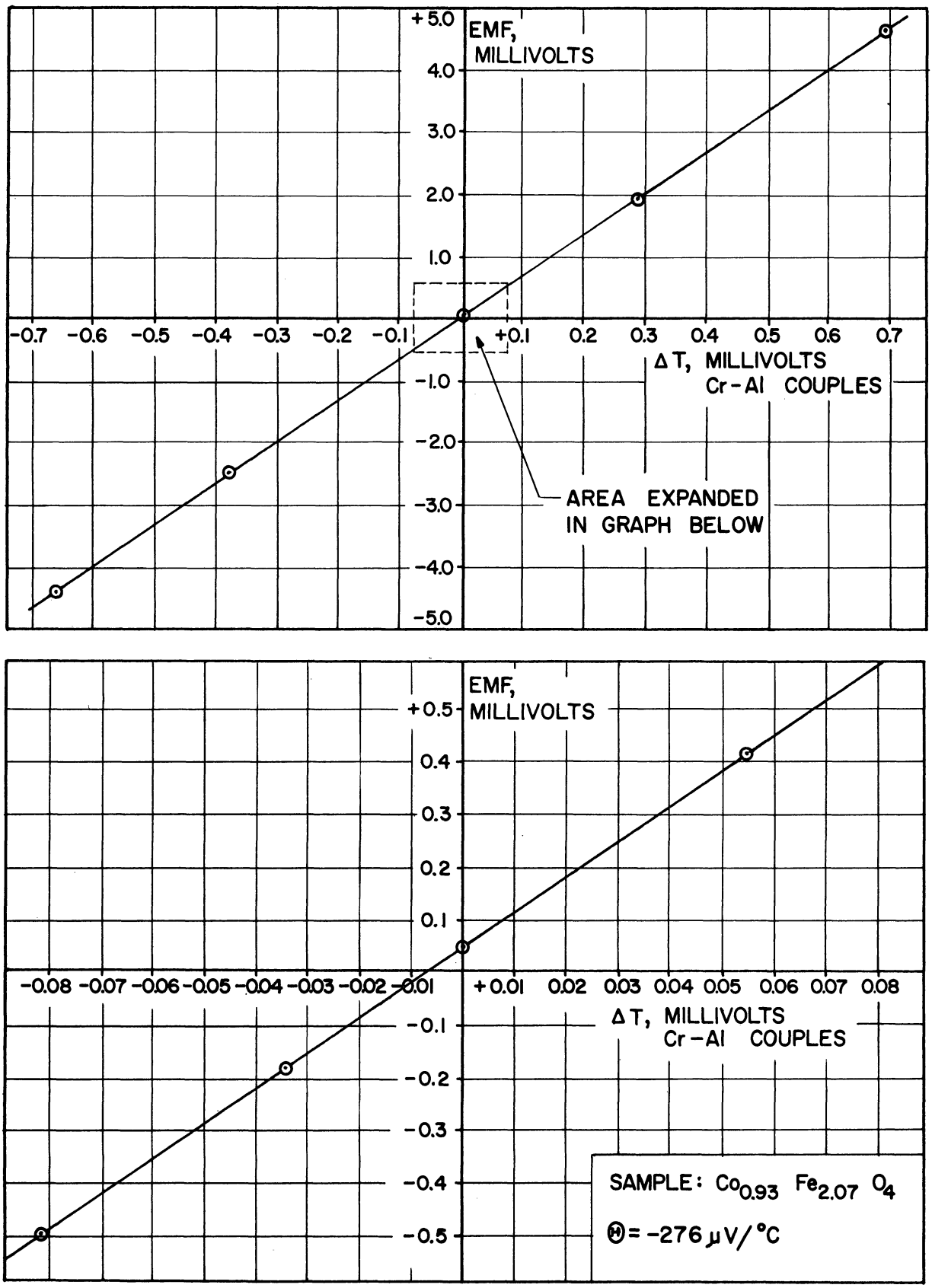

Figure 30. Variation of EMF of Ferrite Pellet with ΔT Across the Pellet.

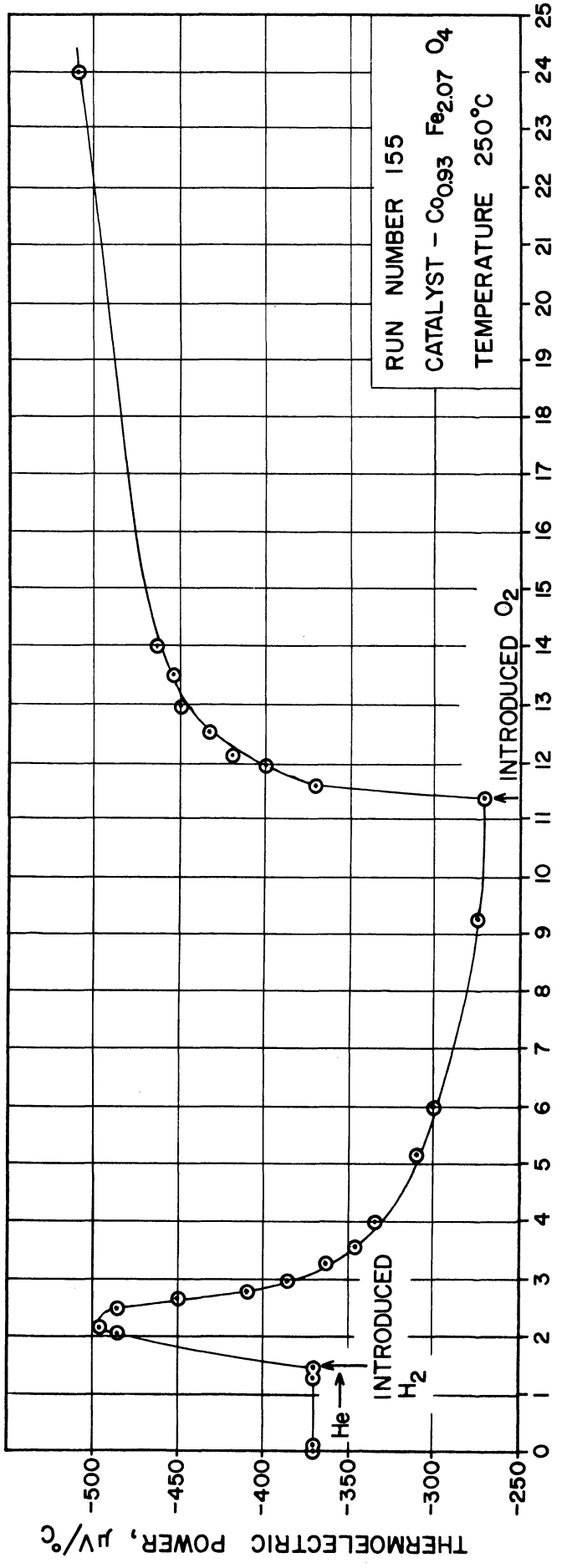

Figure 31. Variation of Thermoelectric Power with Time in Helium, Hydrogen, and Oxygen Atmospheres; Temperature = 250°C.

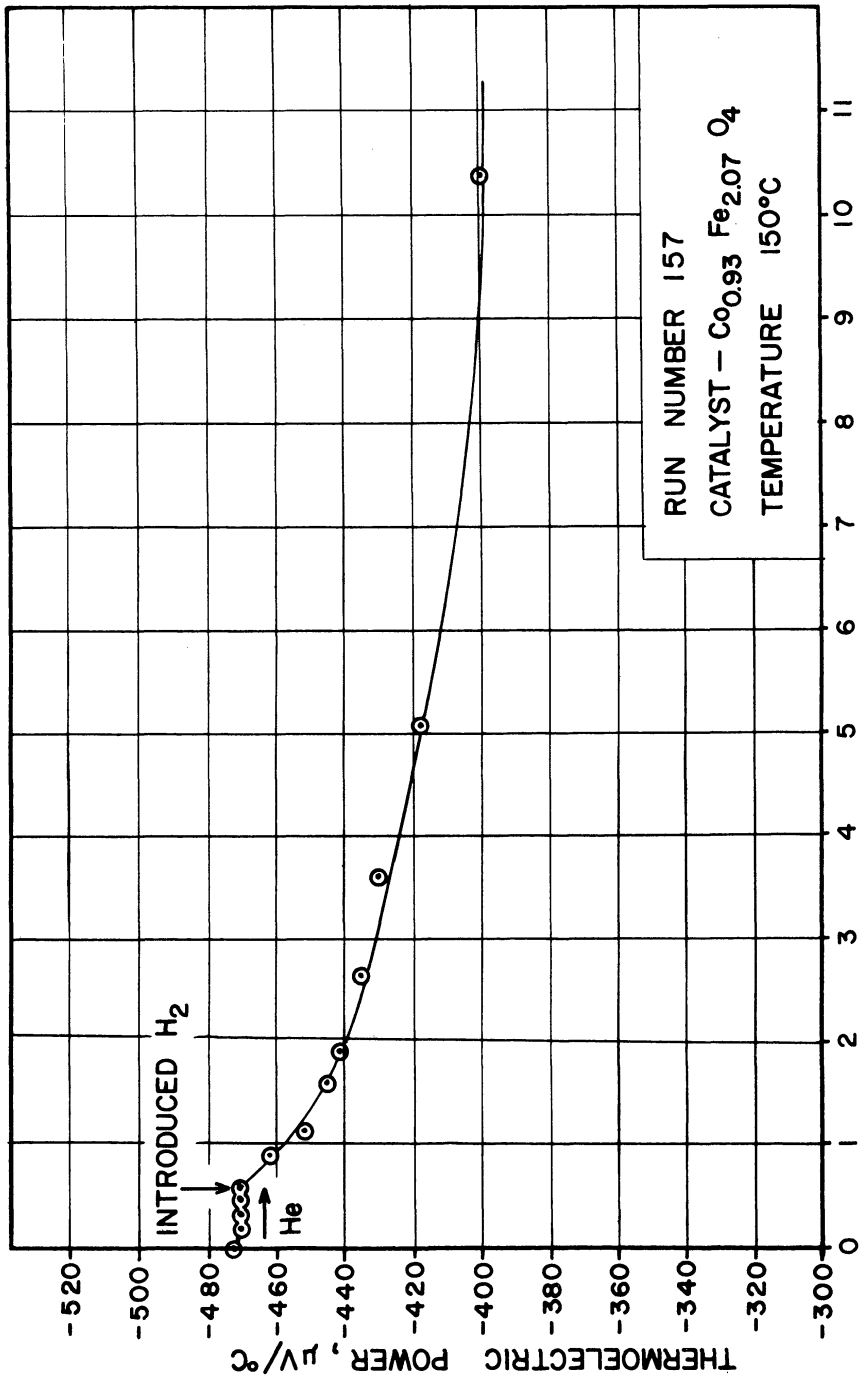

Figure 32. Variation of Thermoelectric Power with Time in Helium and Hydrogen Atmospheres; Temperature = 150°C.

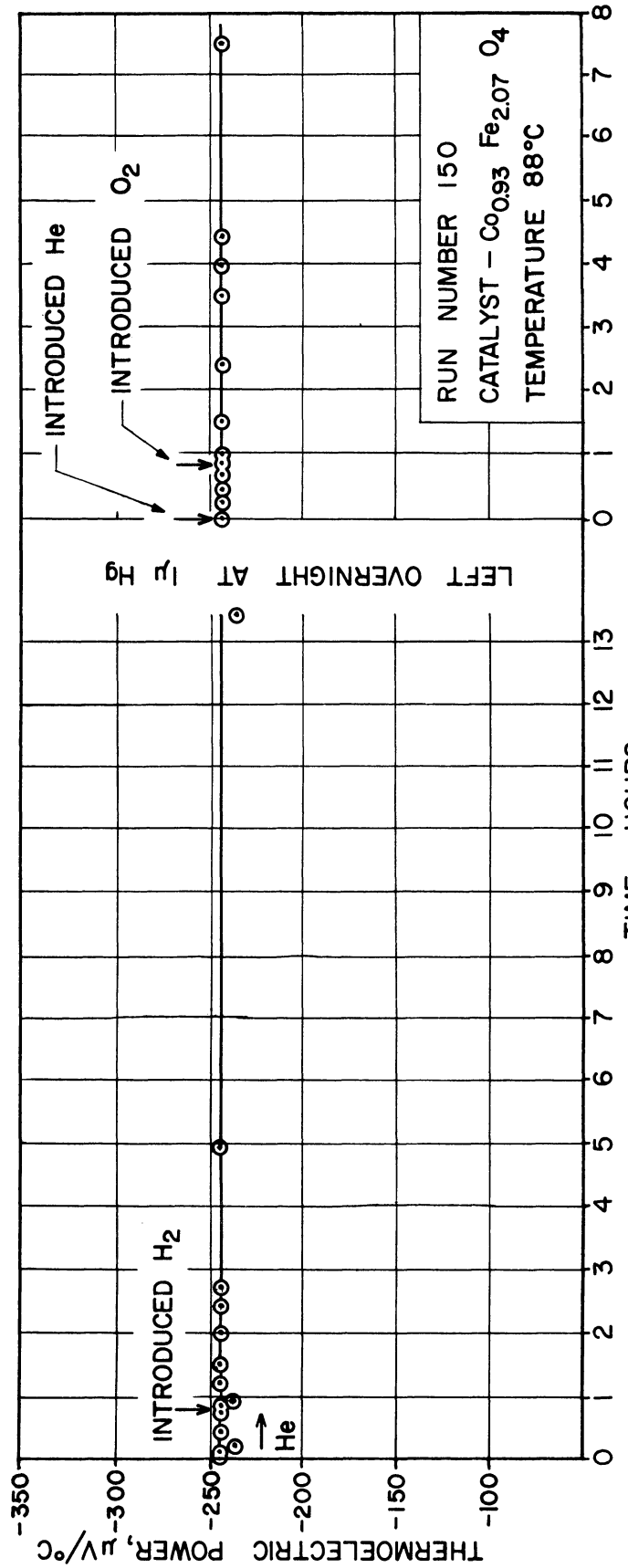

Figure 33. Variation of Thermoelectric Power with Time in Helium, Hydrogen, and Oxygen Atmospheres; Temperature = 88°C.

TABLE VII. Thermoelectric Power Change During the Adsorption of Hydrogen and Oxygen

Run No.	Catalyst Semiconductivity Type	Gas Adsorbed		Temperature °C
		Oxygen*	Hydrogen*	
112	p	(1) ↑		250°
113	p		(1) ↓	250
114	n	(2) ↓	(1) ↑	250
119	n	(2) ↓	(1) ↑	250
120	p	(2) ↑	(1) ↓	250
126	p	(1) ↑	(2) ↓	250
138	n	(2) ↑	(1) ↷	250
139	n		(1) ↷	250
141	p	(1) ↑	(2) ↓	250
142	n	(2) ↑	(1) ↷	250
143	p	(2) ↑	(1) ↓	250
147	p	(2) ↑	(1) ↓	250
149	p	(2) ↷	(1) →	140
150	n	(2) →	(1) →	88
152	p	(1) ↑	(2) ↓	250
153	p	(1) ↑	(2) ↓	250
155	n	(2) ↑	(1) ↷	250
155a	n	**(1) ↷ +	**(2) ↷ *	250
157	n		(1) ↓	160
158	n		(1) →	88
158a	n		(1) →	120
159	n		(1) ↓	180

* The arrows show the direction of change of the absolute value of thermoelectric power upon admittance of the gas. The numbers (1), (2), refer to the order which the gases were admitted., i.e., compare Runs No. 155 , 157 , 150, and 155a with Figures 31 , 32 , 33 , and 34.

** In Run 155a the thermoelectric power changes from - to + as oxygen was first introduced and from + to - when hydrogen was introduced. The + and - signs on the arrows indicate this change.

V. DISCUSSION OF RESULTS

A. Catalyst

The methods outlined by Jonker[45] were used in preparing the cobalt ferrite catalyst. A hard, sintered, non-porous ferrite pellet resulted. Crushed ferrite pellets having four different compositions were used as catalysts for the hydrogen-deuterium exchange studies.

If the hydrogen-deuterium exchange reaction occurs by means of an adsorption-desorption mechanism on the cobalt catalyst, the investigation of the electron transfer process by means of thermoelectric power measurements during the chemisorption of hydrogen and oxygen would be valuable in gaining an insight into the mechanism of the reaction.

However, no change was observed in the thermoelectric power of these sintered ferrite catalyst pellets during the adsorption of helium, hydrogen, or oxygen. This result would be expected if, as discussed in Chapter II, the ratio of the surface layer to particle diameter was so small that the contribution of the surface layer to the thermoelectric power, which would be influenced by the chemisorbed gas, was negligible. In this case, the measured thermoelectric power would be characteristic of the bulk thermoelectric power of the pellet and would be independent of the degree of adsorption on the surface.

In order that the surface contribution to the thermoelectric power would be an appreciable part of the total measured thermoelectric

power, a ferrite pellet with a much larger surface to volume ratio was required. To achieve this end, the technique used by Parravano and Domenicali[74] in studying the thermoelectric behavior of solid particulate nickel oxide was applied to the ferrite. In this technique high surface area powder is compressed to form mechanically strong pellets without the need for additional heating. In order to make the high surface area powder needed for this technique, a ferrite preparation procedure was used in which final firing of the ferrite material occurred at a lower temperature (1100°C as compared to 1350°C) and in a powder form (as compared to a compressed pellet form). The observed variation of thermoelectric power under different gas atmospheres for the mechanically compressed pellets made from the powdered ferrite indicates that the surface contribution to the thermoelectric power is appreciable. The thermoelectric power measurements made on these powdered samples shows the same trend (i.e., swing from + to - at $x = 2.0$) with composition as was observed for the sintered pellets. However, due to the contribution of the surface layer, the magnitude of the thermoelectric power of the powdered samples would not be expected to agree with the value reported by Jonker[45], which correspond to the bulk thermoelectric power of the ferrite. By observing the direction of the change in thermoelectric power of the compressed powder pellets, an insight can be gained into the electron transfer mechanism during adsorption and desorption. This insight may then be applied to better understand the reaction mechanism of the heterogeneous catalysis of hydrogen-deuterium on the cobalt surface.

If the results of the thermoelectric power studies made on this higher surface area ferrite are going to apply to the kinetic study results made on the pelletized ferrite, it must be demonstrated that the two preparation techniques result in the same ferrite material, with different surface areas. This assumption is supported by Figure 35, Appendix III, in which the x-ray diffraction patterns and true solid densities of the two materials are compared. The x-ray diffraction patterns agree both in the line position and relative intensity, indicating that the two methods of preparation result in the same single phase spinel structure. The true solid density compares well also.

A surface area of 2 m^2/gm. (Figure 25) and average particle size of .5 microns (Figure 29) resulted from the preparation of cobalt ferrite in the powder form. This particle size is small enough that the space charge layer formed by the transfer of electrons between the adsorbed ions and the catalyst is of the same order of magnitude as the particle size. Parravano and Domenicali[74] reported changes in the thermoelectric power during the adsorption of various gases on nickel oxide, a localized level semiconductor, which was prepared in a manner similar to the ferrite and had approximately the same particle size (i.e., fired at 1100°C in air), with an average particle size of .57 microns. They reported a lower limit of 600Å for the thickness of the space charge region. Due to the similarity in type of material (localized level semiconductor), firing temperature, and particle size, this value, 600Å, is probably a good estimate of the space charge layer thickness at the surface of the cobalt ferrite.

B. Thermoelectric Power Changes During Chemisorption

The measured thermoelectric power, as pointed out in Chapter II, is a function of the hole and electron carrier concentration. Consequently, factors such as catalyst composition, temperature, and chemisorbed ions which change the carrier concentration will also alter the thermoelectric power. The temperature and catalyst composition, however, were held constant during each run, so that the observed change in thermoelectric power may be attributed to changes in carrier concentration caused by the electron exchange between the adsorbed ions and the catalyst surface.

The change in thermoelectric power during chemisorption was observed over the temperature ranges 80° - 250°C. The results of these runs fall into three categories which will be designated as high temperature (approximately 250°C), intermediate temperature (140° - 180°C), and low temperature (80° - 100°C).

1. High Temperature Runs

At high temperatures, the acceptor levels and donor levels, which are at most .06 ev above the valence band or below the conduction band respectively, have become ionized, and some electrons are thermally excited across the .55 ev gap from the valence band, into the conduction band. When this occurs, the ferrite becomes a two carrier semiconductor, with the electrons in the conduction band contributing to the n-type conductivity and the holes in the valence band contributing to the p-type conductivity. In this temperature range the thermoelectric power, $\ominus$, is given by

$$\ominus T = \frac{-n_1 \mu_1 [E_g - E_f + \alpha] + n_2 \mu_2 [E_f + \beta]}{n_1 \mu_1 e + n_2 \mu_2 e} \qquad (11)$$

where the Fermi level, E_g and $(E_g - E_f)$ are logarithmic functions of carrier concentration. Equation (11) shows that when $n_1 \cong n_2$ the thermoelectric power will be directly proportional to the carrier concentration. If $n_1 >> n_2$ (or $n_2 << n_1$) however, Equation (11) reduces to

$$e\Theta T = -\alpha - kT \ln \frac{N}{n_1} \qquad (n_1 >> n_2) \qquad (14)$$

$$e\Theta T = +\beta + kT \ln \frac{N}{n_2} \qquad (n_2 >> n_1) \qquad (15)$$

and Θ becomes inversely proportional to the logarithm of n_1 or n_2. Jonker[45] reports the cobalt ferrite becomes a two carrier semiconductor at temperatures above approximately 160°C. Experimental evidence of two carrier ferrite at high temperatures (250°C) was also observed in this work (see next paragraph). For compositions in the neighborhood of $CoFe_2O_4$, this intrinsic dissociation occurs at lower temperatures[45].

At 250°C, hydrogen ions, adsorbed on a two carrier n-type ferrite, would give up electrons to the catalyst surface, thereby increasing the absolute value of the n-type thermoelectric power as predicted by Equation (11). When the electron concentration increased to the point where $n_1 >> n_2$, Equation (11) reduces to Equation (14) and the magnitude of n-type thermoelectric power should begin to decrease. If oxygen is now admitted to the surface, electrons will be transferred to the adsorbed oxygen atoms, increasing the absolute value of the thermoelectric power. This effect, is clearly demonstrated in Runs No.

138, 139, 142, 155 and 155a. See Table VII and Figure 34. Run 155a, Figure 34, is particularly interesting. In this run, oxygen was adsorbed at 250°C on an n-type ferrite. As electrons were transferred, n_1 became smaller than n_2 and the thermoelectric power switched from n-type to p-type, changing from an initial value of -170 μv/°C to a value of +600 μ v/°C where it began to level off as $n_2 >> n_1$. At this point hydrogen was introduced and the transfer of electrons from the hydrogen to the surface (and probably the reduction of the adsorbed oxygen to water) caused the thermoelectric power to swing from +600 μ v/°C to a value of -420 μ v/°C. At this point $n_1 >> n_2$ and, as predicted by Equation (14), the absolute value of thermoelectric power began to decrease as n_1 increased further. The amounts of hydrogen and oxygen needed for a transition from the two carrier case, Equation (11), to the single carrier case, Equation (15) may be estimated by using the data given by Jonker, Table I. This data predicts, at room temperature for instance, at a maximum thermoelectric power, 2% of the acceptor levels are ionized and a minimum thermoelectric power at 0%. (This minimum is 0% excess Fe, rather than some larger value, due to the large mobility ratio, $\mu_1 / \mu_2 = 10^4$). If the acceptor levels are furnished by the adsorbed gas, and if the surface contribution to the thermoelectric power controls the measured value, a 2% coverage would be necessary to swing the thermoelectric power from the negative minimum to the positive maximum (see Figure 34). The magnitude of this calculated per cent coverage is certainly reasonable.

These runs demonstrate that at 250°C the ferrite behaves as a two carrier semiconductor, with hydrogen being adsorbed as an electron

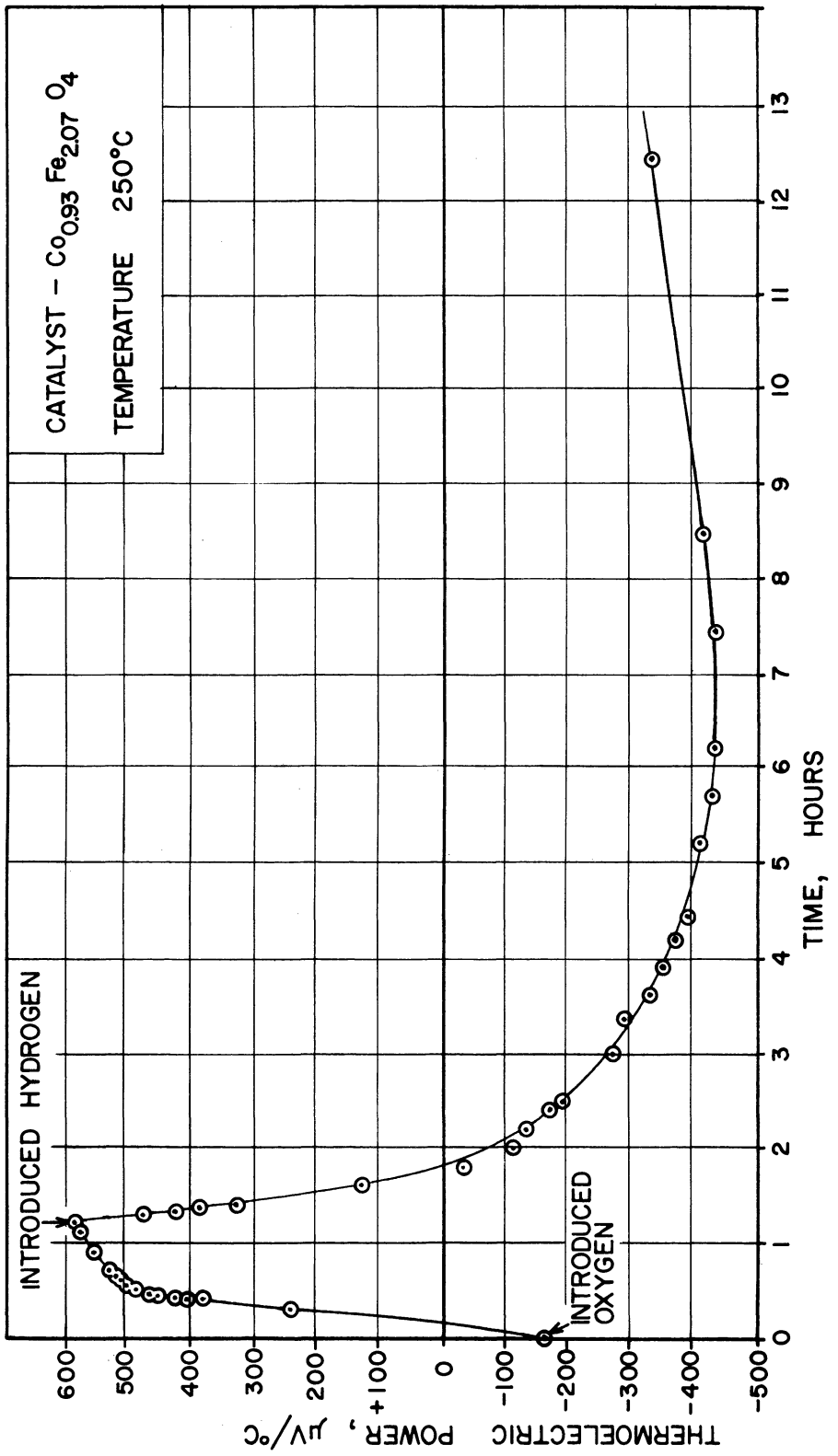

Figure 34. Run Number 155a; Variation of Thermoelectric Power with Time in Oxygen and Hydrogen Atmospheres.

donor and oxygen being absorbed as an electron acceptor.

2. Intermediate Temperature Runs

In the intermediate temperature range, the acceptor levels (or donor levels) are thermally ionized, but the intrinsic conduction is negligible. Therefore, either n_1 or n_2 predominates and Equations (14) and (15) apply, with the absolute value of the thermoelectric power being inversely proportional to the logarithm of the concentration of the majority carriers. In this case the absolute value of the thermoelectric power of an n-type ferrite should be decreased by hydrogen adsorption and increased by oxygen adsorption. In a similar manner the magnitude of the thermoelectric power of a p-type ferrite should be increased by oxygen adsorption and be decreased by hydrogen adsorption. Runs No. 157 and 159 (TABLE VII) demonstrate this effect.

3. Low Temperature Runs

At still lower temperatures (80°-120°C) the ferrite is a single carrier semiconductor with completely ionized donor and acceptor levels. Therefore, the effect of the transfer of electrons from the adsorbed hydrogen or oxygen would be expected to be the same as the effect observed in the intermediate temperature range. However, in this low temperature range, which corresponds to the temperature of the kinetic exchange experiments, no change in thermoelectric power was observed during the adsorption of hydrogen and oxygen. In this temperature range, the adsorption on the powdered ferrite, therefore, takes place with little electron exchange between the adsorbed molecules and the catalyst surface.

C. Kinetic Studies

The present data show that the hydrogen-deuterium exchange on cobalt ferrite proceeds in two stages: (a) an activation stage, in which the catalyst's activity increases with time, followed by (b) a second stage, in which, the catalyst activity is constant. During the activation stage the 98% hydrogen, 2% deuterium gas mixture flows over the catalyst for twelve hours at 200°C. The activated catalyst could be de-activated by exposing it to air or oxygen.

The data also indicate that the activation energy of the hydrogen-deuterium exchange reaction on cobalt ferrite, ($Co_{3-x}Fe_xO_4$), is a function of the catalyst composition (see Figure 22). For the p-type catalysts, with $x < 2.0$, the activation energy was 18 to 19 Kcal/mole, while for the n-type catalysts, with $x > 2$, the activation energies increased to 23 to 24 Kcal/mole. A similar change was observed in the $\ln k_o$ factor, which increased from 30 to 31 (for $x < 2.0$) to 36 to 38 (for $x > 2.0$). Thus a compensation effect was observed between the activation energy E, and the $\ln k_o$ (see Figure 24).

D. Proposed Reaction Mechanism

The exchange reaction occurs on cobalt ferrite in two stages: (a) an activation stage in which the catalytic activity increases with time and (b) a second stage in which the exchange reaction occurs with constant catalytic activity. The proposed mechanism for the hydrogen pretreatment during the activation stage is given by the following reactions:

$$S(O^-) + \tfrac{1}{2}H_2 \rightarrow S(OH^-) \qquad (62a)$$

$$S(O^-) + \tfrac{1}{2}D_2 \rightarrow S(OD^-) \qquad (62b)$$

$$S(O^{--}) + \tfrac{1}{2}H_2 \rightarrow S(OH^-) + e^- \qquad (63a)$$

$$S(O^{--}) + \tfrac{1}{2}D_2 \rightarrow S(OD^-) + e^- \qquad (63b)$$

$$2S(OH^-) \rightarrow H_2O + S(O^-) + e^- \qquad (64)$$

where S refers to a surface site.

In this proposed mechanism the hydrogen pretreatment corresponds to the reduction of adsorbed oxygen. The oxygen is present on the surface of the ferrite as O^- and O^{--}. The reaction of hydrogen with O^- (reaction 62a) will be referred to as Type A adsorption, reaction with O^{--} (reaction 63), will be called Type B adsorption. Morrison[68] has proposed this scheme to describe the adsorption of hydrogen on ZnO. He points out that the singly ionized oxygen atom should provide an attractive adsorption site for hydrogen since the heat involved for the reaction

$$\tfrac{1}{2}H_2 + O^- \rightarrow OH^-$$

is approximately 2.6 ev, calculated from known heats of reaction for various similar reactions. Morrison also reports, that for ZnO, the activation energy is greater for Type B adsorption than for Type A adsorption. Other similar activation pretreatments have been reported in the literature. Molinari and Parravano[66] proposed reaction 62a and reaction 64 to describe the activation of ZnO. Holm and Blue[42] and unpublished data from the Frick Chemical Lab[66] indicate that several molybdenum, tungsten, and uranium oxides are not

active for the hydrogen-deuterium exchange until they are subjected to similar pretreatments.

After the catalyst has been activated, the proposed exchange reaction mechanism is given by the reactions:

$$S(OH^-) + \tfrac{1}{2}D_2 \rightarrow S(O^-) + HD \qquad (65a)$$

$$S(OD^-) + \tfrac{1}{2}H_2 \rightarrow S(O^-) + HD \qquad (65b)$$

$$S(OH^-) + S(OD^-) \rightarrow 2S(O^-) + HD \qquad (66)$$

The catalytic reaction occurs by exchange between the deuterium or hydrogen and the surface OH or OD groups, respectively, reactions 65a and 65b , or between the adsorbed OH^- and OD^- group on the surface, reaction 66. Wicke[107] has shown that reactions 65a and 65b describe the mechanism of the hydrogen-deuterium exchange reaction on alumina catalysts. This mechanism has also been proposed by Molinari and Parravano[66] to explain the hydrogen-deuterium exchange in ZnO.

In the present study the following observations substantiate the plausibility of this mechanism:

1. Thermoelectric Power Studies During Chemisorption

At high temperatures, during hydrogen adsorption, a shift in thermoelectric power corresponding to an electron transfer to the catalyst was observed. This electron transfer could be explained by reactions 63a, 63b and 64, which occur during the high temperature pretreatment of the catalyst. If the activation energy for Type B adsorption is greater than for Type A adsorption, which is the case for ZnO [Morrison[68]], then reactions 63a and 63b would occur at higher

temperatures.

As the temperature is lowered, the semiconductor becomes a single carrier semiconductor, and the observed change in thermoelectric power with hydrogen adsorption decreases, until, in the temperature range 80° to 100°, no change in thermoelectric power is observed during the adsorption of hydrogen. This effect may be caused by the increased predominance of Type A adsorption over Type B adsorption as the temperature is lowered. In Type A adsorption, reactions 62a and b, there is no electron transfer to the catalyst surface and consequently, no change in thermoelectric power would be expected.

Since the amount of electron transfer is small at temperatures corresponding to the exchange reaction temperature, the bending of the bands at the catalyst surface due to the build up of surface charge will be small. This means that the distance between the conduction band (and valence band) and the Fermi level will be approximately the same at the surface as it is in the bulk of the catalyst. Consequently, it would be expected that changes in the Fermi level caused by varying the Fe/Co ratio of the ferrite would influence both the catalytic properties and the surface contribution to the catalyst's thermoelectric power.

2. Hydrogen-Deuterium Exchange Data

The reaction proceeds in two stages: phase one, in which the catalytic activity increases with time, followed by phase two of constant activity. Phase one could then correspond to a reduction of the surface oxygen and an increase in the surface OH and OD concentration. The second stage is a truly catalytic stage in which the hydrogen-deuterium is

exchanged with the surface OH and OD groups. Since the OD and OH groups are formed in phase one, the measured catalytic activity of phase two should increase with time during phase one. These effects have been observed.

Air or oxygen treatment of the activated surface would reoxidize the hydrogenated surface, reducing the OH and OD concentrations and lowering the catalytic activity. It was observed that the introduction of air or oxygen during an exchange run would immediately deactivate the catalyst. The catalyst could then be reactivated by reducing the catalyst with hydrogen (or deuterium) at high temperature.

If the surface oxygen, $S(O^-)$ or $S(O^{--})$, is considered as the active site for adsorption of hydrogen and deuterium on the cobalt surface, Boreskov's relationship (see Theory section) between catalytic activity and Fermi level, described in the Theory Chapter, would apply. Reaction 63a and 63b would be analogous to Equation (30), resulting in an exchange rate of the form of Equation (34). Similarly, reaction 66 would be analogous to Equation (35), resulting in a rate of exchange of the form of Equation (40). This mechanism, then, would predict that lowering the Fermi level (becoming more p-type) should increase the catalytic activity. The activation energy for hydrogen-deuterium exchange reaction was observed to be lower for the p-type ferrite than for the n-type. Although the pre-exponential factor varied in such a manner as to compensate for the change in activation energy, causing only small variation in the overall reaction rate with Fermi level, the direction of the observed change in catalytic activity is

consistent with the direction of the change in Fermi level of the catalyst, as predicted by Boreskov's relationships.

VI. CONCLUSIONS

The hydrogen-deuterium exchange reaction on cobalt ferrite occurs in two stages: (1) The first stage is an activation stage, in which the catalytic activity increases with time. This step might be associated with the reduction of oxygen on the surface of the ferrite, and the corresponding formation of OH and OD groups. (2) In the second stage, the catalytic exchange reaction occurs with constant activity. In this step, it seems likely that exchange occurs between hydrogen and deuterium and the OD and OH groups formed in stage one. This reaction mechanism is consistent with the data of this study and has been used in previous investigations to explain the hydrogen-deuterium reactions on other catalysts. The activation energy for the hydrogen-deuterium exchange reaction on the cobalt ferrite is lower on p-type than on n-type ferrite. A compensation effect was observed between the activation energy and pre-exponential factor.

In four runs made to determine the effect of p-n junctions on catalytic activity, no increase in catalytic activity was observed on mixed, sintered p- and n-type catalysts. Since the relative surface area of p-n junction, produced by sintering the mixed ferrite, could not be determined, it may only be concluded that either (1) the junction is not appreciably more active for the exchange reaction, or (2) the relative area of p-n junction produced by the sintering process was so small that any increase (or decrease) in catalytic activity at the junction would not affect the overall activity of the catalyst.

This study has also furnished data which, along with previous investigations reported in the literature, indicate that the changes in thermoelectric power of particulate systems due to gas chemisorption may be used to gain an insight into electron exchange occuring at the solid surface.

Future work of interest would be to study the oxygen and hydrogen adsorption isotherms on cobalt ferrite and the electron transfer during adsorption. These investigations would shed further light into the mechanism of the exchange reaction.

APPENDIX I

EXPERIMENTAL DATA

A. Raw Data and Calculated Per Cent Conversions for Hydrogen-Deuterium Exchange Runs

TABLE VIII. Preliminary Runs at Constant Temperature (Run 72) and Constant Flow Rate (Run 74)

Sample	Time (min)	Temp. (°C)	Flow (cc. min.)	Mass Spec. Peak Height H_2	HD	D_2	Per Cent Conversion
Run 72, Catalyst $Co_{1.07}Fe_{1.93}O_4$							
C	100	124.5	20	2418	36.3	30.4	.374
D	123	126.25	20	2190	33.5	27.2	.381
E	140	126.25	20	2352	36.3	29.2	.383
F	160	126.25	20	2274	35.5	28.4	.384
G	180	126.25	37	2589	28.3	38.1	.271
H	200	126.25	37	2385	25.7	25.1	.268
I	220	126.25	37	2424	26.2	35.8	.268
J	247	126.25	37	2298	25.2	33.8	.272
K	275	126.25	20	2424	38.7	30.2	.390
L	305	126.25	20	2490	40.8	32.0	.390
M	325	126.75	20	2358	38.6	30.6	.387
N	345	126.5	37	2481	27.6	36.4	.275
O	365	126.5	37	2451	26.7	36.2	.269
P	385	126.5	37	2310	25.0	34.3	.267
Q	405	126.5	37	2433	25.9	36.2	.264
R	425	126.5	20	2439	38.3	30.4	.387
S	445	126.5	20	2430	37.3	30.6	.379
T	460	126.25	20	2304	35.3	29.1	.378
U	475	126.25	20	2499	38.1	31.3	.378

Sample	Time (min)	Temp. (°C)	Flow (cc. min.)	Mass Spec. Peak Height H_2	HD	D_2	Per Cent Conversion
Run 74, Catalyst $Co_{1.07}Fe_{1.93}O_4$							
A	58	144.25	20	1779	33.6	19.6	.462
B	56	144.0	20	2064	39.4	22.3	.469
C	120	143.75	20	2160	41.1	23.4	.468
D	140	137.2	20	1773	29.4	21.4	.407
E	160	137.0	20	2181	34.4	27.0	.389
F	180	136.9	20	2376	37.3	29.6	.387
G	200	131.0	20	2172	29.2	29.4	.332
H	224	131.0	20	2412	32.0	23.2	.325
I	240	130.8	20	2340	30.4	32.4	.319
J	260	122.75	20	1950	19.2	29.4	.246
K	280	122.75	20	2376	23.5	36.4	.244
L	300	123.2	20	2328	23.0	35.9	.243
M	320	131.5	20	2382	31.5	32.9	.324
N	340	131.0	20	2409	31.3	33.4	.319
O	360	131.0	20	2412	31.5	33.5	.321
P	380	136.3	20	2427	37.3	30.6	.379
Q	400	136.2	20	2427	37.0	30.6	.372
R	420	136.2	20	2415	36.4	30.7	.372
S	440	143.6	20	2460	45.4	27.1	.456
T	460	143.8	20	2397	44.1	26.8	.452
U	480	143.8	20	2409	44.7	26.9	.454

TABLE IX. Mixed P- and N-Type Catalyst Runs

Sample	Time (min)	Temp. (°C)	Flow (cc. min.)	Mass Spec. Peak Height H_2	HD	D_2	Per Cent Conversion
Run 125, Catalyst 50%$Co_{1.07}Fe_{1.93}O_4$, 50%$Co_{0.93}Fe_{2.07}O_4$ (not sintered)							
D	60	74.0	20.0	4350	96.6	58.1	.454
E	80	74.1	20.0	4530	103.5	59.7	.461
F	100	72.3	19.9	4350	86.2	63.1	.408
G	115	70.0	20.5	4380	75.7	63.4	.353
H	130	67.0	19.9	4400	62.0	77.1	.287
I	150	71.0	15.0	4370	97.8	56.8	.463
J	170	69.2	15.0	4380	89.2	63.2	.414
K	190	67.0	15.0	4320	75.9	68.1	.358
L	210	64.5	15.0	4330	64.3	74.8	.301
M	240	68.6	9.8	4380	115.8	50.2	.335
N	270	66.2	9.9	4530	100.2	58.4	.461
O	300	64.5	9.85	4390	89.2	63.3	.413
P	330	62.0	9.9+	4350	74.9	69.4	.350
Q	360	59.5	9.9	4560	65.8	79.0	.294

Sample	Time (min)	Temp. (°C)	Flow (cc. min.)	Mass Spec. Peak Height H_2	HD	D_2	Per Cent Conversion
Run 126, Catalyst 50%$Co_{1.07}Fe_{1.93}O_4$, 50%$Co_{0.93}Fe_{2.07}O_4$ (sintered 850°, 1 hour)							
A	90	77.8	20.0	3940	81.7	49.1	.454
B	110	74.7	20.0	3940	70.1	54.7	.391
C	130	72.6	20.0	4030	62.3	60.3	.341
D	150	70.2	20.0	4070	53.3	66.2	.287
E	175	72.4	14.9+	4080	78.5	54.1	.420
F	205	70.5	14.9+	4000	58.1	57.9	.370
G	230	68.25	15.0	4020	59.4	63.8	.318
H	255	65.8	15.0	4110	49.1	62.4	.261
I	325	68.2	9.8	4060	78.1	53.7	.421
J	355	66.0	9.9	4080	68.7	58.9	.368
K	425	64.0	9.9	4060	60.1	63.2	.322
L	455	61.8	9.9	4060	50.9	67.9	.273

Sample	Time (min)	Temp. (°C)	Flow (cc. min.)	Mass Spec. Peak Height H_2	HD	D_2	Per Cent Conversion
Run 127, Catalyst 50%$Co_{1.07}Fe_{1.93}O_4$, 50%$Co_{0.93}Fe_{2.07}O_4$ (sintered 990°C, 1 hr.)							
A	85	71.2	20.0	3720	75.4	48.8	.436
B	105	69.5	19.9	3950	72.5	56.1	.393
C	125	67.0	20.0	4140	64.8	64.4	.335
D	145	65.1	20.0	4190	56.6	69.0	.291
E	170	67.7	15.5	4090	81.5	53.9	.431
F	195	65.9	15.0	4130	74.7	58.8	.388
G	225	63.7	15.0	4200	64.6	65.9	.329
H	250	61.4	15.0	4140	54.6	69.4	.282
I	275	62.8	10.0	4180	82.5	56.1	.424
J	305	61.0	9.9	4270	75.3	61.8	.379
K	335	59.0	9.9	4180	64.4	65.5	.330
L	370	57.0	9.9	4140	54.7	69.4	.283

Sample	Time (min)	Temp. (°C)	Flow (cc. min.)	Mass Spec. Peak Height H_2	HD	D_2	Per Cent Conversion
Run 128, Catalyst 50%$Co_{1.07}Fe_{1.93}O_4$, 50%$Co_{0.93}Fe_{2.07}O_4$ (sintered 1100°C, 1 hr.)							
A	140	74.2	20.0	4000	77.9	54.2	.418
B	160	72.5	19.9	3920	68.1	57.1	.374
C	180	70.2	20.0	4100	61.2	54.5	.322
D	200	68.0	20.0	4150	52.4	70.2	.272
E	225	70.3	14.0	3880	71.8	53.6	.401
F	250	68.5	15.0	4150	68.2	61.9	.355
G	275	66.3	15.0	4100	57.7	66.4	.303
H	300	64.0	15.0	4140	48.8	71.8	.254
I	330	65.0	9.8	4090	71.9	58.8	.379
J	360	63.3	9.8+	4220	67.2	64.8	.341
K	390	61.0	9.85	3970	53.4	65.9	.288
L	420	59.0	9.9	4090	46.8	71.7	.246

TABLE X. High Temperature Runs

Sample	Time (min)	Temp. (°C)	Flow (cc. min.)	Mass Spec. Peak Height H_2	HD	D_2	Per Cent Conversion
Run 76, Catalyst $Co_{1.07}Fe_{1.93}O_4$							
B	115	110.25	20.2	2373	48.2	23.8	.503
C	170	105.3	19.8	2514	43.1	28.9	.427
D	215	100.4	19.7	2520	34.9	33.3	.344
E	260	95.6	19.8	2487	26.1	37.1	.260
F	315	104.8	36.8	2403	25.8	35.9	.264
G	360	110.4	36.4	2469	33.6	33.6	.333
H	429	114.5	37.1	2428	31.5	25.6	.381
I	470	119.75	36.0	2463	45.0	27.1	.448
Run 77, Catalyst $Co_{1.07}Fe_{1.93}O_4$							
A	90	115.4	19.3	2601	51.0	26.2	.493
B	135	110.0	19.4	2571	42.1	30.0	.412
C	180	104.8	19.0	2589	34.9	34.4	.332
D	225	100.7	19.3				
E	270	109.8	36.4	2739	29.1	39.9	.267
F	315	115.1	36.0	2808	38.7	36.8	.345
G	360	120.2	36.0	2505	42.2	29.1	.420
H	405	124.75	36.0	2865	56.0	29.7	.484
Run 78, Catalyst $Co_{1.07}Fe_{1.93}O_4$							
A	80	120.5	19.3	2406	53.7	21.1	.560
B	130	115.0	19.5	2370	46.3	24.8	.483
C	185	109.5	19.3	2367	38.5	28.7	.401
D	230	105.0	19.2	2430	33.4	32.3	.341
E	375	114.0	35.2	2433	32.7	33.2	.330
F	320	120.3	35.0	2469	40.7	29.9	.405
G	365	125.1	35.1	2412	46.1	25.8	.472
H	410	130.1	35.2	2259	48.4	21.5	.530
Run 80, Catalyst $Co_{1.03}Fe_{1.97}O_4$							
E	95	119.5	19.1	2319	41.7	27.0	.436
F	115	119.5	19.1	2307	42.8	26.5	.447
G	135	119.5	19.1	2316	43.5	26.7	.449
H	166	115.5	19.2	2334	37.7	29.9	.387
I	180	115.6	19.4	2322	37.2	29.8	.384
J	215	109.8	19.5	2364	29.7	34.3	.302
K	230	109.8	19.1	2373	29.7	34.6	.300
L	250	105.4	19.1	2361	23.2	37.7	.236
M	275	115.0	34.9	2406	23.8	38.4	.237
N	290	114.8	34.7	2406	24.2	38.5	.239
O	315	109.8	34.9	2415	30.5	35.3	.301
P	340	125.0	34.7	2418	28.0	31.4	.377
Q	365	130.2	34.8	2412	45.4	27.7	.450
R	400	117.1	19.7	2412	41.4	29.5	.412
Run 81, Catalyst $Co_{1.03}Fe_{1.97}O_4$							
E	170	125.0	19.5	2442	41.0	29.2	.412
F	190	120.1	19.7	2541	35.7	33.8	.346
G	210	120.1	19.7	2442	34.1	32.9	.329
H	245	115.25	19.7	2709	31.6	39.5	.282
I	290	109.9	19.4	2430	21.6	38.2	.220
J	320	119.8	34.9	2520	23.2	40.2	.224
K	350	124.5	34.8	2436	27.3	35.9	.275
L	380	129.7	34.8	2436	33.0	33.3	.334
M	420	136.25	34.7	2481	42.3	29.8	.415
Run 82, Catalyst $Co_{1.03}Fe_{1.97}O_4$							
A	75	125.6	19.6	2346	34.4	29.2	.371
B	100	125.6	19.6	2340	35.2	29.1	.377
C	130	120.6	19.4	2274	28.2	31.1	.312
D	160	115.3	19.4	2358	23.7	35.3	.251
E	195	110.0	19.8	2343	18.2	37.9	.194
F	220	120.5	34.7	2373	19.1	38.2	.200
G	250	120.5	35.0	2448	19.4	38.5	.201
H	280	125.7	34.8	2355	23.4	35.4	.249
I	316	129.5	34.5	2430	29.3	34.1	.293
J	350	134.2	34.3	2379	33.7	31.4	.349

Sample	Time (min)	Temp. (°C)	Flow (cc. min.)	Mass Spec. Peak Height H_2	HD	D_2	Per Cent Conversion
Run 83, Catalyst $Co_{0.98}Fe_{2.02}O_4$							
K	320	120.2	19.5	2430	46.1	26.8	.462
L	340	120.2	19.2	2340	45.7	25.0	.477
M	360	120.2	19.2	2391	46.6	25.9	.474
N	390	116.0	19.2	2439	40.6	30.1	.399
O	430	109.75	19.0	2436	29.1	35.3	.292
P	460	105.1	19.3	2430	21.4	39.0	.215
Q	500	115.4	35.7	2469	25.4	38.1	.250
R	525	119.5	34.9	2415	30.7	24.2	.310
S	548	124.5	35.5	2274	36.2	28.9	.385
T	575	130.0	35.5	2376	46.6	25.6	.477
Run 84, Catalyst $Co_{0.98}Fe_{2.02}O_4$							
A	20	125.0	19.4	2304	47.1	22.9	.507
B	40	125.0	19.4	2292	49.1	22.4	.523
C	60	125.25	19.8	2313	50.3	22.6	.527
D	90	119.8	19.1	2328	41.5	27.1	.434
E	120	114.9	19.4	2364	33.3	31.4	.347
F	150	110.1	19.3	2364	26.0	35.4	.269
G	175	120.0	35.7	2364	29.4	34.4	.299
H	190	120.1	35.7	2364	29.3	34.3	.299
I	220	124.5	35.7	2385	35.3	31.5	.366
J	250	130.1	35.5	2376	45.0	26.7	.457
K	280	134.8	35.5	2388	53.6	22.7	.541
Run 85, Catalyst $Co_{0.98}Fe_{2.02}O_4$							
D	110	124.9	19.2	2406	53.1	23.6	.535
E	140	124.75	19.5	2424	53.4	23.6	.531
F	170	120.2	19.6	2391	44.4	27.4	.448
G	200	115.0	19.7	2388	36.0	31.9	.361
H	230	110.2	19.7	2394	28.1	35.9	.281
I	265	119.8	48.8	2388	24.8	38.0	.246
J	290	119.75	48.6	2364	24.6	38.0	.245
K	320	124.8	48.5	2412	31.3	35.2	.308
L	350	130.2	48.4	2400	38.8	31.7	.383
M	385	135.1	48.5	2400	46.9	27.4	.461
Run 86, Catalyst $Co_{0.98}Fe_{2.02}O_4$							
D	80	125.15	19.3	2406	45.9	24.9	.479
E	100	125.2	19.3	2364	46.8	24.8	.485
F	120	125.3	19.6	2412	47.9	24.8	.491
G	150	119.8	19.6	lost sample			
H	180	114.8	19.6	2421	31.4	33.5	.319
I	210	110.1	19.6	2424	24.0	37.0	.245
J	240	120.0	35.5	2424	26.6	36.4	.267
K	270	124.8	35.1	2427	34.1	32.3	.345
L	300	129.8	35.3	2415	42.0	28.7	.421
M	330	135.25	35.5	2421	29.6	24.3	.505
Run 89, Catalyst $Co_{0.93}Fe_{2.07}O_4$							
A	70	115.2	15.6	2322	38.9	24.9	.439
B	85	115.4	19.6	2346	41.2	25.7	.450
C	100	115.4	19.6	2334	41.4	25.4	.450
D	145	115.2	19.6	2364	41.6	25.6	.445
E	175	109.8	19.6	2349	32.1	30.2	.347
F	205	104.8	19.6	2364	25.5	33.7	.274
G	235	100.0	19.6	2376	20.7	36.2	.222
H	265	110.0	35.0	2373	22.8	35.6	.243
I	295	114.9	35.0	2376	29.0	32.8	.307
J	325	120.6	34.9	2364	36.4	28.7	.388
K	355	125.0	35.2	2364	43.2	25.2	.467
Run 90, Catalyst $Co_{0.93}Fe_{2.07}O_4$							
A	80	120.7	19.6	2319	46.6	23.8	.495
B	100	120.7	19.6	2328	48.6	23.9	.504
C	120	120.9	19.6	2313	48.9	23.5	.509
D	150	114.7	19.6	2325	39.2	28.6	.407
E	180	110.0	19.7	2340	32.7	32.1	.337
F	210	105.8	19.6	2349	26.6	35.1	.274
G	240	114.8	36.6	2359	28.0	35.2	.285
H	265	120.1	36.6	2358	36.1	31.2	.366
I	295	126.5	35.9	2358	46.2	26.2	.468
J	325	134.0	36.1	2370	52.1	20.7	.587

TABLE XI. Low Temperature Runs

Sample	Time (min)	Temp. (°C)	Flow (cc. min.)	Mass Spec. Peak Height H_2	HD	D_2	Per Cent Conversion
Run 108, Catalyst $Co_{1.07}Fe_{1.93}O_4$							
H	240	69.41	15.1	2880	55.6	38.0	.427
I	255	70.5	20.0	2910	47.7	42.6	.359
J	270	70.5	20.0	2900	47.5	42.5	.358
K	285	68.5	20.0	2920	42.3	45.5	.317
L	300	68.5	20.0	2930	42.2	45.7	.316
M	315	67.25	15.0	2950	50.2	47.1	.374
N	325	67.25	15.0	2950	50.0	42.7	.369
O	345	65.75	10.0	2950	62.1	36.1	.403
P	355	65.75	9.9	2960	62.5	36.4	.462
Q	370	63.4	9.9	2970	55.4	40.4	.407
R	380	63.4	9.9	2980	54.6	40.8	.401
S	395	64.25	15.0	3000	41.9	47.4	.307
T	405	64.25	15.1	3000	41.8	47.6	.305
U	420	64.8	20.0	3020	33.9	51.5	.248
V	430	64.8	20.0	3010	33.9	51.3	.248
W	445	62.6	20.0	3020	28.9	54.3	.210
X	460	61.67	14.9	3040	35.5	51.2	.257
Y	475	60.3	9.9	3030	45.9	45.9	.333
Z	490	58.5	9.9	2850	40.9	48.4	.297
a	505	59.7	14.9	3030	30.4	53.9	.220
b	520	60.25	19.9	3060	42.2	57.3	.174
Run 110, Catalyst $Co_{1.07}Fe_{1.93}O_4$							
M	100	75.0	25.0	2670	39.1	40.6	.325
N	115	74.8	25.0	2700	40.3	41.0	.329
O	130	74.8	25.0	2710	41.3	40.7	.337
P	145	74.5	25.0	2730	41.9	40.7	.340
Q	175	74.0	20.0	2730	51.2	36.5	.417
R	190	74.0	20.0	2760	52.7	36.5	.419
S	205	73.75	15.0	2730	63.7	30.5	.511
T	225	73.75	15.0	2750	63.6	30.7	.506
U	240	73.0	9.9	2750	79.2	22.8	.635
V	255	73.0	10.0	2700	79.4	23.1	.635
W	285	70.8	9.9	2770	72.5	27.3	.570
X	310	71.6	9.9	2780	55.5	35.6	.438
Y	325	70.9	20.0	2800	43.7	42.0	.342
Z	340	68.6	20.0	2810	38.2	44.1	.300
a	355	68.6	15.0	2780	47.8	39.2	.379
b	400	68.0	9.9	2800	63.9	32.1	.499
c	425	65.75	9.9	2830	56.4	36.2	.438
d	445	65.5	15.0	2880	40.7	45.3	.310
e	600	65.25	20.0	2850	29.8	49.3	.231
Run 111, Catalyst $Co_{1.03}Fe_{1.97}O_4$							
E	160	76.0	20.0	2550	46.6	31.5	.425
F	175	76.0	20.0	2571	49.6	33.3	.427
G	190	76.0	20.0	2571	51.0	34.0	.429
H	205	73.25	20.0	2568	43.8	38.0	.366
I	220	73.25	15.0	2598	55.7	33.1	.457
J	240	62.5	9.9	2592	60.4	26.2	.491
K	255	70.20	15.0	2725	47.0	38.2	.381
L	270	29.75	20.0	2673	36.6	44.1	.293
M	285	67.25	20.0	2661	30.8	46.7	.248
N	300	67.25	15.0	2643	40.0	42.1	.322
O	320	67.0	9.9	2661	52.8	36.0	.423
P	340	64.4	9.9	2655	45.6	39.2	.368
Q	353	64.6	15.0	2706	32.6	47.1	.257
R	375	62.0	9.9	2664	38.2	43.6	.307
Run 112, Catalyst $Co_{1.03}Fe_{1.07}O_4$							
G	25	77.4	20.1	2592	53.4	32.0	.455
H	45	77.4	20.1	2664	55.7	43.3	.448
I	60	77.3	20.0	2667	55.8	34.9	.444
J	75	77.15	20.0	2709	55.8	35.9	.437
K	105	74.2	20.0	2715	47.4	39.9	.373
L	110	74.1	20.0	2667	57.7	33.8	.460
M	140	70.8	9.9	2718	65.0	31.3	.510
N	155	71.25	14.9	2739	49.1	35.4	.356
O	170	71.5	20.0	2745	40.2	44.3	.312
P	185	68.2	20.0	2784	33.3	43.6	.255
Q	200	68.3	15.0	2787	43.0	43.8	.329
R	220	68.3	9.9	2766	57.2	36.6	.439
S	240	66.0	9.85	2784	50.9	46.0	.389
T	255	65.2	15.0	2778	34.3	48.1	.263
U	275	63.0	9.9	2781	47.0	44.3	.322

Sample	Time (min)	Temp. (°C)	Flow (cc. min.)	Mass Spec. Peak Height H_2	HD	D_2	Per Cent Conversion
Run 120, Catalyst $Co_{0.98}Fe_{2.02}O_4$							
B	25	71.0	20.0	2427	37.8	28.1	.402
C	45	71.2	20.0	2433	43.5	31.5	.408
D	60	71.3	19.9	2484	46.8	32.9	.416
E	75	71.5	20.0	24.66	47.8	33.0	.420
F	95	71.5	19.9	2514	49.7	33.3	.427
G	125	69.5	20.1	2526	43.7	36.8	.373
H	140	67.0	20.0	Lost sample			
I	155	64.25	20.0	2562	29.7	44.8	.249
J	170	64.25	19.9	2559	29.4	44.7	.247
K	185	65.8	20.0	2568	33.2	42.9	.279
L	200	68.1	20.0	2580	40.2	39.5	.337
M	225	68.1	15.0	2568	50.4	350	.419
N	240	65.75	15.0	2559	42.0	38.4	.354
O	255	63.4	15.1	2607	35.8	42.8	.295
P	270	61.0	15.0	2592	29.2	45.2	.244
Q	290	64.7	15.0	2598	40.0	40.0	.333
R	310	65.0	9.9	2607	54.5	33.3	.450
S	330	63.2	9.85	2622	48.3	36.6	.398
T	350	60.75	9.85	2622	41.0	40.7	.335
U	370	58.3	9.85	2646	33.4	44.3	.274
Run 121, Catalyst $Co_{0.98}Fe_{2.02}O_4$							
A	60	70.0	19.9	2452	40.1	37.3	.350
B	95	71.8	20.0	2427	48.1	32.4	.426
C	115	72.0	20.0	2175	43.9	28.6	.434
D	130	72.3	20.0	1914	42.0	26.2	.445
E	150	70.3	20.0	1989	35.1	28.1	.384
F	165	68.3	19.9	1986	29.6	31.1	.322
G	180	65.7	20.0	1971	24.4	33.4	.268
H	195	62.3	20.0	1965	32.8	29.2	.360
I	210	69.1	15.0	2010	41.6	26.2	.443
J	225	67.3	15.0	1986	36.1	28.4	.389
K	240	65.1	15.0	1974	30.2	30.7	.330
L	255	62.75	14.9	1977	25.0	33.4	.272
M	270	60.25	15.0	1998	20.6	36.1	.222
N	285	65.9	9.9	1971	43.7	24.3	.473
O	305	63.5	9.8	1986	37.2	28.2	.397
P	325	60.0	9.9	1992	28.4	32.4	.305
Q	345	56.8	9.9+	1955	21.1	34.6	.234
Run 123, Catalyst $Co_{0.93}Fe_{2.07}O_4$							
A	25	72.5	20.0	4540	67.0	65.1	.340
B	40	72.5	20.0	4570	71.4	67.8	.345
C	55	72.5	19.9	4560	71.6	67.8	.344
D	70	70.0	20.0+	4590	59.0	75.2	.282
E	85	66.6	20.0	4630	44.6	82.9	.212
F	100	63.6	20.0	4660	34.6	88.8	.163
G	130	68.4	15.0	4660	66.5	73.5	.311
H	145	65.7	15.0	4700	54.1	80.7	.250
I	160	62.5	15.0-	4710	41.2	86.5	.152
J	175	60.0	15.0-	4740	32.8	91.1	.153
K	195	64.8	9.8	4730	71.2	72.3	.330
L	215	62.6	9.85	4730	60.1	78.2	.278
M	235	60.0	9.85	4770	48.9	84.8	.224
N	255	57.0	9.8+	4800	37.1	20.4	.170
Run 124, Catalyst $Co_{0.93}Fe_{2.07}O_4$							
A	0	75.1	19.9	4810	98.1	60.4	.448
B	15	75.1	20.0	4890	99.9	61.9	.447
C	30	72.7	20.0	4910	83.8	70.3	.373
D	45	69.4	20.0	4810	63.6	78.4	.289
E	60	66.1	20.0	4910	48.8	88.0	.217
F	80	70.9	14.9	4930	90.9	67.6	.402
G	100	68.7	15.0-	4890	75.1	74.1	.336
H	115	65.8	15.0	4960	61.6	82.3	.272
I	130	62.5	15.0	4950	46.3	89.8	.205
J	155	66.2	9.8	4860	91.2	66.6	.406
K	175	64.75	9.9	4970	77.7	74.1	.344
L	195	62.0	9.9	5000	63.1	83.3	.275
M	215	58.5	9.9+	4930	46.8	90.8	.205

B. Raw Data and Calculated Thermoelectric Power for Adsorption Runs

TABLE XII.

Adsorption Runs

Time	Atmosphere	ΔT (millivolts Cr-Al couple)	EMF (millivolts)	Thermoelectric Power, μV/°C
Run No. 112, Catalyst- $Co_{1.09}Fe_{1.91}O_4$, Temperature- 250°C				
1:43	He+2cm O_2	0.8576	10.6270	+532
1:48		0.3370	3.7800	
1:55	"	0.2955	3.5269	+538
2:00		0.8518	10.8557	
2:15	"	0.8704	11.1547	+545
2:22		0.3161	3.7912	
2:45	"	0.3035	3.7266	+551
2:50		0.8557	11.1630	
3:30	"	0.8759	11.5384	+561
3:35		0.3230	3.9865	
4:38	"	0.2928	3.6725	+561
4:45		0.8561	11.3563	
7:26	"	0.9306	12.5239	+574
7:35		0.2876	3.5255	
10:40	"	0.2700	3.4520	+571
11:00		0.9016	12.2210	
Run No. 113, Catalyst- $Co_{1.09}Fe_{1.91}O_4$, Temperature- 250°C				
8:15	Helium	0.9023	9.8052	+470
8:30	"	0.2811	2.6827	
8:43	"	0.2620	1.850	+220
8:49		0.8308*	4.905	
8:50	He+1cm H_2	*	4.7116	+212
8:51	"	*	4.3450	+195
8:52	"	*	4.0490	+182
8:53	"	*	3.8520	+176
8:54	"	*	3.6840	+165
8:55	"	*	3.5490	+159
8:56	"	*	3.4570	+155
8:57	"	*	3.3790	+152
8:58	"	*	3.317	+148
8:59	"	*	3.261	+146
9:00	"	*	3.211	+144
9:01	"	*	3.167	+142
9:02	"	*	3.125	+140
9:03	"	*	3.085	+139
9:04	"	*	3.047	+137
9:05	"	*	3.015	+135
9:06	"	*	2.984	+134
Run No. 114, Catalyst- $Co_{0.96}Fe_{2.04}O_4$, Temperature- 250°C				
10:30	Helium	0.8507	-7.2632	-356
10:40	"	0.2037	-1.6271	
11:35	He+1cm H_2	0.8527	-7.545	-370
11:36	"	*	-7.839	-384
11:37	"	*	-7.970	-391
11:38	"	*	-8.148	-400
11:39	"	*	-8.267	-406
11:40	"	*	-8.404	-413
11:41	"	*	-8.546	-419
11:42	"	*	-8.631	-423
11:43	"	*	-8.782	-431
11:44	"	*	-8.850	-435
11:45	"	*	-8.901	-437
11:46	"	*	-8.939	-439
11:47	"	*	-8.966	-440
11:48	"	*	-8.981	-441
11:49	"	*	-8.990	-442
11:50	"	*	-9.000	-443
3:20	Helium	0.8108	-7.4514	-386
3:25	"	0.2162	-1.8501	
3:30	He+1cm O_2	0.2072	-1.6901	-387
3:35	"	0.7873	-7.1873	
4:00	"	0.8364	-7.7946	-387
4:05	"	0.2225	-1.9769	
4:30	"	0.1438	-1.3420	-358
4:35	"	0.7863	-6.9451	
5:00	"	0.8276	-6.8115	-337
5:10	"	0.1899	-1.4865	
6:05	"	0.1404	-1.0660	-209
6:15	"	0.8106	-4.4575	

*ΔT assumed unchanged from previous reading.

Time	Atmosphere	ΔT (millivolts Cr-Al couple)	EMF (millivolts)	Thermoelectric Power, μV/°C
Run No. 119, Catalyst- $Co_{0.96}Fe_{2.04}O_4$, Temperature- 250°C				
4:18	Helium	0.8215	-6.3419	-302
4:22		0.0970	-0.4059	
4:29	He+2cm H_2	0.8612	-6.4121	-305
4:30	"	*	-7.100	-338
4:31	"	*	-7.325	-348
4:32	"	*	-7.519	-358
4:33	"	*	-7.711	-367
4:34	"	*	-7.883	-375
4:35	"	*	-8.024	-383
4:36	"	*	-8.116	-386
4:37	"	*	-8.225	-391
4:38	"	*	-8.301	-396
4:39	"	*	-8.305	-398
4:40	"	*	-8.387	-399
4:49	He+2cm O_2	0.6591	-8.471	-408
4:50	"	*	-7.700	-366
4:51	"	*	-7.525	-358
4:52	"	*	-7.354	-350
4:53	"	*	-7.091	-338
4:54	"	*	-6.811	-324
4:55	"	*	-6.546	-311
4:56	"	*	-6.351	-302
4:57	"	*	-6.125	-291
4:58	"	*	-5.864	-279
4:59	"	*	-5.641	-268
5:00	"	*	-5.358	-255
Run No. 120, Catalyst- $Co_{0.96}Fe_{2.04}O_4$				
7:15	Helium	0.8240	6.9767	+300
7:20		0.0890	0.4585	
7:29	He+2cm H_2	*	6.8960	+296
7:30	"	*	6.742	+290
7:31	"	*	6.505	+279
7:32	"	*	6.441	+276
7:33	"	*	6.277	+270
7:34	"	*	6.105	+263
7:35	"	*	5.929	+255
7:36	"	*	5.740	+247
7:37	"	*	5.530	+237
7:38	"	*	5.267	+227
7:39	"	*	5.071	+218
7:40	"	*	4.860	+209
8:00	He+2cm O_2	*	4.770	+205
8:01	"	*	10.650	+461
8:02	"	*	10.875	+470
8:03	"	*	10.972	+474
8:04	"	*	11.025	+477
8:05	"	*	11.045	+477
8:06	"	*	11.053	+477
8:07	"	*	11.052	+477
8:08	"	*	11.046	+477
8:09	"	*	11.022	+477
Run no. 126, Catalyst- $Co_{1.09}Fe_{1.91}O_4$, Temperature- 250°C				
1:30	Helium	0.6025	6.629	+453
1:40	"		6.890	+465
1:45	"	0.6050	6.825	+463
1:50	"	*	6.760	+461
1:55	"	0.5964	6.606	+456
2:00	"	0.5872	6.520	+456
2:05	"	0.5809	6.456	+456
2:10	"	0.5804	6.493	+457
2:12	He+2cm O_2	0.5856	7.707	+541
2:15	"	0.5806	7.817	+553
2:20	"	0.5807	7.939	+560
2:30	"	0.5752	8.041	+572
2:45	"	0.5808	8.200	+578
3:00	"	0.5805	8.242	+582
3:40	"	0.5876	8.290	+582
4:13	Helium	0.5913	7.905	+548
4:25	He+2cm H_2	0.5732	4.63	+321
4:26	"	*	4.27	+305
4:27	"	*	3.98	+384
4:28	"	*	3.76	+269
4:29	"	*	3.65	+261
4:30	"	*	3.45	+246
4:31	"	*	3.30	+236
4:34	"	*	3.12	+222
4:35	"	*	2.98	+213
4:40	"	*	2.70	+193
4:45	"	*	2.46	+176
4:50	"	*	2.23	+162
7:25	"	0.6319	1.16	+ 75
8:00	"	0.6018	1.03	+ 69
9:00p.m.	"	0.6403	.95	+ 61

*ΔT assumed unchanged from previous reading.

B. Raw Data and Calculated Thermoelectric Power for Adsorption Runs

TABLE XII. (continued)

Adsorption Runs

Time	Atmosphere	ΔT (millivolts Cr-Al couple)	EMF (millivolts)	Thermoelectric Power, μV/°C
Run No. 149, Catalyst- $Co_{1.09}Fe_{1.91}O_4$, Temperature 140°C				
9:05	Helium	0.3469	5.071	+598
9:08	"	0.3157	4.941	+640
9:26	"	0.3341	5.211	+640
9:37	"	0.3414	5.203	+630
9:40	He+6cm H_2	0.3410	5.226	+633
9:55	"	0.3441	5.206	+627
10:17	"	0.3408	5.266	+633
10:44	"	0/3369	5.200	+634
11:25	"	0.3362	5.132	+628
11:55	"	0.3349	5.135	+699
1:10	"	0.3373	5.139	+626
1:17	"	0.3368	5.102	+626
1:36	"	0.3362	5.128	+626
2:17	"	0.3338	5.668	+625
2:55	"	0.3348	5.561	+619
3:20	"	0.3332	5.034	+620
4:06	"	0.3316	4.936	+613
4:15	"	0.3223	4.984	+672
8:25	Helium	0.3430	5.068	+607
8:45	"	0.3334	5.020	+618
9:00	"	0.3350	4.9885	+616
9:01	He+6cm O_2	0.3377	5.431	+659
9:11	"	0.3400	5.645	+680
9:25	"	0.3355	5.415	+664
9:47	"	0.3338	5.536	+674
10:21	"	0.3331	5.555	+684
11:15	"	0.3366	5.336	+676
Run No. 150, Catalyst- $Co_{0.96}Fe_{2.04}O_4$, Temperature 88°C				
10:35	Helium	0.2485	-1.4825	-244
10:40	"	0.3025	-1.7264	-235
10:45	"	0.2621	-1.5405	-241
11:00	"	0.2561	-1.5015	-241
11:15	"	0.2525	-1.4785	-241
11:20	He+6cm H_2	0.2497	-1.4762	-243
11:26	"	0.2461	-1.4392	-239
11:44	"	0.2445	-1.4322	-240
12:05	"	0.2456	-1.4535	-243
12:40	"	0.2479	-1.4575	-242
12:59	"	0.3483	-1.4605	-242
1:15	"	0.2486	-1.4667	-242
3:50	"	0.2489	-1.4615	-241
12:00	"	0.2600	-1.5115	-235
11:55		0.2617	-1.4722	-232
12:36		0.2482	-1.429	-246
12:47	"	0.2422	-1.448	-245
12:55	"	0.2436	-1.454	-245
1:12	"	0.2422	-1.458	-246
1:15	He+6cm O_2	0.2749	-1.489	-246
1:31	"	0.2499	-1.408	-246
2:02	"	0.2494	-1.503	-249
2:50	"	0.2531	-1.536	-249
4:00	"	0.2489	-1.562	-247
4:30	"	0.2470	-1.483	-246
4:55	"	0.2440	-1.471	-247
8:05	"	0.2484	-1.490	-246
Run No. 152, Catalyst- $Co_{1.09}Fe_{1.91}O_4$, Temperature 250°C				
11:00	Helium	0.6843	6.4105	+385
8:00	"	0.6522	6.2801	+395
8:35	He+2cm O_2	0.6219	6.9265	+460
9:00	"	0.6321	8.0105	+519
9:30	"	0.6575	8.9979	+560
10:10	"	0.6596	9.4334	+590
10:55	"	0.6604	9.5825	+595
11:55	"	0.6672	9.9505	+603
1:10	He+2cm H_2	0.6465	8.1565	+520
1:30	"	0.6277	5.7830	+378
2:00	?	0.6329	4.4892	+290
2:30	"	0.6199	3.6301	+240
3:00	"	0.6319	3.1598	+205
3:30	"	0.6355	2.9401	+190
4:00	"	0.6216	2.7356	+186
4:30	"	0.6242	2.6045	+172
5:00	"	0.6314	2.5911	+168
Run No. 153, Catalyst- $Co_{1.09}Fe_{1.91}O_4$, Temperature 250°C				
12:20	Helium	0.5408	4.3696	+332
7:30	"	0.5330	4.8789	+335
7:45	He+2cm O_2	0.5212	4.9102	+385
8:00	"	0.5117	5.2398	+420
8:30	"	0.5218	5.7422	+450
9:00	"	0.5099	5.8382	+470
9:30	"	0.5100	5.9810	+481
10:00	"	0.5212	6.1585	+485
10:30	"	0.5222	6.1207	+482
11:00	"	0.5177	6.1900	+488
11:30	"	0.5206	6.1524	+425
12:00	"	0.5311	6.3385	+488
Run No. 153, continued				
3:00	He+2cm H_2	0.5421	5.0212	+380
3:30	"	0.5401	3.9485	+300
4:10	"	0.5399	3.4877	+265
4:30	"	0.5378	2.9453	+225
5:00	"	0.5365	2.6848	+205
6:00	"	0.5378	2.4307	+185
6:30	"	0.5377	2.2351	+170
7:00	"	0.5384	2.2362	+170
7:30	"	0.5212	2.0995	+165
8:00	"	0.5271	20.310	+158
10:00	"	0.5317	1.8794	+145
12:00	"	0.5301	1.7442	+135
Run No. 155, Catalyst- $Co_{0.96}Fe_{2.04}O_4$, Temperature 250°C				
8:00	Helium	0.7939	-7.1658	-369
8:05	"	0.7907	-7.2012	-372
9:25	"	0.8021	-7.1765	-367
9:30	He+2cm H_2	0.7990	-7.2013	-371
10:06	"	0.7900	-9.3950	-486
10:12	"	0.7917	-9.6226	-499
10:24	"	0.7929	-9.3721	-483
10:35	"	0.7939	-8.7067	-450
10:45	"	0.7965	-7.9370	-409
10:58	"	0.7895	-7.3278	-384
11:15	"	0.7917	-6.9735	-361
11:35	"	0.7947	-6.6719	-344
12:05	"	0.7956	-6.4026	-332
1:10	"	0.7903	-5.9917	-311
2:00	"	0.7838	-5.7496	-301
5:45	"	0.8000	-5.3270	-275
7:20	"	0.7707	-5.0251	-269
7:35	He+2cm O_2	0.8034	-7.4235	-380
7:50	"	0.7925	-7.7265	-400
8:05	"	0.7969	-8.1215	-420
8:30	"	0.8037	-8.4259	-432
9:00	"	0.8128	-8.8361	-446
9:30	"	0.8075	-9.0535	-459
10:00	"	0.8027	-9.1718	-467
8:00a.m.	"	0.8097	-10.112	-512
Run No. 155a, Catalyst- $Co_{0.96}Fe_{2.04}O_4$, Temperature 250°C				
10:35	Helium	0.7700	-3.002	-160
10:50	He+2cm O_2	0.7705	4.844	+258
10:55	"	0.7737	7.1925	+382
10:56	"	*	7.7920	+412
10:57	"	*	8.160	+432
10:59	"	*	8.700	+460
11:00	"	*	9.000	+476
11:01	"	*	9.181	+486
11:04	"	*	9.412	+498
11:06	"	*	9.576	+507
11:12	"	*	9.926	+526
11:16	"	*	10.183	+538
11:25	"	*	10.590	+560
11:35	He+2cm H_2	*	10.955	+580
11:45	"		11.273	+595
11:50	"	*	9.0665	+480
11:54	"	*	8.1665	+426
11:55	"	*	7.400	+391
11:58	"	*	6.300	+333
12:10	"	*	2.464	+131
12:22	"	*	-0.549	- 28
12:35	"	*	-1.934	-102
12:44	"	*	-2.558	-135
12:55	"	*	-3.333	-176
1:01	"	*	-3.648	-193
1:37	"	*	-5.129	-271
1:50	"	*	-5.504	-291
2:10	"	0.7829	-6.2412	-326
2:25	"	0.7814	-6.649	-348
2:45	"	0.7738	-7.0435	-373
3:00	"	0.7775	-7.360	-388
3:45	"	0.7810	-7.9317	-416
4:15	"	0.7786	-8.0414	-424
4:45	"	0.7781	-8.2676	-430
6:00	"	0.0770	-8.1015	-431
7:00	"	0.8067	-7.9513	-404
11:00	"	0.8030	-6.4329	-328
Run No. 157, Catalyst- $Co_{0.96}Fe_{2.04}O_4$, Temperature 160°C				
12:50	Helium	0.5036	-5.8138	-472
1:02	"	0.5034	-5.7602	-470
1:10	"	0.5038	-5.7654	-470
1:20	He+6cm H_2	0.5067	-5.7917	-470
1:25	"	0.5003	-5.7457	-471
1:40	"	0.5028	-5.6978	-463
2:00	"	0.5000	-5.5129	-455
2:25	"	0.4971	-5.3922	-445
2:45	"	0.4908	-5.2933	-441
3:30	"	0.4911	-5.2250	-436
4:25	"	0.4933	-5.1359	-429
5:55	"	0.4947	-5.0171	-419
11:15	"	0.4946	-4.7628	-395
8:00a.m.	"	0.4960	-4.6227	-382

*ΔT assumed unchanged from previous reading.

B. Raw Data and Calculated Thermoelectric Power for Adsorption Runs

TABLE XII. (continued)

Adsorption Runs

Time	Atmosphere	ΔT (millivolts Cr-Al couple)	EMF (millivolts)	Thermoelectric Power, μV/°C
Run No. 126, continued				
8:35a.m.	He+2cm H_2	0.5985	0.035	+ 2.3
9:30	"		-0.279	-19.0
9:45	"	0.6029	-0.33	-22.0
10:05	"	0.5863	-0.295	-20.0
10:30	"	0.5592	-0.286	-21.0
11:00	"	0.5708	-0.752	-18.0
11:50	"	0.5680	-0.247	-18.0
1:00p.m.	"	0.5655	-0.245	-18.0
2:00	"	0.5545	-0.915	-16.0
Run No. 138, Catalyst- $Co_{0.96}Fe_{2.04}O_4$, Temperature 250°C				
10:45	Helium	0.1148	-8.386	-300
10:52	He+6cm H_2	0.1142	-8.366	-299
10:53	"	*	-8.415	-301
10:56	"	*	-8.310	-298
11:00	"	*	-8.138	-291
11:02	"	*	-7.976	-285
11:06	"	*	-7.700	-275
11:10	"	*	-7.514	-269
11:16	"	*	-7.214	-258
11:22	"	*	-6.976	-249
11:26	"	*	-6.858	-245
11:34	"	*	-6.654	-238
11:55	"	*	-6.294	-225
12:12	"	*	-6.067	-216
12:37	"	*	-5.897	-211
12:42	"	*	-5.860	-209
1:30	"	*	-5.552	-198
6:17	"	*	-4.718	-169
10:10	"	*	-4.260	-155
11:17	He+6cm O_2	0.1103	-3.95	-143
11:19	"	*	-4.920	-178
11:20	"	*	-5.100	-185
11:23	"	*	-5.640	-204
11:26	"	*	-5.935	-215
11:31	"	*	-6.206	-296
11:38	"	*	-6.359	-230
11:50	"	*	-6.420	-233
12:00	"	*	-6.695	-242
12:07	"	*	-6.916	-251
12:19	"	*	-7.005	-254
12:50	"	*	-7.233	-262
Run No. 139, Catalyst- $Co_{0.96}Fe_{2.04}O_4$, Temperature 250°C				
3:33	Helium	0.0732	-4.724	-265
3:38	He+2cm H_2	0.0728	-4.825	-271
3:40	"	*	-5.19	-290
3:44	"	*	-5.255	-294
3:53	"	*	-5.30	-297
3:56	"	*	-5.574	-312
4:00	"	*	-5.297	-297
4:04	"	*	-4.860	-272
4:18	"	*	-4.358	-244
4:23	"	*	-4.323	-241
4:40	"	*	-4.208	-236
4:52	"	*	-4.190	-234
8:40	"	*	-3.845	-215
Run No. 141, Catalyst- $Co_{1.09}Fe_{1.91}O_4$, Temperature 250°C				
9:10	Helium	*	7.216	+384
9:30		*	7.160	+381
9:45		*	7.227	+385
9:55		*	7.777	+385
9:56	He+6cm O_2	*	10.010	+532
9:58	"	*	10.184	+540
10:02	"	*	10.265	+545
10:07	"	*	10.339	+550
10:15	"	0.7702	10.386	+552
10:20	"	0.7690	10.436	+554
10:25	"	0.7683	10.462	+556
10:30	"	0.7722	10.504	+557
10:45	"	0.7744	10.589	+558
11:00	"	0.7608	10.577	+563
1:00	Helium		10.119	
1:04	He+6cm H_2	0.7605	9.773	+527
1:06	"	*	9.503	+513
1:09	"	*	9.284	+501
1:10	"	*	9.109	+496
1:20	"	*	8.654	+466
1:25	"	*	8.435	+454
1:35	"	*	8.007	+432
1:50	"	*	7.567	+406
2:03	"	*	7.326	+394
2:21	"	*	7.023	+378
2:55	"	*	6.510	+351
4:05	"	*	6.120	+330
6:30	"	*	5.601	+302
7:50	"	*	5.462	+295

*ΔT assumed unchanged from previous reading

Time	Atmosphere	ΔT (millivolts Cr-Al couple)	EMF (millivolts)	Thermoelectric Power, μV/°C
Run No. 142, Catalyst- $Co_{0.96}Fe_{2.04}O_4$, Temperature 250°C				
7:35	Helium	0.6590	-4.605	-287
7:40	"	0.6532	-4.690	-290
7:50	"	0.6581	-4.782	-298
7:52	He+10cm H_2	*	-5.090	-311
7:55	"	*	-5.235	-325
8:02	"	*	-5.321	-331
8:06	"	*	-5.370	-333
8:27	"	*	-5.370	-333
8:37	"	*	-5.327	-331
8:45	"	*	-5.308	-330
8:48	"	*	-5.295	-328
9:31	"	*	-5.067	-314
9:53	"	*	-4.995	-310
11:05	"	*	-4.795	-295
11:55	"	*	-4.473	-277
1:10	"	*	-4.429	-274
3:55	Helium	*	-4.538	-290
3:57	He+10cm O_2	*	-4.821	-308
3:59	"	*	-4.210	-314
4:00	"	*	-5.004	-320
4:02	"	0.6410	-5.281	-338
4:05	"	0.6431	-5.475	-350
4:10	"	*	-5.656	-362
4:17	"	*	-5.855	-374
4:23	"	*	-5.967	-386
4:30	"	0.6615	-6.073	-389
4:40	"	*	-6.182	-395
4:45	"	*	-6.231	-399
8:40	"	*	-7.239	-469
12:00	"	*	-7.468	-478
Run No. 143, Catalyst- $Co_{1.09}Fe_{1.91}O_4$, Temperature 250°C				
9:10	Helium	0.6374	7.309	+468
10:10	"	0.6792	7.082	+462
10:25	He+6cm H_2	0.6327	6.938	+447
10:30	"	0.6287	6.820	+446
10:35	"	0.6298	6.743	+439
10:50	"	0.6257	6.359	+417
11:37	"	*	5.795	+379
12:01	"	*	5.443	+356
12:57	"	0.6275	5.114	+334
1:55	"	0.6230	4.835	+317
2:42	"		4.690	+306
4:02	Helium		4.931	+324
4:05	He+6cm O_2	0.6073	8.156	+544
4:10	"	0.6023	8.297	+563
4:19	"	*	8.555	
4:26	"	*	8.761	
4:40	"	*	8.879	
5:00	"	0.6326	8.951	+579
6:50	"	0.6473	9.135	+579
7:40	"	*	9.141	
8:40	"	*	8.944	
9:50	"	*	8.963	
10:35	"	*	8.908	
11:20	"	*	9.287	
12:20	"	*	9.290	
Run No. 147, Catalyst- $Co_{1.09}Fe_{1.91}O_4$, Temperature 250°C				
10:20	Helium	0.5370	5.8662	+445
10:27	"	0.5220	5.774	+452
10:41	"	0.5404	5.913	+450
10:55	"	0.5497	5.946	+445
11:07	"	0.5514	5.955	+444
11:11	He+6cm H_2	0.5482	5.652	+422
11:14	"	0.5465	5.534	+415
11:26	"	0.5463	5.328	+399
11:38	"	0.5471	5.057	+379
11:50	"	0.5439	4.965	+375
12:10	"	0.5469	4.879	+367
1:10	"	0.5528	4.870	+362
2:49	Helium	0.5727	4.559	+336
3:06	"	0.5377	4.579	+349
3:40	"	0.5457	4.625	+347
4:47	"	0.5578	4.656	+347
8:20	"	0.5873	4.970	+346
8:29	He+2cmO_2	0.5776	7.491	+533
8:31	"	0.5730	7.540	+538
8:46	"	0.5764	7.618	+542
8:56	"	0.5776	7.590	+543
9:00	"	0.5724	7.593	+543
9:15	"	0.5710	7.836	+546

*ΔT assumed unchanged from previous reading

B. Raw Data and Calculated Thermoelectric Power for Adsorption Runs

TABLE XII (continued) Adsorption Runs

Time	Atmosphere	ΔT (millivolts Cr-Al couple)	EMF (millivolts)	Thermoelectric Power μV/°C
Run No. 158, Catalyst- $Co_{0.96}Fe_{2.04}O_4$, Temperature 88°C				
11:20	Helium	0.1130	-0.8968	-300
11:50	"	0.1061	-0.7739	-299
12:05	"	0.1055	-0.7689	-300
12:15	He+6cm H_2	0.1051	-0.7689	-300
12:25	"	0.1041	-0.7630	-301
12:40	"	0.1036	-0.7605	-301
1:12	"	0.1042	-0.7636	-300
1:55	"	0.1050	-0.7650	-299
5:25	"	0.1093	-0.7940	-298
Run No. 158a, Catalyst- $Co_{0.96}Fe_{2.04}O_4$, Temperature 120°C				
5:40	He+6cm H_2	0.2045	-1.5015	-303
5:45	"	0.2840	-2.0390	-294
5:47	"	0.3184	-2.3477	-303
5:55	"	0.3721	-2.6989	-297
6:05	"	0.4056	-2.9261	-296
6:30	"	0.4276	-3.0847	-296
8:00	"	0.4349	-3.1286	-296
Run No. 159, Catalyst- $Co_{0.96}Fe_{2.04}O_4$, Temperature 180°C				
8:30	Helium	0.5795	-4.3194	-306
8:45	"	0.5776	-4.3094	-306
9:00	He+10cm H_2	0.5668	-4.2454	-206
9:10	"	0.5664	-4.2436	-306
10:00	"	0.5719	-4.2201	-301
11:45	"	0.5738	-4.1733	-298
2:45	"	0.5699	-4.0800	-293
6:25	"	0.5706	-4.0277	-289
9:30	"	0.5762	-4.0454	-287
8:00a.m.	"	0.5653	-3.9265	-285

APPENDIX II

SAMPLE CALCULATION

Sample calculations of activation energy and pre-exponential factor for a typical hydrogen-deuterium exchange run are given below. Run No. 111, using $Co_{1.03}Fe_{1.97}O_4$ catalyst, is selected for this example solution. The data plot for Run No. 111 is given in Figure 21. The calculation techniques for determining the activation energy and pre-exponential factor are outlined in Chapter II, section D.

A. Activation Energy Calculation

As indicated by Equation (41), the activation energy may be determined from the slope of the $\ln[v_a T_i]$ vs. $1/T_i$ plot, where T_i is the temperature required at each flow rate v_i to reach the constant per cent conversion, p. The procedure was repeated for three values of per cent conversion, (i.e., i = 1, 2, 3).

Per Cent Conversion p	v_a cc./min.	Temperature °K	v_aT	$\ln\left(\frac{v_aT}{10}\right)$	$\frac{1}{T}$
.275	9.95	333.5	3318	5.804	.0029985
	15.00	338.2	5073	6.229	.0029568
	20.00	341.9	6838	6.527	.0029248
.350	9.95	337.1	3354	5.815	.0029664
	15.00	341.9	5129	6.240	.0029248
.425	20.00	345.7	6914	6.538	.0028927
	9.95	340.1	3384	5.284	.0029403
	15.00	345.1	5176	6.249	.0028977
	20.00	348.8	6977	6.548	.0028666

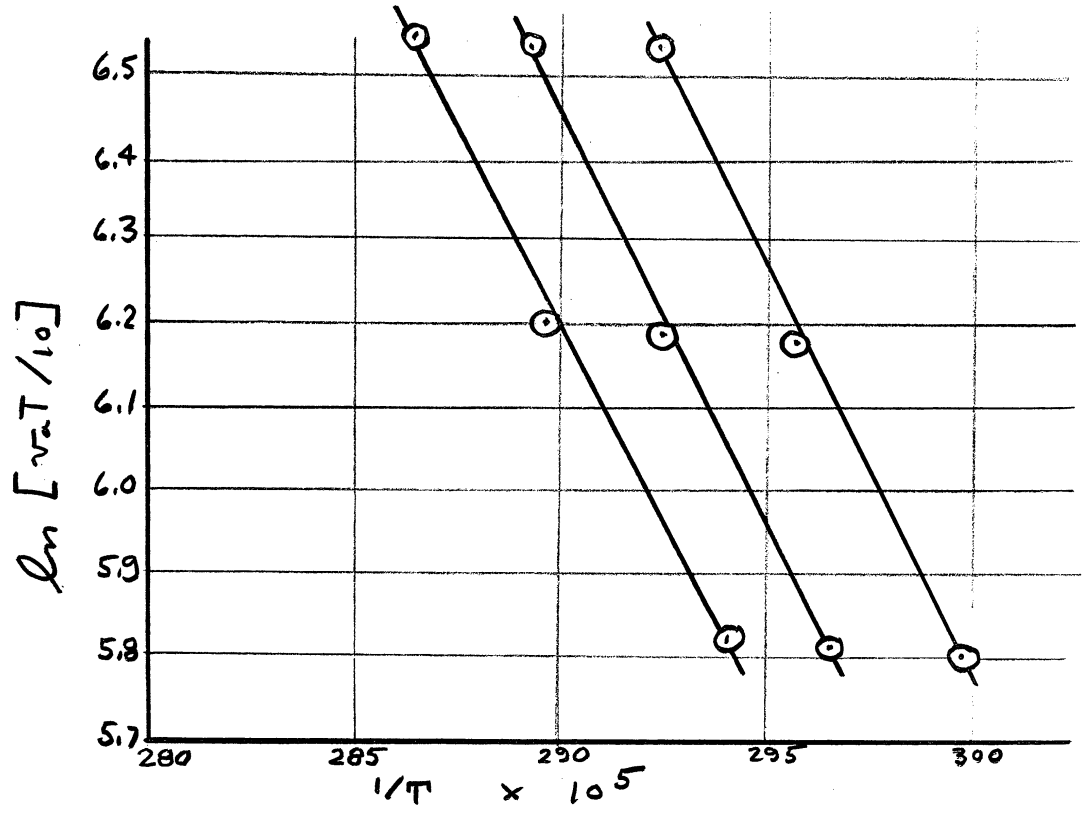

Per Cent Conversion	Activation Energy Calculation $E = (1.987)(\text{slope})$

.275 $\quad E = (1.987)\left[\dfrac{6.5 - 5.8}{299.8 - 292.6}\right]\dfrac{(10^{-3})}{(10^{-5})} = 19.0$ Kcal/mole

.350 $\quad E = (1.987)\left[\dfrac{6.5 - 5.8}{296.8 - 289.6}\right]\dfrac{(10^{-3})}{(10^{-5})} = 19.2$ Kcal/mole

.425 $\quad E = (1.987\left[\dfrac{6.5 - 5.8}{294.3 - 286.8}\right]\dfrac{(10^{-3})}{(10^{-5})} = 18.6$ Kcal/mole

B. Pre-exponential Factor Calculation

As indicated by Equation (54),

$$\ln k_o = E/kT + \ln\left[\frac{m T P_a}{V T_a P}\right] \qquad (54)$$

where m is the slope of a plot of $\ln\left[\frac{1}{1-p}\right]$ vs. $\frac{1}{v_a}$. The values of p and v_a for this plot are determined from Figure 21, at constant temperature. This procedure is repeated for three values of temperature. The smaple calculation below is made at a temperature of 67.5°C.

v_a	p	$\frac{1}{1-p}$	$\ln\left[\frac{1}{1-p}\right]$	$\frac{1}{v_a}$
20.0	.250	1.333	.288	.0500
15.0	.324	1.480	.392	.0667
9.9	.437	1.778	.576	.1005

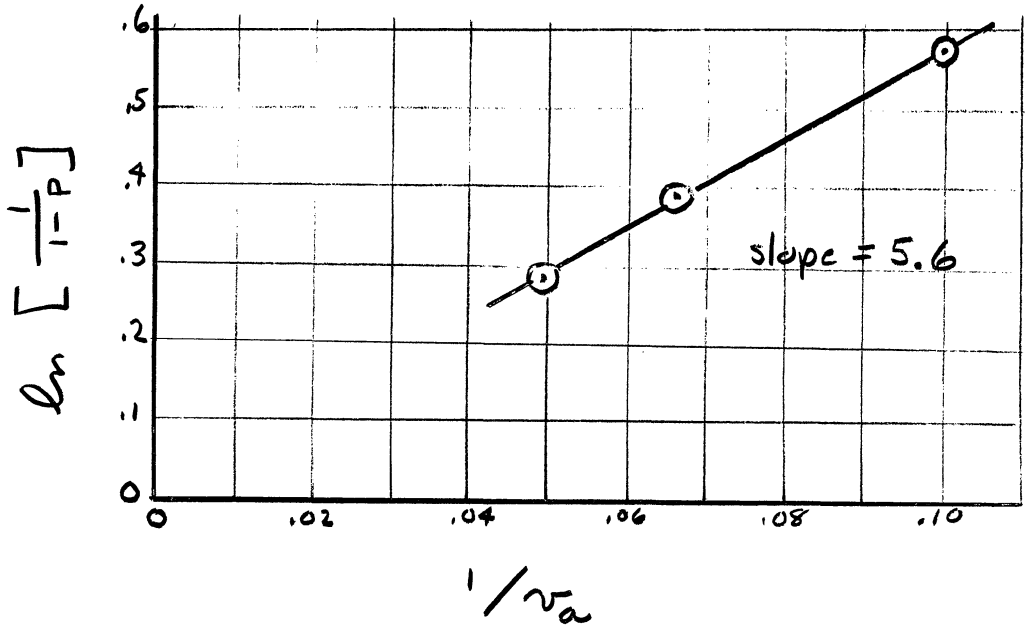

$$\ln k_o = \ln\left[\frac{mTP_a}{VT_aP}\right] + \frac{E}{kT}$$

$$\ln k_o = \ln\left[\frac{(5.6)(340.5)(14.6)}{(.43)(296.0)(14.6)}\right] + \frac{19.0}{(1.987)(340.5)}$$

$$\ln k_o = 2.7 + 28.1 = 30.8.$$

APPENDIX III

COMPARISON OF FERRITE MATERIALS USED IN EXCHANGE STUDIES AND THERMOELECTRIC POWER STUDIES

A. Hydrogen-Deuterium Exchange Studies

$Co_{0.98}Fe_{2.02}O_4$
Crushed Pellet

B. Thermoelectric Power Studies

$Co_{0.96}Fe_{2.04}O_4$
Powder

1. X-Ray Diffraction Pattern

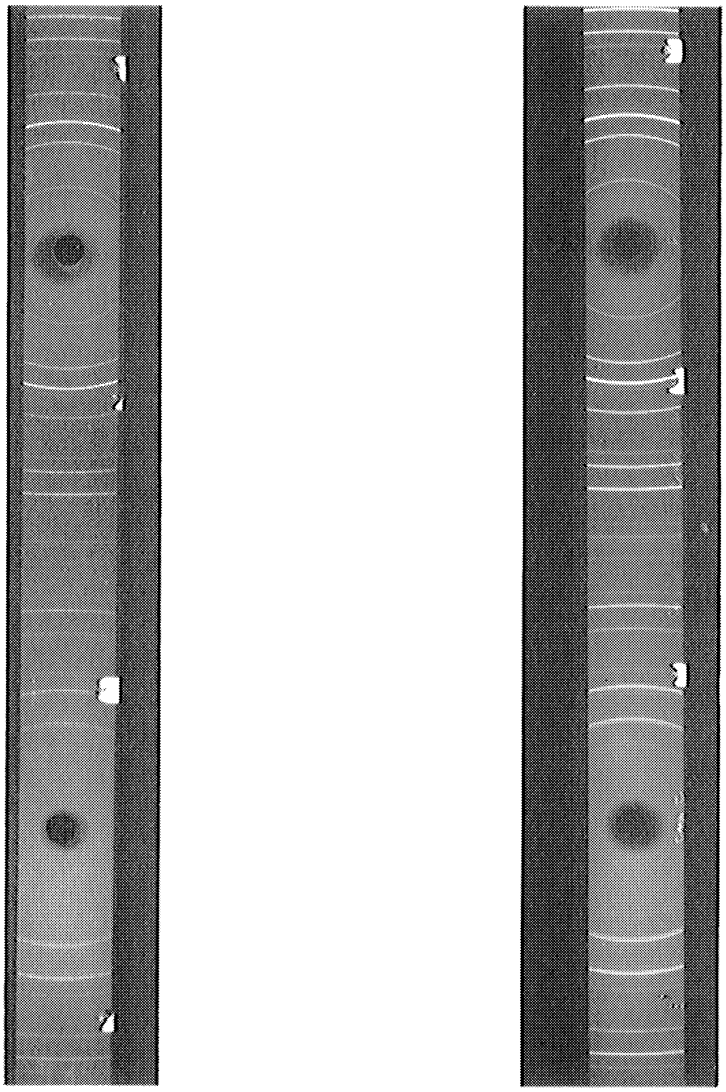

2. Bulk Density

5.2 gm./cc.

5.3 gm./cc.

Figure 35. Comparison of X-Ray Diffraction Patterns and True Bulk Densities of Ferrite Materials Used in Exchange Studies and Thermoelectric Power Studies.

TABLE XIII. $Co_{0.96}Fe_{2.04}O_4$ X-Ray Diffraction Pattern Calculation

Line Number	Intensity**	mm	2θ	d	$h^2+k^2+l^2$
1	30	29.880	21.32	4.84	3
2	50	28.495	35.17	2.91	8
3	100	27.865	41.47	2.256	12
4	4	27.665	43.47	2.415	12
5	2	27.490	45.22	2.326	*
6	50	26.950	50.62	2.092	16
7	2	26.475	55.37	1.925	19
8	30	25.700	63.12	1.718	24
9	70	25.265	67.47	1.610	27
10	80	24.575	74.37	1.480	32
11	3	24.175	78.37	1.415	35
12	2	23.850	81.62	1.368	*
13	5	23.515	84.92	1.374	40
14	20	23.120	88.92	1.277	43
15	5	22.990	90.22	1.263	44
16	5	22.465	95.47	1.209	48
17	2	22.070	99.42	1.172	51
18	10	21.415	105.97	1.120	56
19	50	21.010	110.02	1.091	59
20	20	20.290	117.22	1.098	64
21	10	19.035	129.77	.988	72
22	45	18.510	135.02	.968	75
23	16	18.315	136.97	.961	76
24	30	17.485	145.27	.937	80
25	5	16.720	150.92	.920	83

*These two lines are caused by iron contamination in the cobalt target used in the x-ray diffraction apparatus. These lines are apparent for the two strong intensities, 100 and 80. The ratio of the d values of the strong intensity lines to the d values of the extra lines should equal the ratio of the iron and cobalt wave lengths, 1.098. This calculation is given below:

$$45.22/41.97 = 1.098 \quad \text{and} \quad 81.62/74.37 = 1.098$$

**Center = 32.012

APPENDIX IV

X-RAY FLOURESCENT SPECTROMETER ANALYSES DATA

TABLE XIV. X-Ray Flourescent Data for Catalyst Samples

Sample	Side	Peak Height Fe	Peak Height Co	Fe/Co	Average	Std. Dev.
$Co_{1.07}Fe_{1.93}O_4$	1	75.2	76.2	.987		
		77.6	77.6	1.000		
		76.3	78.3	.974		
		78.0	76.8	1.016		
		76.8	77.8	.987		
		77.2	77.2	1.000		
		78.1	77.1	1.013		
		78.1	77.7	1.005		
		78.1	78.2	.999		
		78.3	78.4	.999		
		78.7	77.0	1.022		
		79.4	79.0	1.005		
					1.001	.0128
	2	82.9	84.8	.978		
		81.9	84.8	.966		
		82.4	84.2	.979		
		83.4	83.0	1.005		
		82.4	84.3	.977		
		84.0	83.6	1.005		
		81.8	83.8	.976		
		83.0	84.5	.982		
		82.5	83.9	.983		
		84.5	84.5	1.000		
		84.0	84.8	.991		
		83.3	84.2	.989		
					0.9859	.0118
$Co_{1.03}Fe_{1.07}O_4$	1	74.5	71.2	1.046		
		74.4	71.9	1.035		
		76.3	71.6	1.066		
		76.0	71.3	1.066		
		75.7	71.2	1.063		
		76.7	71.8	1.068		
		75.8	72.7	1.043		
		75.6	72.6	1.041		
		75.5	72.7	1.039		
		75.6	72.2	1.047		
		75.4	71.4	1.056		
		75.9	71.6	1.060		
					1.0525	.0114
	2	83.5	79.5	1.050		
		84.5	81.0	1.043		
		84.0	81.2	1.034		
		84.2	80.2	1.050		
		84.7	81.3	1.042		
		84.3	81.5	1.034		
		83.6	79.7	1.049		
		83.4	80.2	1.040		
		84.5	80.8	1.046		
		83.4	80.8	1.032		
		84.3	81.2	1.038		
		85.4	81.0	1.054		
					1.0427	.0022

Sample	Side	Peak Height Fe	Peak Height Co	Fe/Co	Average	Std. Dev.
$Co_{0.98}Fe_{2.02}O_4$*	1	83.2	74.8	1.112		
		85.2	74.1	1.150		
		84.7	74.2	1.142		
		85.3	74.0	1.153		
		85.5	75.6	1.131		
		84.8	74.6	1.137		
		84.9	95.0	1.132		
		85.3	74.5	1.145		
		85.7	74.3	1.153		
		84.9	75.3	1.127		
		83.9	75.1	1.117		
		85.6	75.0	1.141		
					1.1367	.0141
	2	76.1	66.2	1.150		
		76.0	66.8	1.138		
		75.6	66.0	1.145		
		75.5	65.6	1.151		
		73.9	65.0	1.137		
		74.8	66.5	1.125		
		74.8	66.4	1.127		
		76.8	65.4	1.174		
		75.1	67.0	1.121		
		74.4	66.1	1.126		
		75.5	66.2	1.140		
		74.7	64.9	1.151		
					1.140	.0141
*Sample reground between each analysis						
$Co_{0.93}Fe_{2.07}O_4$	1	78.6	64.3	1.222		
		77.6	63.9	1.214		
		78.9	63.4	1.244		
		78.4	64.2	1.221		
		78.9	64.5	1.223		
		77.9	63.1	1.235		
		79.3	64.2	1.235		
		78.2	64.4	1.214		
		78.3	63.2	1.239		
		78.8	64.0	1.231		
		79.0	62.4	1.266		
		78.7	63.7	1.235		
					1.2316	.0139
	2	86.1	71.7	1.201		
		86.4	70.7	1.222		
		85.4	70.4	1.213		
		86.7	70.1	1.237		
		86.5	70.0	1.236		
		86.5	71.5	1.210		
		85.7	70.1	1.222		
		86.5	71.4	1.211		
		87.5	70.7	1.238		
		87.9	70.9	1.240		
		86.6	71.4	1.213		
		86.4	70.5	1.226		
					1.222	.0125

TABLE XV. X-Ray Flourescent Data for Mixtures with Known Fe/Co Ratios

Sample	Side	Peak Height Fe	Peak Height Co	Fe/Co	Average	Std. Dev.
$Co_{0.90}/Fe_{2.10}$	1	83.4	64.3	1.297		
		83.8	64.5	1.299		
		83.2	64.2	1.296		
		83.5	64.7	1.291		
		83.5	64.6	1.293		
		83.2	64.4	1.292		
					1.295	.0091
	2	85.5	67.0	1.276		
		85.9	66.7	1.289		
		85.2	66.6	1.279		
		85.4	67.0	1.275		
		86.0	67.3	1.278		
		85.1	67.4	1.263		
					1.277	.0077
$Co_{1.0}/Fe_{2.0}$	1	80.8	72.9	1.108		
		81.4	73.3	1.111		
		81.1	72.9	1.112		
		81.2	72.7	1.117		
		80.9	72.7	1.113		
		81.3	73.4	1.108		
					1.112	.0098
	2	83.0	75.4	1.101		
		83.7	75.6	1.107		
		83.4	75.9	1.099		
		83.2	76.5	1.089		
		83.5	75.5	1.106		
		83.1	76.5	1.086		
					1.098	.0091

Sample	Side	Peak Height Fe	Peak Height Co	Fe/Co	Average	Std. Dev.
$Co_{1.10}/Fe_{1.90}$	1	75.2	79.6	0.945		
		75.9	79.2	0.958		
		75.6	79.7	0.949		
		76.0	80.0	0.950		
		75.3	79.3	0.950		
		75.5	81.2	0.930		
					.947	.0085
	2	76.8	80.3	0.956		
		76.7	80.8	0.040		
		76.3	80.2	0.951		
		76.0	80.0	0.950		
		75.9	80.0	0.949		
		76.4	80.7	0.947		
					.951	.0029

APPENDIX V

CHEMICAL ANALYSES OF RAW MATERIALS

TABLE XVI. Analyses of Fe_2O_3 and $CoCO_3$

Fe_2O_3 (Baker and Adamson Quality, Reagent grade, General Chemical Division, Allied Chemical and Dye Corp.)

Assay (Fe_2O_3)	min.	99.0 %
Maximum Limits of Impurities		
Insoluable in HCl		0.20
Sulfates (So_4)		0.20
Copper (Cu)		0.005
Zinc (Zn)		0.005
Substances not precipitated by NH_4OH (as sulfates)		0.10

$CoCO_3$ (Reagent grade cobalt carbonate, J. T. Baker Chemical Company)

Assay as Co	47.8 %
Insoluable in HCl	0.005
Chloride (Cl)	0.001
Nitrogen Compounds (as N)	0.005
Sulfates (So_4)	0.003
Lead (Pb)	0.003
Copper (Cu)	0.002
Iron (Fe)	0.001
Nickel (Ni)	0.05
Alkalides and Earths (SO_4)	0.24

APPENDIX VI

ENERGY OF FORMATION OF $CoFe_2O_4$

The standard free energy of formation of $CoFe_2O_4$ may be calculated from the following data:

Reaction*	Standard Free Energy of Reaction ΔG_T, cal.	Accuracy Kcal.	Temperature Range °K	Reference
$2\langle C_oO\rangle = 2\langle Co\rangle + (O_2)$	111,800 - 33.8T	2	298 - 1400	57
$\langle FeO\rangle = \langle Fe\rangle + \frac{1}{2}(O_2)$	55,620 - 10.83T	3	298 - 1642	57
$\langle Fe_3O_4\rangle = 3\langle FeO\rangle + \frac{1}{2}(O_2)$	74,620 - 29.9T	3	298 - 1642	57
$3\langle Fe_2O_3\rangle = 2\langle Fe_3O_4\rangle + \frac{1}{2}(O_2)$	59,620 - 33.62T	8	298 - 1460	57
$\langle Co\rangle + \langle Fe_2O_3\rangle = \langle CoFe_2O_4\rangle$	-5,000**		1275	**
$(H_2) + \frac{1}{2}(O_2) = (H_2O)$	-58,900 + 13.1T	1	298 - 2500	57

Calculated Standard Free Energy of $CoFe_2O_4$

$$\langle Co\rangle + 2\langle Fe\rangle + 2(O_2) \longrightarrow \langle CoFe_2O_4\rangle \qquad \Delta G_T = -241{,}490 + 69.67T$$

Equilibrium Oxygen Pressure

$$\log_{10} P_{O_2} = \frac{-241{,}490 + 69.67T}{9.14T} = 7.64 - \frac{26{,}420}{T}$$

If $P(O_2)$ is replaced by the equivalent $\frac{P_{H_2O}}{P_{H_2}}$, the following equations apply:

$$\langle Co\rangle + 2\langle Fe\rangle + 4\langle H_2O\rangle \longrightarrow \langle CoFe_2O_4\rangle + 4\langle H_2\rangle \qquad \Delta GT = -5{,}890 + 17.27T$$

$$\log_{10} \frac{P_{H_2O}}{P_{H_2}} \quad \frac{-5{,}890 + 17.27T}{18.28T} = 7.64 - \frac{322}{T}$$

* ⟨ ⟩ indicates solid, ( ) indicates gas

**Estimate from data by Schmalzried[82] for similar spinel reactions.

BIBLIOGRAPHY

1. Aigrain, P. and Dugas, C. Z., Z. Elektrochem., 56, 363, (1952).

2. Alkhazov, T. G., Belenskii, M. S., Izvestia Vysshikh Ucheb. Zavendenii, Neft i Gas, 3, 73, (1960).

3. A. P. I. Project 44, "Mass Spectral Data", Serial No. 452,453, (1950).

4. Becker, J. A., Green, C. B., Pearson, G. L., Trans. Am. Inst. Elect. Engrs. 65, 711, (1946).

5. Bevan, D. J. M. and Anderson, J. S., Disc. Faraday Society, 8, 235, (1950).

6. Bielanski, A., Deren J., and Haber, J., Nature, 179, 668, (1957).

7. Bielanski, A., Deren J., Haber, J., and Sloczynski, J., Proc. International Congress on Catalysis, 2nd, Paris, 1960, 2, 1653, (1961).

8. Bielanski, A., Deren J., Haber J., Sloczynski, J., and Wilkowa, J., Bull. acad. polon. sci., Ser. Sci., Chim geol. et geograph, 1, 333, (1959).

9. Bleakney, W., Phys. Rev. 40, 496, (1932); 41, 32, (1932).

10. Block, J. and Chon, H. Z., Elektrochem., 60, 912, (1956).

11. Bloem, J., Philips Research Repts., 13, 167, (1958).

12. Boreskov, G. K., Doklady Akad. Nauk SSSR, 127, 591, (1959).

13. Brewer, A. K., J. Phys. Chem. 32, 1006, (1928).

14. Cimino, A., Molinari, E., Cipollini, E., Gass. Chim. ital., 90, 79, 91, 120, (1960).

15. Culver, R. V. and Tompkins, F. C., Advances in Catalysis, 11, 68, (1959).

16. de Boer, J. H., "Electron Emission and Adsorption Processes", Cambridge University Press, London, 1935.

17. de Nobel, D., Philips Research Repts., 14, 361, (1959).

18. Dogramadzi, N. N., Matic, Z. B., Bull. Inst. Nuclear Sci., "Boris Kidrich", 11, 155, (1961).

19. Dowden, D. A., Mackenzie, N., and Trapnell, B. M. W., Proc. Roy. Soc. A237, 245, (1956).

20. Economos, G., J. Am. Ceram. Soc., 38, 241, (1955).

21. Economos, G., J. Am. Ceram. Soc., 38, 628, (1959).

22. Economos, G. and Clevenger, T. R., Jr., J. Am. Ceram. Soc., 43, 48, (1960).

23. Emmett, P. H., "Catalysts", Volz, Reinhold Publishing Corp., New York, 1955.

24. Enikeyev, E. H., Margolis, L. I., and Roginskii, S. Z., Doklady Akad. Nauk SSSR, 124, 606, (1959).

25. Evans, U. R., "Metallic Corrosion, Passivity, and Protection", Edward Arnold and Co., London, 1937.

26. Farrar, R. L., and Smith, H. A., J. Phys. Chem. 59, 763, (1955).

27. Finkelnburg, W. and Humbach, W., Naturwiss, 42, 35, (1955).

28. Frilzche, H., Z. Physik, 133, 422, (1952).

29. Fukutome, M. and Kusano, K., Kogyo Kagaku Zasshi, 63, 1186, (1960).

30. Garner, W. E., Advances in Catalysis, 9, 169, (1957).

31. Garner, W. E., Gray, T. J., and Stone, F. S., Proc. Roy. Soc., A197, 296, (1949).

32. Garrett, C. G. B., J. Chem. Phys., 33, 966, (1960).

33. Gorter, E. W., Proc. I. R. E., 43, 1945 (1955).

34. Gray, T. J., Disc. Faraday Society, 8, 331, (1950).

35. Halpern, J., Advances in Catalysis, 11, 301, (1959).

36. Harrison, L. G. and McDowell, C. A., Proc. Roy. Soc., A228, 66, (1955).

37. Hauffe, K., Advances in Catalysis, 7, 213, (1955).

38. Hauffe, K. and Engell, H. J., Z. Elektrochem., 56, 366, (1952).

39. Hauffe, K., Glang, R., and Engell, H. J., Z. physik Chem., 201, 223, (1952).

40. Hauffe, K. and Vierk, A. L., Z. physik Chem., 196, 160, (1950).

41. Heckelsberg, L. F., Clark, A., and Bailey, G. C., J. Phys. Chem., 60, 559, (1956).

42. Holm, V. C. F. and Blue, R. W., Ind. Eng. Chem., 44, 107, (1952).

43. Huston, A. R., in "Semiconductors", (Hannay, N. B., editor), p. 541, Reinhold Publishing Corporation, New York, 1959.

44. Jonker, G. H., unpublished measurements, (mentioned in Ref. 46).

45. Jonker, G. H., J. Phys. Chem. Solids, 9, 165, (1959).

46. Jonker, G. H. and van Houten, S., in "Halbleiterprobleme Band VI", p. 118, Verlag Friedr. Vieweg and Sohn, Braunschweig, 1961.

47. Keier, N. P. and Chizhikova, G. I., Doklady Akad. Nauk SSSR, 120, 830, (1955).

48. Keier, N. P. and Kutseva, L. N., Doklady Akad. Nauk SSSR, 117, 259, (1957).

49. Keier, N. P., Roginskii, S. Z., and Sazonovo, I. S., Izvest. Akad. Nauk SSSR, Ser Fiz, 21, 183, (1957).

50. Kirshenbaum, I., "Physical Properties and Analysis of Heavy Water", (Urey, H. C. and Murphy, G. M., editors), McGraw-Hill Book Company, Inc., New York, 1951.

51. Kittel, C., "Introduction to Solid State Physics", John Wiley and Sons, New York, 1956.

52. Kmetko, E. A., Phys. Rev. 99, 1642A, (1955).

53. Korsunovskii, G. A., Doklady Akad. Nauk SSSR, 134, 1394, (1960).

54. Krawczynski, Dissertation, Munich, (1956).

55. Kroger, F. A., Vink, H. J., and Volger, J., Physica, 20, 1095, (1954); Philips Research Repts. 10, 39, (1955).

56. Krusemeyer, H. J. and Thomas, D. G., J. Phys. Chem. Solids, 1, 78, (1958).

57. Kubaschewski, O., and Evans, E. L., "Metallurgical Thermodynamics", Pergamon Press, New York, 1958.

58. Kubokawa, Y. and Toyama, O., J. Phys. Chem. 60, 833, (1956).

59. Kuchaev, J. L. and Boreskov, G. K., Problemy Kinetiki i Kataliza, 10, 108, (1960).

60. Langmiur, I., J. Am. Chem. Soc. 38, 2221, (1916); 40, 1361, (1918); Trans. Faraday Society, 17, 607, (1922).

61. Law, J. T. in "Semiconductors", (Hannay, N. B., editor), p. 676, Reinhold Publishing Corporation, New York, 1959.

62. Leonard-Jones, J. G., Trans. Faraday Society, 28, 333, (1932).

63. Linde, V. R., Margolis L. Y. and Roginskii, S. Z., Doklady Akad. Nauk SSSR, 136, 860, (1961).

64. Mason, D. R., "Semiconductor Theory and Technology", Engineering Summer Conference, The University of Michigan, (1962). (To be published by McGraw-Hill Book Company, Inc., New York).

65. Matveev, K. and Boreskov, G. K., Problemy Kinetiki i Kataliza, 8, 165, (1955).

66. Molinari, E. and Parravano, G., J. Am. Chem. Soc., 75, 5233, (1953).

67. Morin, F. J. in "Semiconductors", (Hannay, N. B., editor), p. 600, Reinhold Publishing Corporation, New York, (1959).

68. Morrison, S. R., Advances in Catalysis, 7, 259, (1955).

69. Myosnikov, I. A. and Pshezhetsky, S. Y., Problemy Kinetiki i Kataliza, 8, 175, (1955).

70. Nier, A. O. C., Stevens, C. M., and Rustad, B., S. A. M. Report A-573, March 17, 1943.

71. Nyrop, J. E., "The Catalytic Action of Surfaces", Williams and Norgate, London, 1937.

72. Otwinowska, H., Treszczanowixz, E., and Ciboroski, S., Actes intern. Congr. Catalyse, 2nd, Paris 1960, 2, 1733, (1960).

73. Parravano, G. and Boudart, M., Advances in Catalysis, 7, 47, (1953).

74. Parravano, G. and Domenicali, C. A., J. Chem. Phys., 26, 359, (1957).

75. Penzkofer, Dissertation, Munich, (1956).

76. Rideal, E. K. and Wansbrough-Jones, O. H., Proc. Roy. Soc., A123, 202, (1929).

77. Rittenberg, D., Bleakney, W., and Urey, H. C., J. Chem. Phys., 2, 48, (1934).

78. Robin, J. andBenard, J., Compt. rend. 232, 1830, (1951); Compt. rend. 23, 734, (1952).

79. Roginskii, S. Z., Problemy Kinetiki i Kataliza, Akad. Nauk SSSR, Trudy Konf., 1958, 10, 5, (1960).

80. Roginskii, S. Z. and Schultz, E., Z. physik. Chem. A138, 21, (1928).

81. Roiter, B. D. and Paladino, A. E., J. Am. Ceram. Soc. 45, 128, (1962).

82. Schmalzried, H., Z. physik Chem. Neue Folge, 25, 178, (1960).

83. Schmidt, O., Chem. Revs., 12, 363, (1933).

84. Schuster, M. C. and Fullam, E. F., Ind. Eng. Chem., 18, 653, (1946).

85. Schwab, G. -M., Angew, Chem., 73, 399, (1961).

86. Schwab, G. -M., and Block, J., Z. Elektrochem. 58, 756, (1954); Z. physik Chem. N. F., 1. 42, (1954).

87. Schwab, G. -M., Roth, E., Grintzos, C., and Mavrakis, N., in "Structure and Properties of Solid Surfaces", p. 464, University of Chicago Press, Chicago, 1953.

88. Slater, J. C., "Handbuch der Physik", Vol. 19, J. Springer, Berlin, 1956.

89. Smiltens, R., J. Am. Chem. Soc., 79, 4881, (1957).

90. Solymosi, F., Magyar Tudomanyos Akad. Kens. Tudomanyak Ostalyonak Kozlemenyei, 13, 97, (1960).

91. Stockmann, F., Z. Physik, 127, 563, (1950).

92. Svadlenak, R. E. and Scott, A. B., J. Am. Chem. Soc., 79, 5385, (1957).

93. Taylor, H. S. and Liang, S. C., J. Am. Chem. Soc., 69, 1306, (1947).

94. Taylor, H. S. and Strother, C. O., J. Am. Chem. Soc., 56, 586, (1934).

95. Temkin, M. I., J. Phys. Chem. (U.S.S.R.) 15, 296, (1941).

96. Urey, H. C. and Teal, G. K., Revs. Modern Phys. 7, 34, (1935).

97. van Houten, S., J. Phys. Chem. Solids, 17, 7, (1960).

98. van Uitert, L. G., J. Chem. Phys., 23, 1883, (1955); 24, 306, (1956).

99. Verwey, E. J. W., in "Semiconducting Materials", p. 151, Butterworth Scientific Publications, London, 1951.

100. Verwey, E. J. W., Haaijman, P. W., Romeijn, F. C., and van Oosterhout, G. W., Philips Research Repts., 5, 173, (1950).

101. Wagner, C., Z. physik. Chem. B22, 181, (1933).

102. Wagner, C., J. Chem. Phys., 18, 69, (1950).

103. Wagner, C. and Hauffe, K., Z. Elektrochem., 44, 172, (1938).

104. Watson, H., Jr., J. Appl. Phys., 32, 120, (1961).

105. Weisz, P. B., J. Chem. Phys. 20, 1483, (1952); ibid 21, 1531, (1953).

106. Weller, S. W. and Voltz, S. E., J. Am. Chem. Soc. 75, 5227, (1953); Z. physik. Chem. Frankfort, N. S., 5, 100, (1955).

107. Wicke, E., Z. Elektrochem., 53, 279, (1949).

108. Winter, E. R. S., Advances in Catalysis, 10, 196, (1958).

109. Wolkenstein, Th., Uspekhi Fiz. Nauk, 60, 249, (1956).

110. Wolkenstein, Th., J. chim. phys., 54, 175, (1957).

111. Wolkenstein, Th., Advances in Catalysis, 9, 807, 818, (1957).

112. Wolkenstein, Th., Advances in Catalysis, 12, 189, (1960).

113. Wolkenstein, Th., "Theorie Electronique de la Catalyse sur les Semi-conducteurs", Mason and Cie, Paris, 1961.

NOMENCLATURE

A	Surface area, $m^2/gm.$
$a_1 \ldots a_6$	Proportionality constant between pressure runs and mass spectrometer peak height (see Table II)
$b_1 \ldots b_7$	Proportionality constant between $(\text{pressure})^2$ and mass spectrometer peak height (see Table II)
b	Adsorption coefficient
b_o	Defined by Equation (24)
d	Electron jump length, cm, see Equation (1)
d	Average particle diameter, microns
d	Average interplanar spacing (see Table XIII)
E	Activation energy in Arrheius equation, Kcal/gm. mole
E_1	Energy of adsorption
E_2	Energy of desorption
E_{01}	Defined by Equation (25)
E_{02}	Defined by Equation (26)
E_a	Energy of acceptor level
E_b	Energy of surface acceptor level
E_d	Energy of donor level
E_f	Fermi level
E_g	Energy of conduction level
e	Charge on electron
e	Base of natural logarithms
h	Planck's constant
h,k,l	Miller indices
I	Ionization potential

I_i	Mass spectrometer peak height (i=2,3,4--refers to mass of molecule)
k	Boltzmann's constant
k	Rate Constant
k_o	Pre-exponential factor in Arrhenius equation
k_1	Rate constant for adsorption
k_2	Rate constant for desorption
k_{01}	Defined by Equation (27)
k_{02}	Defined by Equation (28)
ln	Natural logarithm (to the base e)
m*	Effective mass
m	Defined by Equation (53)
N	Concentration of sites available for electrons and holes, cm^{-3}
N_A	Total concentration of acceptors (ionized and unionized)
N_B	Total concentration of surface sites
N_C	Concentration of states in conduction level
N_D	Total concentration of donors (ionized and unionized)
N_V	Concentration of states in valence level
n_1	Concentration of electrons in conduction level
n_2	Concentration of holes in valence levels
P	Pressure
p	Per cent conversion of deuterium to hydrogen-deuteride
Q	Heat of adsorption
q	Activation energy for lattice deformation

r	Rate of reaction
S	Surface site for adsorption
T	Temperature, °K
t	Time
V	Void volume of reaction, cc.
v	Flow rate through reactor at S.T.P. cc./min.
v_a	Flow rate through reactor at actual temperatures and pressure, cc./min.
w	Energy of interaction between adsorbed atom and surface
w_1	Rate of adsorption
w_2	Rate of desorption
α	Extra contribution to transport energy levels of electrons
α'	α (kT)
β	Extra contribution to transport energy levels of holes
β'	β (kT)
γ	Defined by Figure 6 and Equations (25) and (26)
Δ	Indicates a difference (i.e., $\Delta T = T_2 - T_1$)
Θ	Thermoelectric power, μv/°C
θ	Per cent surface coverage
μ	Mobility, cm^2/v.sec.
μ	Abbreviation for micron
ν	Frequency of lattice vibrations, sec^{-1}
Π	Peltier coefficient
ρ	Catalyst density
Σ	Summation
σ	Electrical conductivity

ϕ	Work function

Subscripts

1	Electrons, or adsorption
2	Holes, or desorption
A	Acceptor level, or molecule A
a	Actual conditions
B	Surface acceptor level
C	Conductor level
0	Initial state
t	Time
V	Valence level